

AFIT/GE/ENG/97D-11

ATMOSPHERIC TURBULENCE SCINTILLATION EFFECTS ON WAVEFRONT
TILT ESTIMATION

THESIS
James Allan Louthain
Captain, USAF

AFIT/GE/ENG/97D-11

Approved for public release; distribution unlimited

19980128 113

The views expressed in this thesis are those of the author and do not reflect the official policy or position of the Department of Defense or the United States Government.

AFIT/GE/ENG/97D-11

ATMOSPHERIC TURBULENCE SCINTILLATION EFFECTS ON
WAVEFRONT TILT ESTIMATION

THESIS

Presented to the Faculty of the School of Engineering
of the Air Force Institute of Technology

Air University

In Partial Fulfillment of the
Requirements for the Degree of
Master of Science in Electrical Engineering

James Allan Louthain, B.S.E.E.

Captain, USAF

December, 1997

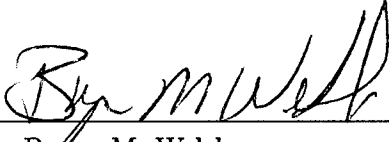
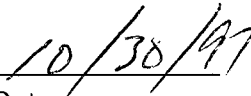

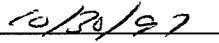
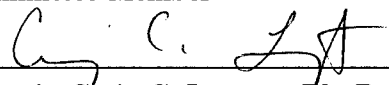
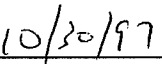
Approved for public release; distribution unlimited

ATMOSPHERIC TURBULENCE SCINTILLATION EFFECTS ON
WAVEFRONT TILT ESTIMATION

James Allan Louthain, B.S.E.E.

Captain, USAF

Approved:

 _____ Dr. Byron M. Welsh Thesis Advisor	 _____ Date
 _____ Dr. Michael C. Roggemann Committee Member	 _____ Date
 _____ Captain Craig C. Largent, Ph. D. Committee Member	 _____ Date

Acknowledgements

First of all, I thank my committee members Dr. Byron Welsh, Dr. Michael Roggemann, and Capt Craig Largent for their invaluable guidance during this thesis effort. A special thanks is due to Dr. Welsh for his uncanny ability to analyze complicated equations and his rapid but ruthless editing which proved to be invaluable to producing this final document. I thank Dan Zambon and Dave Doak for keeping the SUN workstations and the Hawkeye Lab running smoothly. I would also like to thank Troy VanCaster for leading me through the ways of L^AT_EX, since he always seemed to have solved the problems just before I needed them. Most importantly, I give a heartfelt thanks to my wife, Julie, for her understanding, support, and help during these past eighteen months.

James Allan Louthain

Table of Contents

	Page
Acknowledgements	iii
List of Figures	vii
List of Tables	xv
Abstract	xvi
 I. Introduction	 1-1
1.1 Atmospheric Turbulence Modeling	1-2
1.2 Adaptive Optic Systems	1-4
1.3 Summary of key results	1-6
1.4 Overview	1-6
 II. Correlation Functions of Weak Turbulence	 2-1
2.1 Derivation of Correlation Functions	2-1
2.2 Correlations for a constant strength of turbulence	2-6
2.3 Structure Functions	2-12
2.4 Mean Square Value Functions	2-13
 III. Phase, Amplitude, and Cross Power Spectral Densities of Weak Turbulence	 3-1
 IV. Fourier Series Based Atmospheric Phase and Amplitude Field Screen Generator	 4-1
4.1 The Development of the Random Screen	4-2
4.2 Method for Screen Generation	4-5
4.3 Field Screen Generation Procedure	4-6
4.3.1 Set-up:	4-6

	Page
4.3.2 Screen Generation:	4-7
4.4 Numerical Results	4-9
4.4.1 Weak Turbulence Atmospheric Statistics	4-9
4.4.2 Setup for independent uncorrelated phase and amplitude screen generation: Steps 1 and 2	4-10
4.4.3 Simulation results for independent uncorrelated amplitude and phase screen generation	4-10
4.4.4 Setup for independent correlated phase and amplitude screen generation: Steps 1, 2, and 3.	4-15
4.4.5 Simulation results for independent correlated amplitude and phase screen generation	4-15
V. Amplitude Effects on Full Aperture Tilt Sensing	5-1
5.1 Full aperture tilt estimation using image centroid	5-1
5.1.1 Tilt estimation calculation using random screens	5-4
5.2 Simulations using the random screen generator with uncorrelated amplitude and phase screens	5-4
5.2.1 Mean square error in the tilt estimation	5-5
5.2.2 Strehl ratio calculation	5-11
5.3 Comparisons of simulations using correlated versus uncorrelated phase and amplitude screens	5-22
5.3.1 Mean Square Error in the Tilt Estimation with correlated versus uncorrelated screens	5-22
5.3.2 Strehl Ratio Calculation with correlated versus uncorrelated screens	5-22
5.3.3 Conclusions about using correlated versus uncorrelated screens	5-27
VI. Conclusions and Recommendations	6-1
6.1 Conclusions	6-1

	Page
6.2 Recommendations for Further Study	6-2
6.2.1 Screen Generation	6-2
6.2.2 Simulations	6-2
Bibliography	BIB-1
Vita	VITA-1

List of Figures

Figure		Page
1.1.	Simplified optical configuration of an adaptive optics imaging system	1-5
2.1.	A cross section of the Fourier representation of the random refractivity slab, where $A(n, \vec{\kappa})$ is the amplitude, $\phi_o(\eta, \vec{\kappa})$ is the random phase and $\frac{\kappa_1}{2\pi}$ is the spatial frequency.	2-2
2.2.	The normalized amplitude correlation is plotted versus $\frac{d}{L_o}$ for a strength of turbulence, $L_o/r_o = 100$, and $\frac{L_o^2}{\lambda L} = 20000$	2-10
2.3.	The normalized phase correlation is plotted versus $\frac{d}{L_o}$ for a strength of turbulence, $L_o/r_o = 100$, and $\frac{L_o^2}{\lambda L} = 20000$	2-10
2.4.	The normalized cross correlation is plotted versus $\frac{d}{L_o}$ for a strength of turbulence, $L_o/r_o = 100$, and $\frac{L_o^2}{\lambda L} = 20000$	2-11
2.5.	The mean square value of the amplitude perturbations in the pupil are plotted for different strengths of turbulence, L_o/r_o	2-14
2.6.	The mean square value of the phase perturbations in the pupil are plotted for different strengths of turbulence, L_o/r_o	2-15
2.7.	The mean cross value of the phase and amplitude perturbations in the pupil are plotted for different strengths of turbulence, L_o/r_o	2-15
3.1.	The power spectral densities as a function of ρL_o for $\lambda/L_o = 5 \times 10^{-8}$, $L/L_o = 10000$, and $L_o/r_o = 100$	3-6
4.1.	Theoretical and simulated phase structure function, $D_{pp}(\vec{d})$ plotted versus $ \vec{d} /L_o$ for a von Karman turbulence power spectrum with $D_p^\phi/L_o = 4$, $D_p^\phi/r_o = 400$, $L/L_o = 1000$, and $\lambda/L_o = 5 \times 10^{-8}$. The screen dimension is $D = 10r_o$ and the number of FS coefficients is $N = 300$	4-12
4.2.	Theoretical and simulated amplitude structure function, $D_{aa}(\vec{d})$ plotted versus $ \vec{d} /L_o$ for a von Karman turbulence power spectrum with $D_p^A/L_o = 1/4$, $D_p^A/r_o = 25$, $L/L_o = 1000$, and $\lambda/L_o = 5 \times 10^{-8}$. The screen dimension is $D = 10r_o$ and the number of FS coefficients is $N = 300$	4-12

Figure		Page
4.3.	Theoretical and simulated phase structure function, $D_{pp}(\vec{d})$, plotted versus $ \vec{d} /L_o$ for a von Karman turbulence power spectrum with $D_p^\phi/L_o = 4$, $D_p^\phi/r_o = 400$, $L/L_o = 1000$, and $\lambda/L_o = 5 \times 10^{-8}$. The screen dimension is $D = 40r_o$ and the number of FS coefficients is $N = 300$	4-13
4.4.	Theoretical and simulated amplitude structure function, $D_{aa}(\vec{d})$, plotted versus $ \vec{d} /L_o$ for a von Karman turbulence power spectrum with $D_p^A/L_o = 1/4$, $D_p^A/r_o = 25$, $L/L_o = 1000$, and $\lambda/L_o = 5 \times 10^{-8}$. The screen dimension is $D = 40r_o$ and the number of FS coefficients is $N = 300$	4-13
4.5.	Theoretical and simulated phase structure function, $D_{pp}(\vec{d})$, plotted versus $ \vec{d} /L_o$ for a von Karman turbulence power spectrum with $D_p^\phi/L_o = 4$, $D_p^\phi/r_o = 400$, $L/L_o = 1000$, and $\lambda/L_o = 5 \times 10^{-8}$. The screen dimension is $D = 100r_o$ and the number of FS coefficients is $N = 300$	4-14
4.6.	Theoretical and simulated amplitude structure function, $D_{aa}(\vec{d})$, plotted versus $ \vec{d} /L_o$ for a von Karman turbulence power spectrum with $D_p^A/L_o = 5/8$, $D_p^A/r_o = 62.5$, $L/L_o = 1000$, and $\lambda/L_o = 5 \times 10^{-8}$. The screen dimension is $D = 100r_o$ and the number of FS coefficients is $N = 450$	4-14
4.7.	Theoretical and simulated phase structure function, $D_{pp}(\vec{d})$, plotted versus $ \vec{d} /L_o$ for a von Karman turbulence power spectrum with $D_p/L_o = 1.5$, $D_p/r_o = 150$, $L/L_o = 1000$, and $\lambda/L_o = 5 \times 10^{-8}$. The screen dimension is $D = 10r_o$ and the number of FS coefficients is $N = 400$. The phase screens used in this calculation were correlated with the amplitude screens by the cross correlation.	4-16
4.8.	Theoretical and simulated amplitude structure function, $D_{aa}(\vec{d})$, plotted versus $ \vec{d} /L_o$ for a von Karman turbulence power spectrum with $D_p/L_o = 1.5$, $D_p/r_o = 150$, $L/L_o = 1000$, and $\lambda/L_o = 5 \times 10^{-8}$. The screen dimension is $D = 10r_o$ and the number of FS coefficients is $N = 400$. The amplitude screens used in this calculation were correlated with the phase screens by the cross correlation.	4-17

Figure		Page
4.9.	Theoretical and simulated cross structure function, $D_{ap}(\vec{d})$, plotted versus $ \vec{d} /L_o$ for a von Karman turbulence power spectrum with $D_p/L_o = 1.5$, $D_p/r_o = 150$, $L/L_o = 1000$, and $\lambda/L_o = 5 \times 10^{-8}$. The screen dimension is $D = 10r_o$ and the number of FS coefficients is $N = 400$	4-17
4.10.	Theoretical and simulated phase structure function, $D_{pp}(\vec{d})$, plotted versus $ \vec{d} /L_o$ for a von Karman turbulence power spectrum with $D_p/L_o = 1.5$, $D_p/r_o = 150$, $L/L_o = 1000$, and $\lambda/L_o = 5 \times 10^{-8}$. The screen dimension is $D = 100r_o$ and the number of FS coefficients is $N = 400$. The phase screens used in this calculation were correlated with the amplitude screens by the cross correlation.	4-18
4.11.	Theoretical and simulated amplitude structure function, $D_{aa}(\vec{d})$, plotted versus $ \vec{d} /L_o$ for a von Karman turbulence power spectrum with $D_p/L_o = 1.5$, $D_p/r_o = 150$, $L/L_o = 1000$, and $\lambda/L_o = 5 \times 10^{-8}$. The screen dimension is $D = 100r_o$ and the number of FS coefficients is $N = 400$. The amplitude screens used in this calculation were correlated with the phase screens by the cross correlation.	4-18
4.12.	Theoretical and simulated cross structure function, $D_{ap}(\vec{d})$, plotted versus $ \vec{d} /L_o$ for a von Karman turbulence power spectrum with $D_p/L_o = 1.5$, $D_p/r_o = 150$, $L/L_o = 1000$, and $\lambda/L_o = 5 \times 10^{-8}$. The screen dimension is $D = 100r_o$ and the number of FS coefficients is $N = 400$	4-19
4.13.	Random phase screen, $\hat{\phi}(\vec{d})$, plotted versus $ \vec{d} /L_o$ for a von Karman turbulence power spectrum with $D_p/L_o = 4$, $D_p/r_o = 400$, $L/L_o = 1000$, and $\lambda/L_o = 5 \times 10^{-8}$. The screen dimension is $D = 10r_o$ and the number of FS coefficients is $N = 300$	4-20
4.14.	Random amplitude screen, $\hat{A}(\vec{d})$, plotted versus $ \vec{d} /L_o$ for a von Karman turbulence power spectrum with $D_p/L_o = 1/4$, $D_p/r_o = 25$, $L/L_o = 1000$, and $\lambda/L_o = 5 \times 10^{-8}$. The screen dimension is $D = 10r_o$ and the number of FS coefficients is $N = 300$	4-21
5.1.	Simplified configuration of a full aperture tilt centroid tracker. (C_x, C_y) is the location of the image centroid and f is the focal length of the lens.	5-2

Figure		Page
5.2.	The mean square error in the tilt estimation, T_{mse} , and the mean square tilt, T_{ms} , are plotted versus L/L_o for $D/r_o = 10$, $L_o/r_o = 200$, and $\lambda/L_o = 5.0 \times 10^{-8}$. The T_{mse} is calculated twice, once using the phase and amplitude screen case and once for the phase screen only case. The T_{ms} is calculated by computing the average slope of the phase over the screen.	5-7
5.3.	The mean square error in the tilt estimation, T_{mse} , and the mean square tilt, T_{ms} , are plotted versus L_o/r_o for $D/r_o = 10$, $L/L_o = 10000$, and $\lambda/L_o = 5.0 \times 10^{-8}$. The T_{mse} is calculated twice, once using the phase and amplitude screen case and once for the phase screen only case. The T_{ms} is calculated by computing the average slope of the phase over the screen.	5-8
5.4.	The mean square error in the tilt estimation, T_{mse} , and the mean square tilt, T_{ms} , are plotted versus λ/L_o for $D/r_o = 10$, $L/L_o = 10000$, and $L_o/r_o = 200$. The T_{mse} is calculated twice, once using the phase and amplitude screen case and once for the phase screen only case. The T_{ms} is calculated by computing the average slope of the phase over the screen.	5-9
5.5.	The mean square error in the tilt estimation, T_{mse} , and the mean square tilt, T_{ms} , are plotted versus D/r_o for $\lambda/L_o = 5.0 \times 10^{-8}$, $L/L_o = 10000$, and $L_o/r_o = 200$. The T_{mse} is calculated twice, once using the phase and amplitude screen case and once for the phase screen only case. The T_{ms} is calculated by computing the average slope of the phase over the screen.	5-10
5.6.	Block diagram of Strehl ratio calculation procedure. Random screens are generated by following the <i>Screen Generation</i> procedure in Sec. 4.3.2. Strehl ratios SR_{UT} , SR_{UTP} , and SR_{UTAP} are for screens compensated by the actual tilt, estimated tilt using phase screen image centroid, and estimated tilt using phase/amplitude screen image centroid, respectively. The fourth Strehl ratio, SR , is calculated for the random uncompensated phase/amplitude screen.	5-13
5.7.	Point spread function of the diffraction limited unaberrated screen. .	5-14

Figure		Page
5.8.	Point spread function (psf) of the uncorrected random screen for the short exposure image for the following parameters $L/L_o = 50,000$, $D/r_o = 10$, $L_o/r_o = 200$, and $\lambda/L_o = 5.0 \times 10^{-8}$	5-15
5.9.	Point spread function (psf) of the uncorrected random screen for the long exposure image for the following parameters $L/L_o = 50,000$, $D/r_o = 10$, $L_o/r_o = 200$, and $\lambda/L_o = 5.0 \times 10^{-8}$	5-15
5.10.	Point spread function (psf) of the corrected random screen using the image centroid of the phase screen only to determine the tilt for the long exposure image for the following parameters $L/L_o = 50,000$, $D/r_o = 10$, $L_o/r_o = 200$, and $\lambda/L_o = 5.0 \times 10^{-8}$	5-16
5.11.	Point spread function (psf) of the corrected random screen using the actual average tilt for the long exposure image for the following parameters $L/L_o = 50,000$, $D/r_o = 10$, $L_o/r_o = 200$, and $\lambda/L_o = 5.0 \times 10^{-8}$	5-16
5.12.	Point spread function (psf) of the corrected random screen using the image centroid of the phase/amplitude screen for the long exposure image for the following parameters $L/L_o = 50,000$, $D/r_o = 10$, $L_o/r_o = 200$, and $\lambda/L_o = 5.0 \times 10^{-8}$	5-17
5.13.	Strehl ratios of the simulated wavefront are plotted versus L/L_o for $D/r_o = 10$, $L_o/r_o = 200$, and $\lambda/L_o = 5.0 \times 10^{-8}$. Strehl ratios are plotted for the compensated screen with phase/amplitude centroid, SR_{UTAP} , compensated screen with actual phase tilt, SR_{UT} , compensated screen with phase centroid, SR_{UTP} , and uncompensated screen, SR	5-18
5.14.	Strehl ratios of the simulated wavefront are plotted versus L_o/r_o for $D/r_o = 10$, $L/L_o = 10000$, and $\lambda/L_o = 5.0 \times 10^{-8}$. Strehl ratios are plotted for the compensated screen with phase/amplitude centroid, SR_{UTAP} , compensated screen with actual phase tilt, SR_{UT} , compensated screen with phase centroid, SR_{UTP} , and uncompensated screen, SR	5-19

Figure		Page
5.15.	Strehl ratios of the simulated wavefront are plotted versus λ/L_o for $D/r_o = 10$, $L/L_o = 10000$, and $L_o/r_o = 200$. Strehl ratios are plotted for the compensated screen with phase/amplitude centroid, SR_{UTAP} , compensated screen with actual phase tilt, SR_{UT} , compensated screen with phase centroid, SR_{UTP} , and uncompensated screen, SR	5-20
5.16.	Strehl ratios of the simulated wavefront are plotted versus D/r_o for $\lambda/L_o = 5.0 \times 10^{-8}$, $L/L_o = 10000$, and $L_o/r_o = 200$. Strehl ratios are plotted for the compensated screen with phase/amplitude centroid, SR_{UTAP} , compensated screen with actual phase tilt, SR_{UT} , compensated screen with phase centroid, SR_{UTP} , and uncompensated screen, SR	5-21
5.17.	The amplitude and phase screen are correlated by the cross correlation. The mean square error in the tilt estimation, T_{mse} , and the mean square tilt, T_{ms} , are plotted versus L/L_o for $D/r_o = 10$, $L_o/r_o = 200$, and $\lambda/L_o = 5.0 \times 10^{-8}$. The T_{mse} is calculated twice, once using the phase and amplitude screen case and once for the phase screen only case. The T_{ms} is calculated by computing the average slope of the phase over the screen. $D_p/L_o = D_p^A/L_o = D_p^\phi/L_o = D_p^C/L_o = 1.5$. .	5-23
5.18.	The amplitude and phase screen are uncorrelated . The mean square error in the tilt estimation, T_{mse} , and the mean square tilt, T_{ms} , are plotted versus L/L_o for $D/r_o = 10$, $L_o/r_o = 200$, and $\lambda/L_o = 5.0 \times 10^{-8}$. The T_{mse} is calculated twice, once using the phase and amplitude screen case and once for the phase screen only case. The T_{ms} is calculated by computing the average slope of the phase over the screen. $D_p^A/L_o = 1.5$ and $D_p^\phi/L_o = 1.5$	5-23
5.19.	The amplitude and phase screen are correlated by the cross correlation. The mean square error in the tilt estimation, T_{mse} , and the mean square tilt, T_{ms} , are plotted versus L_o/r_o for $D/r_o = 10$, $L/L_o = 10000$, and $\lambda/L_o = 5.0 \times 10^{-8}$. The T_{mse} is calculated twice, once using the phase and amplitude screen case and once for the phase screen only case. The T_{ms} is calculated by computing the average slope of the phase over the screen. $D_p/L_o = D_p^A/L_o = D_p^\phi/L_o = D_p^C/L_o = 1.5$.	5-24

Figure		Page
5.20.	The amplitude and phase screen are uncorrelated . The mean square error in the tilt estimation, T_{mse} , and the mean square tilt, T_{ms} , are plotted versus L_o/r_o for $D/r_o = 10$, $L/L_o = 10000$, and $\lambda/L_o = 5.0 \times 10^{-8}$. The T_{mse} is calculated twice, once using the phase and amplitude screen case and once for the phase screen only case. The T_{ms} is calculated by computing the average slope of the phase over the screen. $D_p^A/L_o = 1.5$ and $D_p^\phi/L_o = 1.5$	5-24
5.21.	The amplitude and phase screen are correlated by the cross correlation. Strehl ratios of the simulated wavefront are plotted versus L/L_o for $D/r_o = 10$, $L_o/r_o = 200$, and $\lambda/L_o = 5.0 \times 10^{-8}$. Strehl ratios are plotted for the compensated screen with phase/amplitude centroid, SR_{UTAP} , compensated screen with actual phase tilt, SR_{UT} , compensated screen with phase centroid, SR_{UTP} , and uncompensated screen, SR . $D_p/L_o = D_p^A/L_o = D_p^\phi/L_o = D_p^C/L_o = 1.5$	5-25
5.22.	The amplitude and phase screen are uncorrelated . Strehl ratios of the simulated wavefront are plotted versus L/L_o for $D/r_o = 10$, $L_o/r_o = 200$, and $\lambda/L_o = 5.0 \times 10^{-8}$. Strehl ratios are plotted for the compensated screen with phase/amplitude centroid, SR_{UTAP} , compensated screen with actual phase tilt, SR_{UT} , compensated screen with phase centroid, SR_{UTP} , and uncompensated screen, SR . $D_p^A/L_o = 1.5$ and $D_p^\phi/L_o = 1.5$	5-25
5.23.	The amplitude and phase screen are correlated by the cross correlation. Strehl ratios of the simulated wavefront are plotted versus L_o/r_o for $D/r_o = 10$, $L/L_o = 10000$, and $\lambda/L_o = 5.0 \times 10^{-8}$. Strehl ratios are plotted for the compensated screen with phase/amplitude centroid, SR_{UTAP} , compensated screen with actual phase tilt, SR_{UT} , compensated screen with phase centroid, SR_{UTP} , and uncompensated screen, SR . $D_p/L_o = D_p^A/L_o = D_p^\phi/L_o = D_p^C/L_o = 1.5$	5-26

Figure		Page
5.24.	The amplitude and phase screen are uncorrelated . Strehl ratios of the simulated wavefront are plotted versus L_o/r_o for $D/r_o = 10$, $L/L_o = 10000$, and $\lambda/L_o = 5.0 \times 10^{-8}$. Strehl ratios are plotted for the compensated screen with phase/amplitude centroid, SR_{UTAP} , compensated screen with actual phase tilt, SR_{UT} , compensated screen with phase centroid, SR_{UTP} , and uncompensated screen, SR . $D_p^A/L_o = 1.5$ and $D_p^\phi/L_o = 1.5$	5-26

List of Tables

Table		Page
5.1.	Atmospheric turbulence and optical parameters used in simulations.	5-5

Abstract

A new atmospheric turbulence screen generator is developed for use in performance calculations of adaptive optics systems valid over a wide range of atmospheric turbulence parameters. The screen generator accounts for diffraction effects caused by weak turbulence and incorporates the phase, amplitude, and cross statistics of the perturbed optical field. The wavefront's phase and amplitude perturbations are taken from the correlation functions developed by Lee and Harp and the cross correlation of the phase and amplitude derived in this thesis. The screen generator uses a modal representation to perform a Fourier series expansion of the wavefront phase and amplitude over a square area. The phase, amplitude, and cross power spectral densities determined from the correlation functions are used in the Fourier series expansion. The mean square value and the structure functions of the phase, amplitude, and cross terms are calculated to within 1% of the theoretical values in a Monte Carlo experiment using the screen generator. Monte Carlo experiments performed using the screen generator showed the amplitude perturbations can significantly reduce the accuracy of full-aperture tilt estimation using image centroid motion. However, since the amplitude perturbations affect the image centroid, the tilt estimate using the combined amplitude and phase screen allows for a higher Strehl ratio than using only the phase to estimate the correction.

ATMOSPHERIC TURBULENCE SCINTILLATION EFFECTS ON WAVEFRONT TILT ESTIMATION

I. Introduction

When the aperture size of an optical system limits the resolution of the system it is referred to as diffraction limited. Atmospheric turbulence replaces the aperture size as the limiting factor in optical performance for large aperture systems, when imaging or propagating through the earth's atmosphere. The heating and cooling of the earth's surface along with a mixing effect of wind causes the atmosphere to be turbulent. As a wavefront from an object travels through this turbulent atmosphere, the turbulence will cause different sections of the wavefront to experience different optical path lengths. The optical path differences will bend the wavefront, resulting in optical field perturbations. These random fluctuations in the optical field can cause extensive blurring in imaging through the atmosphere and is the limiting factor in large aperture ground-based imaging systems. These fluctuations can also cause significant spreading of the spot-size of a laser propagating long distances through the atmosphere, significantly reducing the power on target. In the past few decades, advances in adaptive optical systems have made it feasible to approach resolutions near the diffraction limit for viewing objects beyond the atmosphere [6, 8, 12].

Many papers have developed simulation techniques that incorporate the phase perturbations caused by atmospheric turbulence [2, 4, 11, 12, 15], but optical field perturbations can take the form of both phase and amplitude perturbations. Even if perfect phase correction is applied by the adaptive optical system, it cannot correct for the amplitude perturbations. Therefore, to accurately evaluate the atmospheric turbulence effects, the amplitude perturbations should be considered. This thesis develops a random screen generator that simulates both the phase and amplitude optical field perturbations due to weak turbulence.

The amplitude perturbations effects on imaging have been studied to some degree, but there hasn't been much study in how the amplitude perturbations affect the phase measurements required in adaptive optical systems. This thesis will study the effects of amplitude perturbations on full aperture tilt estimation. The tilt estimation in an adaptive optics system is used to remove the overall phase tilt in the perturbed wavefront.

1.1 Atmospheric Turbulence Modeling

Modeling the effects of turbulence has received a great deal of attention. Most of the work on optical propagation through turbulence is based upon the seminal efforts of Fried, Kolmogorov, and Tatarski [3, 9, 13]. Kolmogorov suggested that over an extended propagation path the index of refraction differences could be modeled as homogeneous and isotropic random processes. Homogeneity implies the statistics of the turbulent flow are independent of the position within the turbulent flow. The isotropic assumption is much stronger since it implies homogeneity and also requires that the second and higher order statistics of the turbulence are only dependent upon the radial distance between any two points [6, 12].

Many papers have used the geometric optics calculation to model atmospheric turbulence effects on images taken through the earth's turbulent atmosphere [12, 15]. The geometric optics approach models the turbulence effects by integrating over the optical path differences which simply add phase to the propagating wave. The approach is often appropriate when there is little far-field turbulence (i.e., ground to space propagation). If, however, the turbulence is extended through the entire medium, the field encounters both phase and amplitude variations due to diffraction effects (i.e., propagation within the turbulence). In this thesis we will incorporate the phase and amplitude effects caused by atmospheric turbulence.

The phase perturbations have the effect of creating a wavefront randomly crinkled in appearance and propagating in a random direction (or tilt). The amplitude effects, often referred to as scintillation, create a speckled appearance in the intensity of the field. The amplitude and phase perturbations have the effect of degrading the image and widening the point spread function (psf). The random overall tilt of the wavefront phase perturbations

has the effect of moving the image around in space, but does not reduce its sharpness. If a very-short-exposure image is recorded (i.e., the tilt is removed), the psf can be significantly reduced and resolution enhanced. A large portion of the image degradation is due to the random tilt portion of the phase perturbations of the wavefront at the pupil [6, 12]. Since adaptive optics systems can only correct the phase perturbations, scintillation effects represent the theoretical limit one can achieve in adaptive optics systems.

First, the phase and amplitude effects of the random fluctuations on the optical field propagation must be predicted. The analysis presented here considers a diffraction calculation based upon the work of Lee and Harp to determine both the phase and amplitude perturbation effects caused by atmospheric turbulence on the wavefront in the aperture. The optical field statistics of the phase and amplitude perturbations used in this thesis are taken from the correlation functions developed by Lee and Harp [10]. In addition, the cross correlation of the phase and amplitude perturbations is derived for the first time in this thesis. The correlations are determined by modeling the turbulence as layers of randomly varying refractivity perpendicular to the propagation path. As the field propagates through the medium, diffraction occurs at each of the layers. Due to the weak turbulence assumption, the effects of the diffracted wave being diffracted again (second order effects) by subsequent layers is ignored. The weak index of refraction fluctuation model does not predict real effects of strong turbulence, such as the saturation of the log amplitude fluctuations. To represent the perturbations in the frequency domain the power spectral densities (psd)s are determined by taking the Fourier transform of the correlation functions.

Analysis of the correlation functions often results in difficult analytical solutions with no closed form. Therefore, simulations of the atmospheric turbulence are often used to determine how optical systems will perform [2, 4, 11, 12, 15]. These previous works only accounted for the phase effects of the turbulence. To investigate the effect of propagation through extended turbulence, amplitude effects must be incorporated as well.

In order to study the effects of the amplitude and phase perturbations screens will be generated to simulate the complete random optical field caused by the turbulence. A new method of atmospheric screen generation is developed for use in performance calcula-

tions of adaptive optics systems that is valid over a wide range of atmospheric turbulence parameters and incorporates both phase and amplitude effects. The generated random optical field over the aperture, $\hat{E}(\vec{x})$, can be represented as

$$\hat{E}(\vec{x}) = (1 + \hat{A}(\vec{x})) e^{j\hat{\phi}(\vec{x})}, \quad (1.1)$$

where $\hat{A}(\vec{x})$ represents the amplitude perturbations and $\hat{\phi}(\vec{x})$ represents the phase perturbations. The screen generator accounts for diffraction effects caused by turbulence and incorporates the phase, amplitude, and cross statistics of the weak turbulence model. The screen generation approach follows Welsh's paper on Fourier series (FS) based phase screen generation [15]. Welsh's relationship for the phase screen generation is extended by using the phase, *amplitude, and cross* psds. A modal representation is used to perform a FS expansion of the wavefront phase and amplitude over a square area. The screen generator uses the psds of the phase and amplitude perturbations, determined from the correlation functions, in the FS expansion. The screen also incorporates the cross psd derived in this thesis to ensure the cross statistics are satisfied.

1.2 Adaptive Optic Systems

Adaptive optic systems operate by measuring the wavefront phase of a reference guide star, laser guide star, or the glint off the object to be "imaged" and subtracting the phase from the object wavefront, resulting in an improvement in image quality [12,14]. On many systems, the wavefront measurements are made with a wavefront sensor (WFS) such as the Shack-Hartman sensor and a separate full-aperture tilt sensor. The measurements of the WFS and the tilt sensor are converted to electrical signals which drive actuators on the deformable mirror and the tip-tilt mirror, resulting in the desired phase correction. A simplified adaptive optics system is illustrated in Fig. 1.1. When the phase is perfectly measured and compensated by a system for a beacon along the same path as the object, theory predicts perfect phase correction [12]. The result of perfect correction in a phase only perturbed wavefront is referred to as diffraction limited performance.

However, adaptive optic systems can never reach perfect correction. Errors due to sampling and wavefront reconstruction will always exist. In addition, when the object and

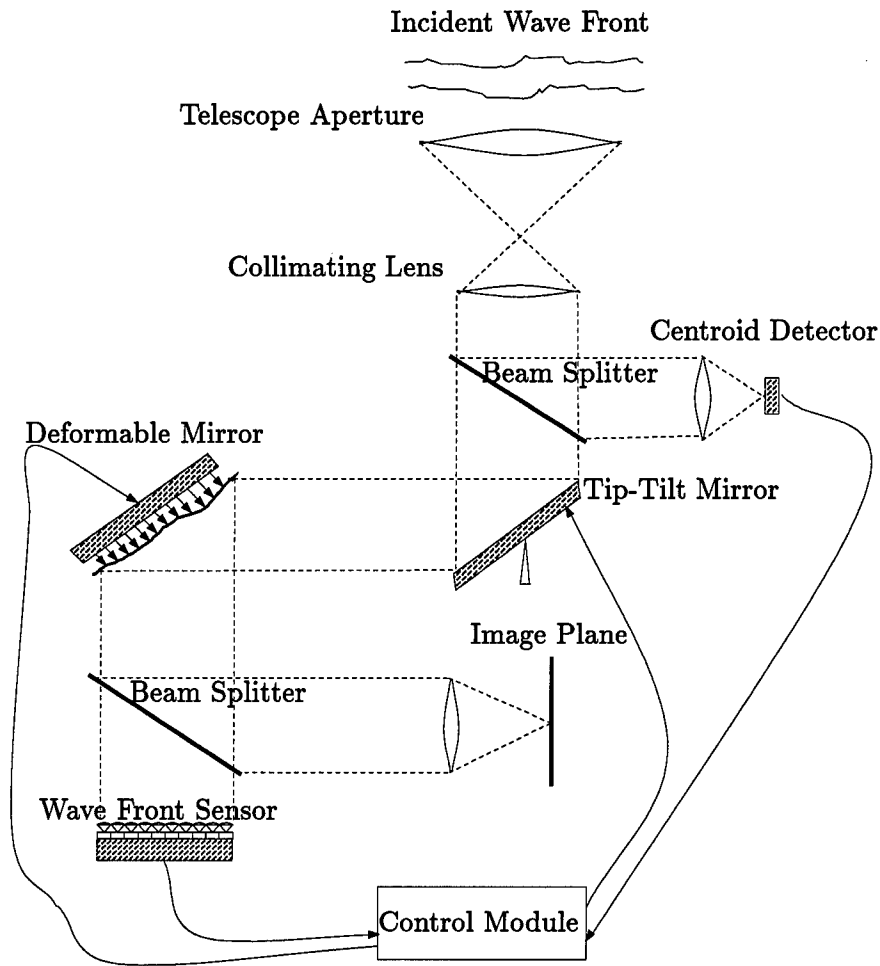


Figure 1.1 Simplified optical configuration of an adaptive optics imaging system

reference beacon are not collocated the light travels through different turbulence. Since the system is compensating for the beacon's turbulent path and not the turbulence the object sees, errors in the compensation result. This is called anisoplanatism. Furthermore, even if perfect phase correction is applied, the adaptive optics system cannot correct for the amplitude perturbations. Therefore, the theoretical limit of adaptive optic compensation is determined by these scintillation effects. To accurately evaluate total effects of the atmospheric turbulence the scintillation effects should be considered.

Scintillation effects in imaging have been studied to some degree, but there hasn't been much study in how the amplitude perturbations affect the phase measurements required in adaptive optic systems. This thesis studies the effects of scintillation on full

aperture tilt estimation in weak turbulence. The tilt estimation is used by the tip-tilt mirror in an adaptive optics system to remove the overall tilt in the wavefront. Monte-Carlo experiments using the random screen generator will be performed to investigate the effects of the amplitude perturbations on the full-aperture tilt estimation. Since the random tilt contains 87% of the power in the wavefront phase fluctuations, accurate wavefront tilt estimation is essential to an adaptive optics system. These experiments will use the random amplitude and phase perturbation screens produced by the screen generator developed in this thesis to determine the effect of the amplitude perturbations on the tilt estimation.

1.3 Summary of key results

The theoretical statistics were developed for the amplitude and phase perturbations of the optical field caused by weak turbulence. The statistics were applied in the development of a random optical field screen generator. The mean square value and the structure functions of the phase, amplitude, and cross terms are calculated in a Monte Carlo experiment using the screen generator to within 1% of the theoretical values for a number of screen dimensions. Monte Carlo experiments performed using the screen generator determined the amplitude perturbations can significantly reduce the accuracy of full-aperture tilt estimation using image centroid motion. However, using the combined amplitude and phase screen image centroid to estimate tilt correction allowed for a higher Strehl ratio than using only the phase to estimate the correction.

1.4 Overview

Chapter II develops the amplitude, phase, and cross correlation functions of the atmospheric turbulence. Chapter III determines the power spectral density (psd) functions of the atmospheric turbulence from the correlation functions. Chapter IV uses the psds developed in Chapter III to develop an atmospheric turbulence phase and amplitude screen generator. Chapter V studies the effect of the amplitude perturbations on the wavefront tilt estimation and the resulting Strehl ratios. Results are presented that indicate how amplitude perturbations affect the tilt estimation for various conditions of weak atmospheric

turbulence. Chapter VI gives some conclusions about the results and recommendations for further study.

II. Correlation Functions of Weak Turbulence

The purpose of this section is to develop the phase, amplitude and cross correlation functions for the optical field perturbations caused by atmospheric turbulence. A diffraction based calculation is used to develop the correlation functions associated with weak scattering through a random medium. The approach follows Lee and Harp's development and results in the same functions as in their paper [10]. In addition to the phase and amplitude correlations, the cross correlation is derived for the first time and follows an approach similar to Troxel's paper [14].

The turbulence induced random index of refraction is modeled with thin slabs of random refractivity perpendicular to the propagation path. Each slab is represented with a Fourier decomposition of random phase and varying spatial frequency (see Fig. 2.1). A wave is propagated from slab to slab where each slab can be treated as a phase-diffraction grating. At each slab, the incident wave is diffracted resulting in two diffracted orders and the original direction of propagation. Due to a weak scattering approximation only a single diffraction at each slab is allowed (i.e., the diffracted orders aren't allowed to diffract in subsequent layers). Therefore only the zeroth order has enough power to have a non-negligible effect at the next layer. The results are integrated over the spatial frequencies and every angle of the Fourier components to determine the amplitude and phase perturbations [10]. Finally, the random field perturbations in the amplitude and phase are used to calculate the amplitude, phase, and cross correlations.

The final solutions for the amplitude, phase and cross correlations are very similar in form and each include three multiplicative terms: a term relating the perturbations at one point with those at another point, the power spectrum of the refractive index, and a weighting term which accounts for the relative perturbations at a given position along the transmission path [10].

2.1 Derivation of Correlation Functions

Using the layered approach, the effect on the optical field can be represented as a differential amplitude perturbation and a differential residual phase at each slab or layer

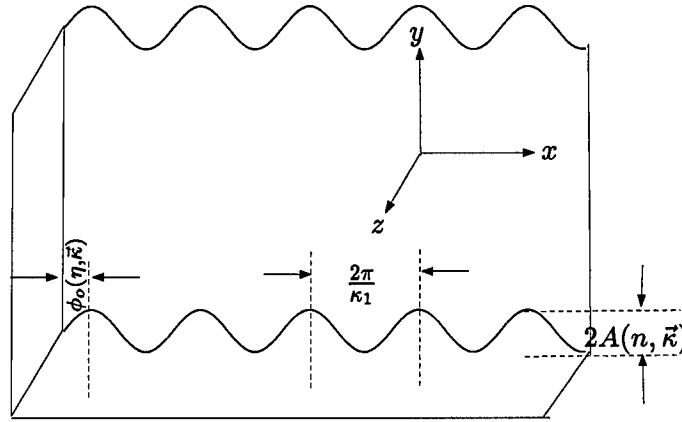


Figure 2.1 A cross section of the Fourier representation of the random refractivity slab, where $A(n, \vec{\kappa})$ is the amplitude, $\phi_o(\eta, \vec{\kappa})$ is the random phase and $\frac{\kappa_1}{2\pi}$ is the spatial frequency.

(see Fig. 2.1). The total amplitude perturbation represents the deviation from a unit amplitude. The total phase perturbation represents the total phase deviation induced by the refractive index perturbation. Lee and Harp derives the following differential phase and amplitude perturbations for propagation through weak turbulence modeled as the propagation through one of the differential slabs [10]

$$dP_a = -ka(\kappa)d\eta \cos(\kappa(x + b)) \sin[\eta(\sqrt{k^2 - \kappa^2} - k)] \quad (2.1)$$

and

$$dP_p = -ka(\kappa)d\eta \cos(\kappa(x + b)) \cos[\eta(\sqrt{k^2 - \kappa^2} - k)]. \quad (2.2)$$

Lee and Harp define k as the wavenumber, $2\pi/\lambda$; $a(\kappa)$ as the peak amplitude of the refractive index perturbations; b as the random phase of the refractive index; $d\eta$ as the differential propagation path length; η as the path length from the slab to the observation plane; x as the direction along which the periodic Fourier component is taken; and κ as the spatial frequency of the particular Fourier component.

Using the binomial expansion and the assumption that $\kappa \ll k$ the following factor can be simplified to

$$\sqrt{k^2 - \kappa^2} - k = k\left(\sqrt{1 - \frac{\kappa^2}{k^2}} - 1\right) \approx k\left[\left(1 - \frac{\kappa^2}{k^2}\right) - 1\right] = \frac{\kappa^2}{2k} = \alpha. \quad (2.3)$$

Now, Troxel represents the perturbations in three dimensions at a particular altitude, η , by

$$P_a(\eta, \vec{\kappa}, \vec{x}) = A(\eta, \vec{\kappa}) \cos(\vec{\kappa} \cdot \vec{x} + \phi_o(\eta, \kappa)) \sin(\eta\alpha) \quad (2.4)$$

and

$$P_p(\eta, \vec{\kappa}, \vec{x}) = -A(\eta, \vec{\kappa}) \cos(\vec{\kappa} \cdot \vec{x} + \phi_o(\eta, \kappa)) \cos(\eta\alpha), \quad (2.5)$$

where $A(\eta, \vec{\kappa})$ and $\phi_o(\eta, \vec{\kappa})$ are related to the amplitude and phase of the refractivity field Fourier component and \vec{x} is a position vector in the plane of the slab [14]. The total residual phase and amplitude perturbations are found by integrating over all slabs distributed along a path length, L , and all frequencies, $\vec{\kappa}$ and can be represented as

$$P_a(\vec{x}) = \int_0^L \int d\eta d\vec{\kappa} A(\eta, \vec{\kappa}) \cos(-\vec{\kappa} \cdot \vec{x} - \phi_o(\eta, \kappa)) \sin(\eta\alpha) \quad (2.6)$$

$$P_p(\vec{x}) = - \int_0^L \int d\eta d\vec{\kappa} A(\eta, \vec{\kappa}) \cos(-\vec{\kappa} \cdot \vec{x} - \phi_o(\eta, \kappa)) \cos(\eta\alpha), \quad (2.7)$$

where $\alpha = \kappa^2/(2k)$. Representing the perturbations in complex phasor notation, the amplitude perturbations and residual phase perturbations of the field can be written as

$$P_a(\vec{x}) = -\mathcal{R} \left\{ \int_0^L \int d\eta d\vec{\kappa} A(\eta, \vec{\kappa}) e^{-j\phi_o(\eta, \kappa)} e^{-j(\vec{\kappa} \cdot \vec{x})} \sin(\eta\alpha) \right\} \quad (2.8)$$

and

$$P_p(\vec{x}) = -\mathcal{R} \left\{ \int_0^L \int d\eta d\vec{\kappa} A(\eta, \vec{\kappa}) e^{-j\phi_o(\eta, \kappa)} e^{-j(\vec{\kappa} \cdot \vec{x})} \cos(\eta\alpha) \right\}, \quad (2.9)$$

where \mathcal{R} is an operator that takes the real portion of a complex quantity. The \mathcal{R} operator is now dropped and the work continues with the complex phasor representations $\underline{P_a(\vec{x})}$ and $\underline{P_p(\vec{x})}$ given by

$$\underline{P_a(\vec{x})} = \int_0^L \int d\eta d\vec{\kappa} \tilde{A}(\eta, \vec{\kappa}) e^{-j(\vec{\kappa} \cdot \vec{x})} \sin(\eta\alpha) \quad (2.10)$$

and

$$\underline{P_p}(\vec{x}) = \int_0^L \int_0^\infty d\eta d\kappa \tilde{A}(\eta, \kappa) e^{-j(\vec{\kappa} \cdot \vec{x})} \cos(\eta\alpha), \quad (2.11)$$

where $\tilde{A}(\eta, \kappa) = A(\eta, \kappa) e^{-j\phi_o(\eta, \kappa)}$ and $\alpha = \kappa^2/(2k)$ [14].

From Eqs. (2.10) and (2.11) above the development of the amplitude and phase correlations directly follows Troxel's approach [14]. The amplitude and phase correlations are defined as the ensemble average of the perturbations at two different locations separated by \vec{d} and can be represented as

$$\Gamma_{aa}(\vec{d}) = \langle P_a(\vec{x}) P_a(\vec{x} - \vec{d}) \rangle \quad (2.12)$$

and

$$\Gamma_{pp}(\vec{d}) = \langle P_p(\vec{x}) P_p(\vec{x} - \vec{d}) \rangle, \quad (2.13)$$

where the angle brackets denote the expected value of the argument.

Lee and Harp determines the correlations of the amplitude and phase perturbations in weak turbulence as the following

$$\Gamma_{aa}(\vec{d}) = 4k^2 \pi^2 \int_0^L \int_0^\infty d\kappa d\eta \kappa J_0(\kappa d) \Phi(\kappa) \sin^2(\alpha\eta), \quad (2.14)$$

and

$$\Gamma_{pp}(\vec{d}) = 4k^2 \pi^2 \int_0^L \int_0^\infty d\kappa d\eta \kappa J_0(\kappa d) \Phi(\kappa) \cos^2(\alpha\eta), \quad (2.15)$$

where $\alpha = \frac{\kappa^2}{2k}$ and J_0 is the zeroth order Bessel function of the first kind [10]. Equations (2.14) and (2.15) are the key equations that describe the second order statistics of the amplitude and phase effects due to weak turbulence. These equations form the basis for all other statistical representations of the field effects due to the atmospheric turbulence in this thesis.

Another key second order statistic is required to define the atmospheric turbulence effects on the optical field. In order to investigate how the phase and amplitude perturbations are related one needs to know how they are correlated (i.e., their cross correlation). The cross correlation is defined as the ensemble average of the amplitude and phase perturbations taken at two different locations separated by \vec{d} . The method used here is very

similar to the approach used by Troxel to derive the angle dependent phase and amplitude correlation functions [14]. Using the perturbation relationships in Eqs. (2.10) and (2.11), the cross correlation can be determined by

$$\begin{aligned}\underline{\Gamma_{ap}(\vec{d})} &= \langle P_a(\vec{x})P_p^*(\vec{x}-\vec{d}) \rangle, \\ &= \left\langle \int \int \int_0^L \int_0^L d\eta_1 d\eta_2 d\vec{\kappa}_1 d\vec{\kappa}_2 \tilde{A}(\eta_1, \vec{\kappa}_1) e^{-j(\vec{\kappa}_1 \cdot \vec{x})} \sin(\eta_1 \alpha_1) \right. \\ &\quad \left. \times \tilde{A}^*(\eta_2, \vec{\kappa}_2) e^{j(\vec{\kappa}_2 \cdot (\vec{x}-\vec{d}))} \cos(\eta_2 \alpha_2) \right\rangle.\end{aligned}\quad (2.16)$$

Since the only random quantities are in the \tilde{A} terms, the other deterministic terms can be passed through the expectation.

$$\begin{aligned}\underline{\Gamma_{ap}(\vec{d})} &= \int \int \int_0^L \int_0^L d\eta_1 d\eta_2 d\vec{\kappa}_1 d\vec{\kappa}_2 \left\langle \tilde{A}(\eta_1, \vec{\kappa}_1) \tilde{A}^*(\eta_2, \vec{\kappa}_2) \right\rangle \\ &\quad \times e^{-j(\vec{\kappa}_1 \cdot \vec{x})} \sin(\eta_1 \alpha_1) e^{j(\vec{\kappa}_2 \cdot (\vec{x}-\vec{d}))} \cos(\eta_2 \alpha_2).\end{aligned}\quad (2.17)$$

Troxel uses the following relationship derived from a Tatarski relation to perform the expectation:

$$\left\langle \tilde{A}(\eta_1, \vec{\kappa}_1) \tilde{A}^*(\eta_2, \vec{\kappa}_2) \right\rangle = 8\pi k^2 \delta(\vec{\kappa}_1 - \vec{\kappa}_2) \delta(\eta_1 - \eta_2) \Phi(\vec{\kappa}_1, \eta_1), \quad (2.18)$$

where $\Phi(\kappa, \eta)$ is the three dimensional refractive index power spectrum with $\kappa^2 = \kappa_x^2 + \kappa_y^2$, and δ is the Dirac delta function [13, 14]. The $\delta(\eta_1 - \eta_2)$ part of Eq. (2.18) is a derived relation and should not be considered as a statement of independence of turbulent layers. Substituting Eq. (2.18) into Eq. (2.17) gives

$$\underline{\Gamma_{ap}(\vec{d})} = 8k^2 \pi \int \int_0^L d\eta d\vec{\kappa} \Phi(\vec{\kappa}, \eta) \sin(\alpha\eta) \cos(\alpha\eta) e^{-j\vec{\kappa} \cdot \vec{d}} \quad (2.19)$$

and using a trigonometric identity the relation becomes

$$\underline{\Gamma_{ap}(\vec{d})} = 4k^2 \pi \int \int_0^L d\eta d\vec{\kappa} \Phi(\vec{\kappa}, \eta) \sin(2\alpha\eta) e^{-j\vec{\kappa} \cdot \vec{d}}. \quad (2.20)$$

The following relation from Goodman illustrates that the real part of the complex correlation is twice the real valued cross correlation:

$$\Gamma_{uv}(\tau) = 2\Gamma_{uv}^{(r,r)}(\tau) + j2\Gamma_{uv}^{(i,r)}(\tau), \quad (2.21)$$

where $\Gamma_{uv}^{(r,r)}(\tau)$ is the real correlation [6]. Therefore, the real correlation is half the real portion of the complex one (i.e. $\Gamma_{ap}(\vec{d}) = \frac{1}{2}\mathcal{R}\{\Gamma_{ap}(\vec{d})\}$). The real correlation can now be represented as

$$\Gamma_{ap}(\vec{d}) = 2k^2\pi \int_0^L \int_0^\pi d\eta d\vec{\kappa} \Phi(\vec{\kappa}, \eta) \sin(2\alpha\eta) \cos(\vec{\kappa} \cdot \vec{d}). \quad (2.22)$$

The vector representation can be changed to polar coordinates where $d\vec{\kappa} = \kappa d\kappa d\theta$. The integration over $d\theta$ goes from 0 to π . The integration over $d\theta$ can then be performed using the relation

$$\int_0^\pi d\theta \cos(a \cos(\theta)) = \pi J_0(a), \quad (2.23)$$

where J_0 is the zeroth order Bessel function of the first kind. Finally, the cross correlation can be represented as

$$\begin{aligned} \Gamma_{ap}(\vec{d}) &= 2k^2\pi \int_0^L \int_0^\infty \int_0^\pi d\theta d\kappa d\eta \kappa \cos(\kappa d \cos(\theta)) \Phi(\kappa, \eta) \sin(2\alpha\eta) \\ &= 2k^2\pi^2 \int_0^L \int_0^\infty d\kappa d\eta \kappa J_0(\kappa d) \Phi(\kappa, \eta) \sin(2\alpha\eta). \end{aligned} \quad (2.24)$$

Equation (2.24) is the cross-correlation of the amplitude and phase perturbations of the optical field due to weak turbulence. This equation will be used throughout this thesis to represent statistics of the cross terms of the phase and amplitude.

2.2 Correlations for a constant strength of turbulence

In order to proceed with the correlations developed in this section they need to be related to a particular turbulent medium. The 3-D turbulence power spectrum of the refractive index, $\Phi(\kappa, \eta)$, is a function of both the turbulence along the path and the frequency distribution. The following relation essentially breaks up the functional

dependence of the 3-D power spectrum into the turbulence strength profile $C_n^2(\eta)$ and a normalized power spectral density $\Phi_0(\kappa)$. It can be represented as the following [6,12]

$$\Phi(\kappa, \eta) = 0.033 C_n^2(\eta) \Phi_0(\kappa), \quad (2.25)$$

where $C_n^2(\eta)$ represents the strength of turbulence along the path. The von Karman turbulence power spectrum definition for $\Phi_0(\kappa)$ uses an inner scale, L_m , and outer scale, L_o , to represent the smallest and largest turbulence scale sizes, respectively, in a particular medium. L_o is usually on the order of ten to twenty meters, where as L_m is usually only a few millimeters [12]. The von Karman spectrum, $\Phi_0(\kappa)$, is defined as [12]

$$\Phi_0(\kappa) = \frac{e^{-\frac{\kappa^2 L_m^2}{4\pi^2}}}{(\kappa^2 + \frac{4\pi^2}{L_o^2})^{11/6}}. \quad (2.26)$$

Using Eq. (2.25), the amplitude, phase and cross correlations given in Eqs. (2.14), (2.15), and (2.24) can be written as

$$\begin{aligned} \Gamma_{aa}(\vec{d}) &= 4k^2 \pi^2 \int_0^\infty \int_0^L d\eta d\kappa \kappa J_0(\kappa d) \Phi(\kappa, \eta) \sin^2(\alpha\eta) \\ &= 4k^2 \pi^2 (0.033) \int_0^\infty d\kappa \kappa J_0(\kappa d) \Phi_0(\kappa) \int_0^L d\eta C_n^2(\eta) \sin^2(\alpha\eta), \end{aligned} \quad (2.27)$$

and

$$\begin{aligned} \Gamma_{pp}(\vec{d}) &= 4k^2 \pi^2 \int_0^\infty \int_0^L d\eta d\kappa \kappa J_0(\kappa d) \Phi(\kappa, \eta) \cos^2(\alpha\eta) \\ &= 4k^2 \pi^2 (0.033) \int_0^\infty d\kappa \kappa J_0(\kappa d) \Phi_0(\kappa) \int_0^L d\eta C_n^2(\eta) \cos^2(\alpha\eta), \end{aligned} \quad (2.28)$$

and

$$\begin{aligned} \Gamma_{ap}(\vec{d}) &= 2k^2 \pi^2 \int_0^\infty \int_0^L d\eta d\kappa \kappa J_0(\kappa d) \Phi(\kappa, \eta) \sin(2\alpha\eta) \\ &= 2k^2 \pi^2 (0.033) \int_0^\infty d\kappa \kappa J_0(\kappa d) \Phi_0(\kappa) \int_0^L d\eta C_n^2(\eta) \sin(2\alpha\eta). \end{aligned} \quad (2.29)$$

To compare the correlations above let's assume the strength of turbulence is constant over the entire length of propagation. For horizontal propagation through the atmosphere

constant turbulence is a good approximation, but for propagation up through the atmosphere it is not such a good approximation, since strength of turbulence has a strong dependence on altitude. The total turbulence over the entire path is defined as

$$\int_0^L d\eta C_n^2(\eta) = \left(\frac{0.185}{r_0}\right)^{5/3} (\lambda^2), \quad (2.30)$$

where r_0 is the Fried parameter of the turbulence and λ is the average wavelength of the light [3]. The Fried parameter can be interpreted as the limiting aperture size beyond which no increase in resolution occurs.

Using Eq. (2.30), now the correlations can be integrated over the path length and calculated as the following

$$\begin{aligned} \Gamma_{aa}(\vec{d}) &= 4k^2\pi^2(0.033)\frac{\lambda^2}{L}\left(\frac{0.185}{r_0}\right)^{5/3}\int_0^\infty d\kappa\kappa J_0(\kappa d)\Phi_0(\kappa)\int_0^L d\eta\sin^2(\alpha\eta) \\ &= 4k^2\pi^2(0.033)\frac{\lambda^2}{L}\left(\frac{0.185}{r_0}\right)^{5/3}\int_0^\infty d\kappa\kappa J_0(\kappa d)\Phi_0(\kappa)\left[\frac{L}{2}-\frac{1}{4\alpha}\sin(2\alpha L)\right] \\ &= 8\pi^4(0.033)\left(\frac{0.185}{r_0}\right)^{5/3}\int_0^\infty d\kappa\kappa J_0(\kappa d)\Phi_0(\kappa)\left[1-\frac{1}{2\alpha L}\sin(2\alpha L)\right], \quad (2.31) \end{aligned}$$

and

$$\begin{aligned} \Gamma_{pp}(\vec{d}) &= 4k^2\pi^2(0.033)\frac{\lambda^2}{L}\left(\frac{0.185}{r_0}\right)^{5/3}\int_0^\infty d\kappa\kappa J_0(\kappa d)\Phi_0(\kappa)\int_0^L d\eta\cos^2(\alpha\eta) \\ &= 4k^2\pi^2(0.033)\frac{\lambda^2}{L}\left(\frac{0.185}{r_0}\right)^{5/3}\int_0^\infty d\kappa\kappa J_0(\kappa d)\Phi_0(\kappa)\left[\frac{L}{2}+\frac{1}{4\alpha}\sin(2\alpha L)\right] \\ &= 8\pi^4(0.033)\left(\frac{0.185}{r_0}\right)^{5/3}\int_0^\infty d\kappa\kappa J_0(\kappa d)\Phi_0(\kappa)\left[1+\frac{1}{2\alpha L}\sin(2\alpha L)\right], \quad (2.32) \end{aligned}$$

and

$$\begin{aligned} \Gamma_{ap}(\vec{d}) &= 2k^2\pi^2(0.033)\frac{\lambda^2}{L}\left(\frac{0.185}{r_0}\right)^{5/3}\int_0^\infty d\kappa\kappa J_0(\kappa d)\Phi_0(\kappa)\int_0^L d\eta\sin(2\alpha\eta) \\ &= 2k^2\pi^2(0.033)\frac{\lambda^2}{L}\left(\frac{0.185}{r_0}\right)^{5/3}\int_0^\infty d\kappa\kappa J_0(\kappa d)\Phi_0(\kappa)\frac{1}{\alpha}\sin^2(\alpha L) \\ &= 8\pi^4(0.033)\left(\frac{0.185}{r_0}\right)^{5/3}\int_0^\infty d\kappa\kappa J_0(\kappa d)\Phi_0(\kappa)\frac{1}{\alpha L}\sin^2(\alpha L), \quad (2.33) \end{aligned}$$

where $\alpha = \frac{|\vec{k}|^2}{2k} = \frac{\lambda\kappa^2}{4\pi}$.

In order to present these correlations more clearly, it is also convenient to perform a change of variables when calculating the correlations. Let $\kappa' = \kappa L_o$. Performing the change of variables results in

$$\begin{aligned}\Gamma_{aa}(\vec{d}) &= 8\pi^4(0.033)(0.185)^{5/3} \left(\frac{L_o}{r_o}\right)^{5/3} \int_0^\infty d\kappa' \kappa' \frac{1}{(\kappa'^2 + 4\pi^2)^{11/6}} \\ &\quad \times J_0\left(\frac{\kappa' d}{L_o}\right) \left[1 - \frac{2\pi L_o^2}{\lambda L \kappa'^2} \sin\left(\frac{\lambda L \kappa'^2}{2\pi L_o^2}\right)\right],\end{aligned}\quad (2.34)$$

and

$$\begin{aligned}\Gamma_{pp}(\vec{d}) &= 8\pi^4(0.033)(0.185)^{5/3} \left(\frac{L_o}{r_o}\right)^{5/3} \int_0^\infty d\kappa' \kappa' \frac{1}{(\kappa'^2 + 4\pi^2)^{11/6}} \\ &\quad \times J_0\left(\frac{\kappa' d}{L_o}\right) \left[1 + \frac{2\pi L_o^2}{\lambda L \kappa'^2} \sin\left(\frac{\lambda L \kappa'^2}{2\pi L_o^2}\right)\right],\end{aligned}\quad (2.35)$$

and

$$\begin{aligned}\Gamma_{ap}(\vec{d}) &= 8\pi^4(0.033)(0.185)^{5/3} \left(\frac{L_o}{r_o}\right)^{5/3} \int_0^\infty d\kappa' \kappa' \frac{1}{(\kappa'^2 + 4\pi^2)^{11/6}} \\ &\quad \times J_0\left(\frac{\kappa' d}{L_o}\right) \left(\frac{4\pi L_o^2}{\lambda L \kappa'^2}\right) \sin^2\left(\frac{\lambda L \kappa'^2}{4\pi L_o^2}\right),\end{aligned}\quad (2.36)$$

where we have approximated the exponential in Eq. (2.26) as being approximately one. Numerical integration was performed over κ' for the correlations above for a strength of turbulence, $L_o/r_o = 100$, and $\frac{L_o^2}{\lambda L} = 20000$. The correlation plots are shown in Figs. 2.2, 2.3, and 2.4. Notice how much wider $\Gamma_{pp}(\vec{d})$ is than $\Gamma_{aa}(\vec{d})$ and $\Gamma_{ap}(\vec{d})$. This trend indicates that the phase perturbations are spatially correlated over a larger area than the amplitude perturbations.

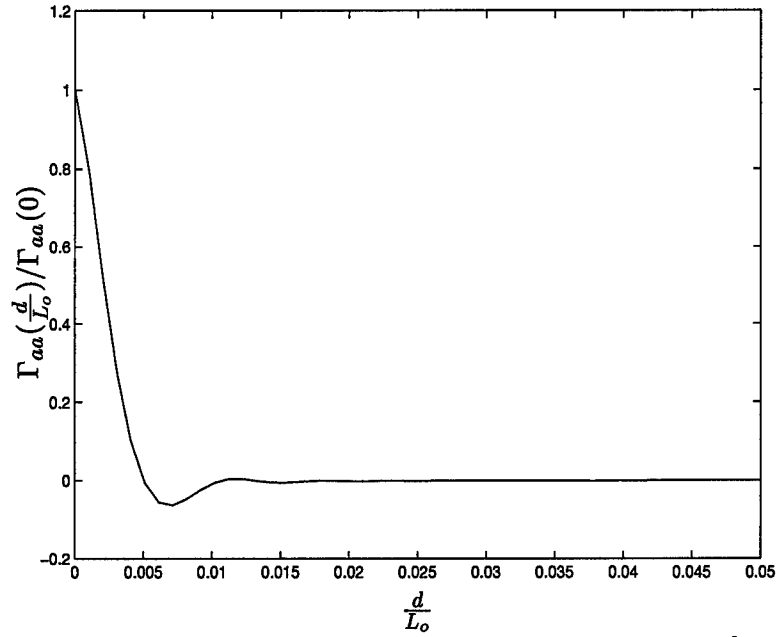


Figure 2.2 The normalized amplitude correlation is plotted versus $\frac{d}{L_o}$ for a strength of turbulence, $L_o/r_o = 100$, and $\frac{L_o^2}{\lambda L} = 20000$.

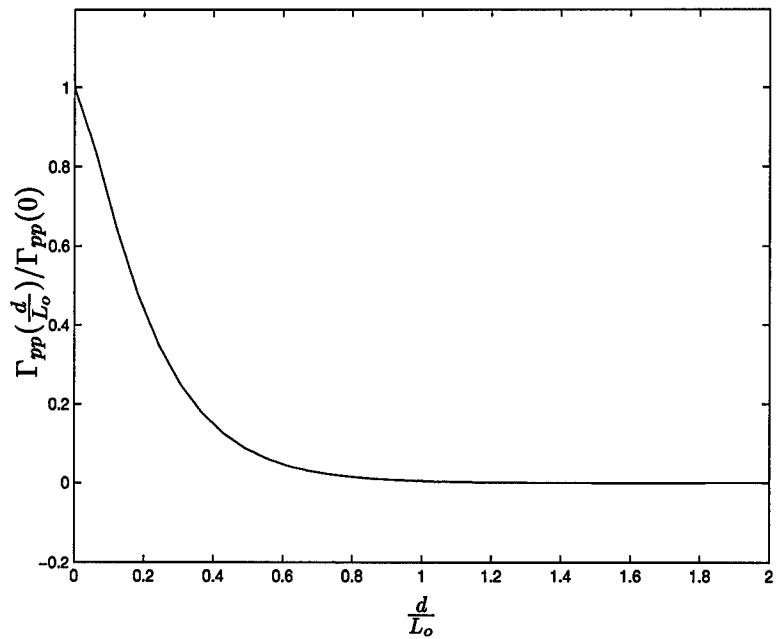


Figure 2.3 The normalized phase correlation is plotted versus $\frac{d}{L_o}$ for a strength of turbulence, $L_o/r_o = 100$, and $\frac{L_o^2}{\lambda L} = 20000$.

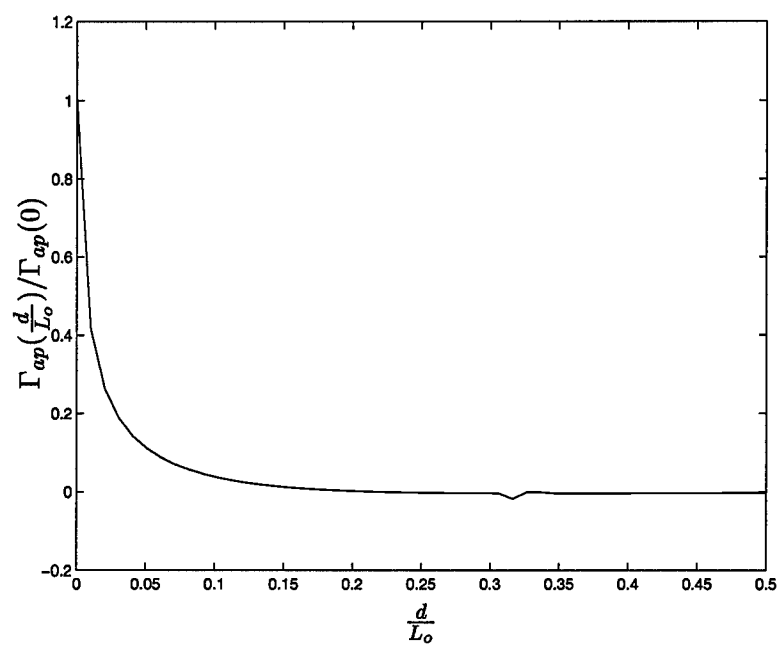


Figure 2.4 The normalized cross correlation is plotted versus $\frac{d}{L_o}$ for a strength of turbulence, $L_o/r_o = 100$, and $\frac{L_o^2}{\lambda L} = 20000$.

2.3 Structure Functions

The structure functions for these perturbations can be represented as [6, 12]

$$\begin{aligned}
 D_{aa}(\vec{d}) &= 2\Gamma_{aa}(0) - 2\Gamma_{aa}(\vec{d}), \\
 &= 16\pi^4(0.033)(0.185)^{5/3} \left(\frac{L_o}{r_o}\right)^{5/3} \int_0^\infty d\kappa' \kappa' \frac{1}{(\kappa'^2 + 4\pi^2)^{11/6}} \\
 &\quad \times \left[1 - J_0\left(\frac{\kappa' d}{L_o}\right)\right] \left[1 - \frac{2\pi L_o^2}{\lambda L \kappa'^2} \sin\left(\frac{\lambda L \kappa'^2}{2\pi L_o^2}\right)\right], \tag{2.37}
 \end{aligned}$$

and

$$\begin{aligned}
 D_{pp}(\vec{d}) &= 2\Gamma_{pp}(0) - 2\Gamma_{pp}(\vec{d}), \\
 &= 16\pi^4(0.033)(0.185)^{5/3} \left(\frac{L_o}{r_o}\right)^{5/3} \int_0^\infty d\kappa' \kappa' \frac{1}{(\kappa'^2 + 4\pi^2)^{11/6}} \\
 &\quad \times \left[1 - J_0\left(\frac{\kappa' d}{L_o}\right)\right] \left[1 + \frac{2\pi L_o^2}{\lambda L \kappa'^2} \sin\left(\frac{\lambda L \kappa'^2}{2\pi L_o^2}\right)\right], \tag{2.38}
 \end{aligned}$$

and

$$\begin{aligned}
 D_{ap}(\vec{d}) &= 2\Gamma_{ap}(0) - 2\Gamma_{ap}(\vec{d}), \\
 &= 16\pi^4(0.033)(0.185)^{5/3} \left(\frac{L_o}{r_o}\right)^{5/3} \int_0^\infty d\kappa' \kappa' \frac{1}{(\kappa'^2 + 4\pi^2)^{11/6}} \\
 &\quad \times \left[1 - J_0\left(\frac{\kappa' d}{L_o}\right)\right] \left(\frac{4\pi L_o^2}{\lambda L \kappa'^2}\right) \sin^2\left(\frac{\lambda L \kappa'^2}{4\pi L_o^2}\right). \tag{2.39}
 \end{aligned}$$

The wave structure function is the sum of the phase and amplitude structure functions [6, 12]

$$\begin{aligned}
 D(\vec{d}) &= D_{pp}(\vec{d}) + D_{aa}(\vec{d}) \\
 &= 32\pi^4(0.033)(0.185)^{5/3} \left(\frac{L_o}{r_o}\right)^{5/3} \int_0^\infty d\kappa' \kappa' \frac{1}{(\kappa'^2 + 4\pi^2)^{11/6}} \\
 &\quad \times \left[1 - J_0\left(\frac{\kappa' d}{L_o}\right)\right]. \tag{2.40}
 \end{aligned}$$

2.4 Mean Square Value Functions

The mean square value of the amplitude and phase can be calculated easily from the correlations. Letting d go to zero in Eqs. (2.34), (2.35), and (2.36) we get the ensemble average of the squared phase and amplitude perturbations or the mean square values. These can be represented as follows

$$\begin{aligned}\Gamma_{aa}(0) &= 8\pi^4(0.033)(0.185)^{5/3} \left(\frac{L_o}{r_o}\right)^{5/3} \int_0^\infty d\kappa' \kappa' \frac{1}{(\kappa'^2 + 4\pi^2)^{11/6}} \\ &\times \left[1 - \frac{2\pi L_o^2}{\lambda L \kappa'^2} \sin\left(\frac{\lambda L \kappa'^2}{2\pi L_o^2}\right) \right],\end{aligned}\quad (2.41)$$

and

$$\begin{aligned}\Gamma_{pp}(0) &= 8\pi^4(0.033)(0.185)^{5/3} \left(\frac{L_o}{r_o}\right)^{5/3} \int_0^\infty d\kappa' \kappa' \frac{1}{(\kappa'^2 + 4\pi^2)^{11/6}} \\ &\times \left[1 + \frac{2\pi L_o^2}{\lambda L \kappa'^2} \sin\left(\frac{\lambda L \kappa'^2}{2\pi L_o^2}\right) \right],\end{aligned}\quad (2.42)$$

and

$$\begin{aligned}\Gamma_{ap}(0) &= 8\pi^4(0.033)(0.185)^{5/3} \left(\frac{L_o}{r_o}\right)^{5/3} \int_0^\infty d\kappa' \kappa' \frac{1}{(\kappa'^2 + 4\pi^2)^{11/6}} \\ &\times \left(\frac{4\pi L_o^2}{\lambda L \kappa'^2} \right) \sin^2\left(\frac{\lambda L \kappa'^2}{4\pi L_o^2}\right).\end{aligned}\quad (2.43)$$

Normally, as the propagation path or wavelength increases L_o/r_o increases and the turbulence effects are stronger. For the following plots the strength of turbulence, L_o/r_o , is held constant to show the relative mean square values of the phase and amplitude perturbations. Figure 2.5 shows the mean square value of the amplitude perturbations as a function of $\frac{L_o^2}{\lambda L}$ for different strengths of turbulence, L_o/r_o . For constant L_o/r_o , notice how the amplitude perturbations decrease substantially as $\frac{L_o^2}{\lambda L}$ gets large. On the other hand, the phase contribution, plotted in Fig. 2.6, gets very large for large $\frac{L_o^2}{\lambda L}$. Note also, the sum of the phase and amplitude mean square values is invariant to $\frac{L_o^2}{\lambda L}$ for constant L_o/r_o . For instance, for $L_o/r_o = 100$ the sum of the phase and amplitude mean square

values is 186.65. The mean cross value, $\Gamma_{ap}(0)$, of the phase and amplitude perturbations is plotted in Fig. 2.7. Notice how $\Gamma_{ap}(0)$ decreases as $\frac{L_o^2}{\lambda L}$ increases similar to the amplitude perturbations in $\Gamma_{aa}(0)$.

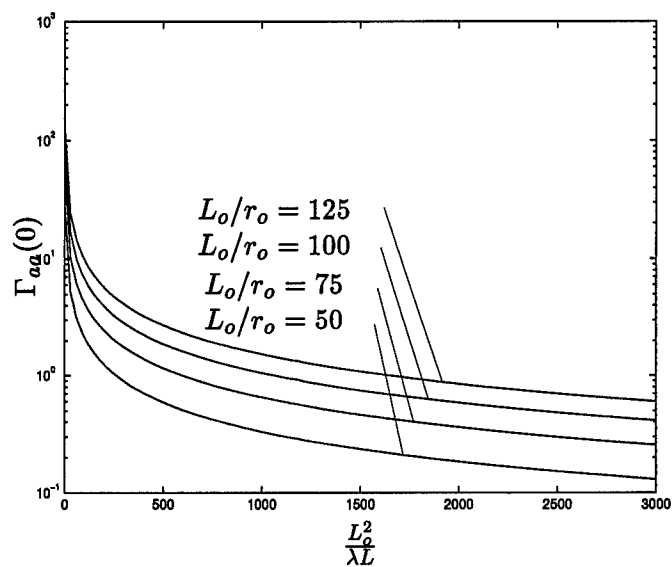


Figure 2.5 The mean square value of the amplitude perturbations in the pupil are plotted for different strengths of turbulence, L_o/r_o .

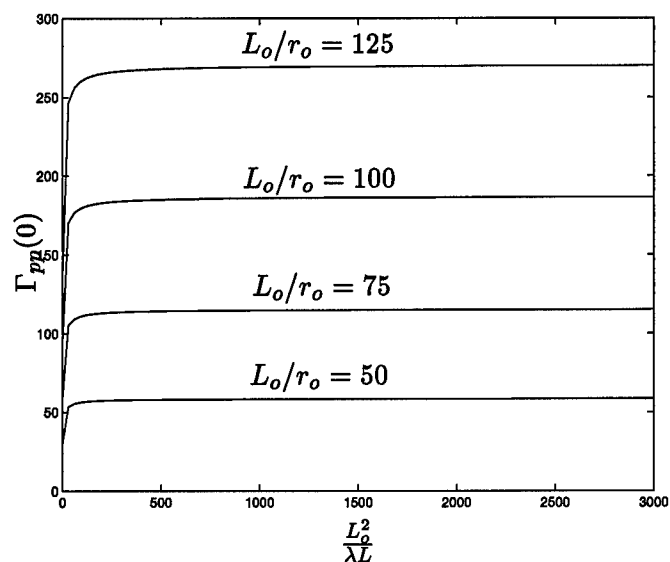


Figure 2.6 The mean square value of the phase perturbations in the pupil are plotted for different strengths of turbulence, L_o/r_o .

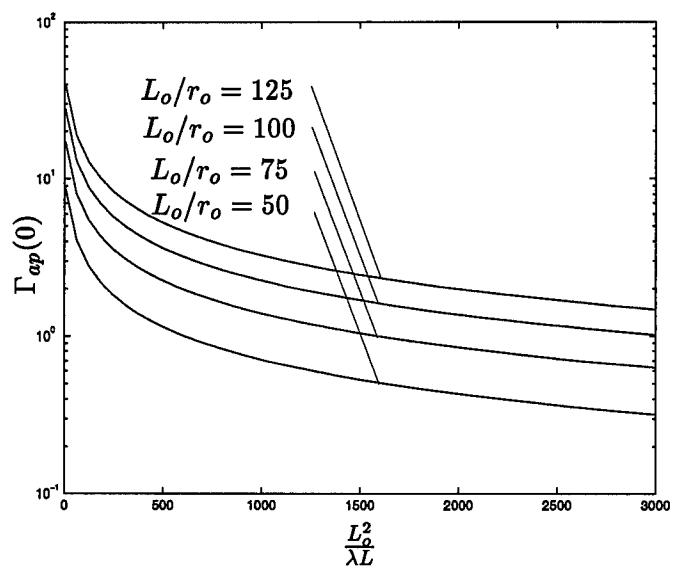


Figure 2.7 The mean cross value of the phase and amplitude perturbations in the pupil are plotted for different strengths of turbulence, L_o/r_o .

III. Phase, Amplitude, and Cross Power Spectral Densities of Weak Turbulence

Often it is convenient to represent the perturbations in the frequency domain to get a better idea of the strength of turbulence and the perturbations at the pupil. The frequency domain representations, the power spectral densities (psds), are developed from the correlations introduced in the previous section. The psds are calculated by taking the Fourier transform of the correlation functions [6]. The psds developed in this chapter will be used to create random phase and amplitude field screens with the correct first and second order statistics in the next chapter.

To begin, below are the phase, amplitude and cross correlation functions of the field perturbations due to the refractive index perturbations that were developed in Eqs.(2.15), (2.14), and (2.24) in the last chapter

$$\Gamma_{aa}(d) = 4k^2\pi^2 \int_0^L \int_0^\infty d\kappa d\eta \kappa J_0(\kappa d) \Phi(\kappa) \sin^2(\alpha\eta), \quad (3.1)$$

and

$$\Gamma_{pp}(d) = 4k^2\pi^2 \int_0^L \int_0^\infty d\kappa d\eta \kappa J_0(\kappa d) \Phi(\kappa) \cos^2(\alpha\eta), \quad (3.2)$$

and

$$\Gamma_{ap}(d) = 2k^2\pi^2 \int_0^L \int_0^\infty d\kappa d\eta \kappa J_0(\kappa d) \Phi(\kappa) \sin(2\alpha\eta), \quad (3.3)$$

where $\alpha = \frac{|\vec{\kappa}|^2}{2k}$.

The definitions of the Fourier Bessel transform and inverse transform are the following [6]

$$\begin{aligned} F(\rho) &= \mathcal{F}\{f(x)\} \\ &= \int_0^\infty 2\pi dx f(x) x J_0(2\pi\rho x) \end{aligned} \quad (3.4)$$

and

$$\begin{aligned} f(x) &= \mathcal{F}^{-1}\{F(\rho)\} \\ &= \int_0^\infty 2\pi d\rho F(\rho) \rho J_0(2\pi\rho x). \end{aligned} \quad (3.5)$$

The Fourier Bessel transform is used to perform a Fourier transform of a function represented in polar coordinates. If the correlations are represented in polar coordinates, the Fourier Bessel transform definition above can be utilized to perform the Fourier transform. After making a change in variables to polar coordinates, where $\kappa = 2\pi\rho$, $d\kappa = 2\pi d\rho$, and $\alpha = (4\pi^2 |\vec{\rho}|^2)/(2k)$, the correlation function for the amplitude can be written as the following

$$\begin{aligned}\Gamma_{aa}(d) &= 4k^2\pi^2 \int_0^L d\eta \int_0^\infty 2\pi d\rho \Phi(2\pi\rho, \eta) \sin^2(\alpha\eta) 2\pi\rho J_0(2\pi\rho d) \\ &= 8k^2\pi^3 \int_0^L d\eta \mathcal{F}^{-1} \left\{ \Phi(2\pi\rho, \eta) \sin^2(\alpha\eta) \right\}.\end{aligned}\quad (3.6)$$

Utilizing the Wiener Khinchin theorem, the psd can be found by taking the Fourier transform of the correlation function [6]. Performing the Fourier transform on the amplitude correlation function above yields the following equation:

$$\begin{aligned}\Phi_{aa}(\rho) &= \mathcal{F}\{\Gamma_{pp}(d)\} \\ &= \mathcal{F} \left\{ 8k^2\pi^3 \int_0^L d\eta \mathcal{F}^{-1} \left\{ \Phi(\kappa, \eta) \sin^2(\alpha\eta) \right\} \right\} \\ &= 8k^2\pi^3 \int_0^L d\eta \Phi(2\pi\rho, \eta) \sin^2(\alpha\eta).\end{aligned}\quad (3.7)$$

After making the same change in variables as before, the phase correlation can be written as the following

$$\begin{aligned}\Gamma_{pp}(d) &= 4k^2\pi^2 \int_0^L d\eta \int_0^\infty 2\pi d\rho \Phi(2\pi\rho, \eta) \cos^2(\alpha\eta) 2\pi\rho J_0(2\pi\rho d) \\ &= 8k^2\pi^3 \int_0^L d\eta \mathcal{F}^{-1} \left\{ \Phi(2\pi\rho, \eta) \cos^2(\alpha\eta) \right\},\end{aligned}\quad (3.8)$$

where $\kappa = 2\pi\rho$ and $d\kappa = 2\pi d\rho$ and now $\alpha = (4\pi^2 |\vec{\rho}|^2)/(2k)$.

Similarly, applying the Fourier transform to the phase correlation function above yields the following equation for the phase psd

$$\begin{aligned}
\Phi_{pp}(\rho) &= \mathcal{F}\{\Gamma_{pp}(d)\} \\
&= \mathcal{F}\left\{8k^2\pi^3 \int_0^L d\eta \mathcal{F}^{-1}\left\{\Phi(\kappa, \eta) \cos^2(\alpha\eta)\right\}\right\} \\
&= 8k^2\pi^3 \int_0^L d\eta \Phi(2\pi\rho, \eta) \cos^2(\alpha\eta).
\end{aligned} \tag{3.9}$$

Similarly, the cross correlation function can be written as the following

$$\begin{aligned}
\Gamma_{ap}(d) &= 2k^2\pi^2 \int_0^L d\eta \int_0^\infty 2\pi d\rho \Phi(2\pi\rho, \eta) \sin(2\alpha\eta) 2\pi\rho J_0(2\pi\rho d) \\
&= 4k^2\pi^3 \int_0^L d\eta \mathcal{F}^{-1}\left\{\Phi(2\pi\rho, \eta) \sin(2\alpha\eta)\right\},
\end{aligned} \tag{3.10}$$

where $\kappa = 2\pi\rho$ and $d\kappa = 2\pi d\rho$ and now $\alpha = (4\pi^2 |\vec{\rho}|^2)/(2k)$. As before, applying the Fourier transform to the cross correlation function above yields the following equation for the cross psd:

$$\begin{aligned}
\Phi_{ap}(\rho) &= \mathcal{F}\{\Gamma_{ap}(d)\} \\
&= \mathcal{F}\left\{4k^2\pi^3 \int_0^L d\eta \mathcal{F}^{-1}\left\{\Phi(2\pi\rho, \eta) \sin(2\alpha\eta)\right\}\right\} \\
&= 4k^2\pi^3 \int_0^L d\eta \Phi(2\pi\rho, \eta) \sin(2\alpha\eta).
\end{aligned} \tag{3.11}$$

In all of the psds derived above the 3-D psd for the refractive index perturbations is

$$\Phi(\kappa, \eta) = 0.033C_n^2(\eta)\Phi_0(\vec{\kappa}), \tag{3.12}$$

where

$$\Phi_0(\vec{\kappa}) = \frac{e^{(-\frac{\kappa^2 L^2 m}{4\pi^2})}}{(\kappa^2 + \frac{4\pi^2}{L_o^2})^{11/6}}. \tag{3.13}$$

Letting $\kappa = 2\pi\rho$ in the above equation and approximating the exponential to one, yields the following relationship

$$\Phi_0(\rho) = \frac{(2\pi)^{-11/3}}{(\rho^2 + \frac{1}{L_o^2})^{11/6}}. \quad (3.14)$$

We can use the relationship introduced in the previous section for constant $C_n^2(\eta)$ over the propagation path to represent the 3-D psd for the refractive index perturbations as

$$\Phi(\kappa, \eta) = 0.033 \frac{\lambda^2}{L} \left(\frac{0.185}{r_o} \right)^{5/3} \Phi_0(\tilde{\kappa}). \quad (3.15)$$

Therefore, the amplitude, phase, and cross power spectral densities become

$$\begin{aligned} \Phi_{aa}(\rho) &= 8k^2\pi^3 \int_0^L d\eta \Phi(2\pi\rho, \eta) \sin^2(\alpha\eta) \\ &= 8k^2\pi^3(0.033)\Phi_0(\rho) \int_0^L d\eta C_n^2(\eta) \sin^2(\alpha\eta) \\ &= 8k^2\pi^3(0.033) \left[\frac{\lambda^2}{L} \left(\frac{0.185}{r_o} \right)^{5/3} \right] \Phi_0(\rho) \left[\frac{L}{2} - \frac{1}{4} \left(\frac{1}{\alpha} \right) \sin(2\alpha L) \right] \\ &= 16\pi^5(0.033) \left(\frac{0.185}{r_o} \right)^{5/3} \Phi_0(\rho) \left[1 - \left(\frac{1}{2\pi\rho^2\lambda L} \right) \sin(2\pi\rho^2\lambda L) \right], \end{aligned} \quad (3.16)$$

and

$$\begin{aligned} \Phi_{pp}(\rho) &= 8k^2\pi^3 \int_0^L d\eta \Phi(2\pi\rho, \eta) \cos^2(\alpha\eta) \\ &= 8k^2\pi^3(0.033)\Phi_0(\rho) \int_0^L d\eta C_n^2(\eta) \cos^2(\alpha\eta) \\ &= 8k^2\pi^3(0.033) \left[\frac{\lambda^2}{L} \left(\frac{0.185}{r_o} \right)^{5/3} \right] \Phi_0(\rho) \left[\frac{L}{2} + \frac{1}{4} \left(\frac{1}{\alpha} \right) \sin(2\alpha L) \right] \\ &= 16\pi^5(0.033) \left(\frac{0.185}{r_o} \right)^{5/3} \Phi_0(\rho) \left[1 + \left(\frac{1}{2\pi\rho^2\lambda L} \right) \sin(2\pi\rho^2\lambda L) \right], \end{aligned} \quad (3.17)$$

and

$$\begin{aligned} \Phi_{ap}(\rho) &= 4k^2\pi^3 \int_0^L d\eta \Phi(2\pi\rho, \eta) \sin(2\alpha\eta) \\ &= 4k^2\pi^3(0.033)\Phi_0(\rho) \int_0^L d\eta C_n^2(\eta) \sin(2\alpha\eta) \end{aligned}$$

$$\begin{aligned}
&= 4k^2\pi^3(.033) \left[\frac{\lambda^2}{L} \left(\frac{0.185}{r_o} \right)^{5/3} \right] \Phi_0(\rho) \left[\frac{1}{2\alpha} (1 - \cos(2\alpha L)) \right] \\
&= 16\pi^5(0.033) \left(\frac{0.185}{r_o} \right)^{5/3} \Phi_0(\rho) \left[\frac{1}{\pi\rho^2\lambda L} \sin^2(\pi\rho^2\lambda L) \right], \tag{3.18}
\end{aligned}$$

where $\alpha = (4\pi^2 |\vec{\rho}|^2)/(2k)$ and $\Phi_0(\rho) = \frac{(2\pi)^{-11/3}}{(\rho^2 + \frac{1}{L_o^2})^{11/6}}$.

To present the psds more clearly a change of variables is performed. This change of variables allows the psds to be plotted versus the dimensionless quantity, $\rho' = \rho L_o$. The $\Phi_0(\rho')$ can be represented as the following

$$\Phi_0(\rho') = \frac{(2\pi)^{-11/3}}{(\frac{\rho'^2}{L_o^2} + \frac{1}{L_o^2})^{11/6}}, \tag{3.19}$$

but we find it convenient to represent it as follows

$$\Phi_0(\rho') = \frac{(2\pi)^{-11/3} L_o^2 L_o^{5/3}}{(\rho'^2 + 1)^{11/6}}. \tag{3.20}$$

Performing the change in variables results in the following relations for the amplitude, phase, and cross psds

$$\begin{aligned}
\Phi_{aa}(\rho') &= 16\pi^5(0.033)(0.185)^{5/3} \left(\frac{L_o}{r_o} \right)^{5/3} \frac{(2\pi)^{-11/3}}{(\rho'^2 + 1)^{11/6}} \\
&\times \left[1 - \left(\frac{L_o^2}{2\pi\rho'^2\lambda L} \right) \sin \left(\frac{2\pi\rho'^2\lambda L}{L_o^2} \right) \right], \tag{3.21}
\end{aligned}$$

and

$$\begin{aligned}
\Phi_{pp}(\rho') &= 16\pi^5(0.033)(0.185)^{5/3} \left(\frac{L_o}{r_o} \right)^{5/3} \frac{(2\pi)^{-11/3}}{(\rho'^2 + 1)^{11/6}} \\
&\times \left[1 + \left(\frac{L_o^2}{2\pi\rho'^2\lambda L} \right) \sin \left(\frac{2\pi\rho'^2\lambda L}{L_o^2} \right) \right], \tag{3.22}
\end{aligned}$$

and

$$\begin{aligned}
\Phi_{ap}(\rho') &= 16\pi^5(0.033)(0.185)^{5/3} \left(\frac{L_o}{r_o} \right)^{5/3} \frac{(2\pi)^{-11/3}}{(\rho'^2 + 1)^{11/6}} \\
&\times \left[\frac{L_o^2}{\pi\rho'^2\lambda L} \sin^2 \left(\frac{\pi\rho'^2\lambda L}{L_o^2} \right) \right]. \tag{3.23}
\end{aligned}$$

Figure 3.1 shows the power spectral densities as a function of ρL_o . Notice how the phase is much stronger than the amplitude for smaller spatial frequencies, but as ρL_o increases the phase and amplitude contributions converge to the same relationship. Also, notice how much quicker the phase psd and even the cross psd drops off as a function of frequency than the amplitude psd. The wider psd of the amplitude perturbations corresponds to higher spatial frequency content than the phase perturbations.

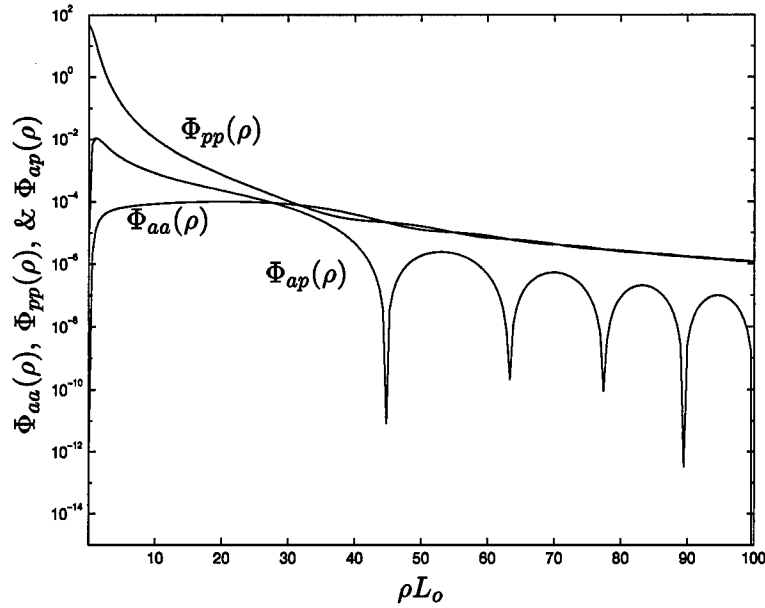


Figure 3.1 The power spectral densities as a function of ρL_o for $\lambda/L_o = 5 \times 10^{-8}$, $L/L_o = 10000$, and $L_o/r_o = 100$.

IV. *Fourier Series Based Atmospheric Phase and Amplitude Field Screen Generator*

Simulations are often used to study the effects of atmospheric turbulence on imaging systems and laser propagation. In this chapter we use the power spectral densities calculated in the previous chapter to develop phase and amplitude screens. Many screens only account for phase by performing a geometric optics phase calculation [2, 4, 11, 12, 15] which is appropriate when there is little far-field turbulence. When, however, the turbulence is extended through the entire medium the field encounters phase *and amplitude* variation due to diffraction effects. Using the proper ensemble statistics of the amplitude, phase, and cross power spectral densities (psds) will allow for realistic simulations of extended turbulence. These screens will simulate wavefront phase and amplitude perturbations in the optical field induced by propagation through the turbulence.

Many methods have been developed to generate phase screens. The methods can be broken into two mathematical approaches. The first approach uses a 2-Dimensional rectangular grid of points to represent the statistics of the screen, sample based screen representation. Whereas, in the second approach the screen is represented as a sum of orthogonal basis functions or a modal based representation. The most common method uses an approach based upon the Fourier transform. The technique is direct and computationally efficient due to the use of the Fast Fourier Transform (FFT). The problem with this method is that the energy of low spatial frequencies (e.g., tilt) is under-represented. The low spatial frequencies contain a large majority of the power which presents a major problem when studying the effects of tilt. A modal based approach allows for much better low frequency representation [15].

The method used in this thesis follows Welsh's paper on Fourier series based phase screen generation [15]. A modal representation is used to perform a Fourier Series (FS) expansion of the wavefront phase and amplitude over a square area. This approach has a much more accurate representation for low spatial frequencies than the sample based approach [15]. Welsh's relationship for the phase screen generation is extended by using the phase, *amplitude*, and *cross* psds developed in the previous chapter.

4.1 The Development of the Random Screen

To begin, the complex phase in the pupil at the point \vec{x} can be expressed as an integral of the contributions of each layer along the path as in Eq. (2.11):

$$\underline{P_p}(\vec{x}) = \int \int_0^L d\eta d\vec{\kappa} \tilde{A}(\eta, \vec{\kappa}) e^{-j(\vec{\kappa} \cdot \vec{x})} \cos(\eta\alpha). \quad (4.1)$$

Similarly, the complex amplitude perturbations in the pupil can be represented by the following as in Eq. (2.10):

$$\underline{P_a}(\vec{x}) = \int \int_0^L d\eta d\vec{\kappa} \tilde{A}(\eta, \vec{\kappa}) e^{-j(\vec{\kappa} \cdot \vec{x})} \sin(\eta\alpha). \quad (4.2)$$

The amplitude, phase, and cross correlations were developed in Chapter 2 by computing the following

$$\Gamma_{aa}(\vec{d}) = \langle P_a(\vec{x}) P_a(\vec{x} - \vec{d}) \rangle, \quad (4.3)$$

and

$$\Gamma_{pp}(\vec{d}) = \langle P_p(\vec{x}) P_p(\vec{x} - \vec{d}) \rangle, \quad (4.4)$$

and

$$\Gamma_{ap}(\vec{d}) = \langle P_a(\vec{x}) P_p(\vec{x} - \vec{d}) \rangle. \quad (4.5)$$

where the angle brackets denote the expected value of the argument. The psds were calculated by taking the Fourier transforms of the correlation functions.

The next step will be to generate random wavefront screens of amplitude and phase with the proper statistics. The screen can be broken into a phase screen, $\hat{\phi}(\vec{x})$, and an amplitude screen, $\hat{A}(\vec{x})$. The two can be combined into a phase and amplitude field screen

$$\hat{E}(\vec{x}) = (1 + \hat{A}(\vec{x})) e^{j\hat{\phi}(\vec{x})}. \quad (4.6)$$

The area over which the optical field perturbations are being represented by the FS is a square of dimension D_p . The FS representation of the phase and amplitude will be periodic in both the x and y -directions with period D_p . The FS expansion of the phase can be represented as:

$$\hat{\phi}(\vec{x}) = \sum_{n=-\infty}^{\infty} \sum_{n'=-\infty}^{\infty} c_{n,n'}^{\phi} \exp \left\{ j2\pi \left(\frac{nx}{D_p} + \frac{n'y}{D_p} \right) \right\}, \quad (4.7)$$

where $c_{n,n'}^\phi$ is the FS coefficient for the spatial frequency $\vec{f} = \frac{\hat{x}n}{D_p} + \frac{\hat{y}n'}{D_p}$. The vectors \hat{x} and \hat{y} are unit vectors in the x and y -directions, respectively, and x and y are the x and y components of \vec{x} . The coefficients $c_{n,n'}^\phi$ are chosen to be circular-complex Gaussian, independent random variables having a mean square value given by

$$E \left\{ |c_{n,n'}^\phi|^2 \right\} = \frac{1}{D_p^2} \Phi_{\phi\phi} \left(\frac{n}{D_p}, \frac{n'}{D_p} \right) \quad (4.8)$$

where $E\{\cdot\}$ denotes the expected value of the argument and $\Phi_{\phi\phi}$ represents the phase psd. We require Hermitian symmetry, $c_{n,n'} = c_{-n,-n'}^*$. We also require the zero frequency term to be a real, zero mean Gaussian random variable [15]. In Welsh's paper he used the geometric phase psd in the above equation, but one could just as easily use the psds developed for the phase *and the amplitude* perturbations. The FS expansion of the amplitude can be represented in the same way by the following:

$$\hat{A}(\vec{x}) = \sum_{n=-\infty}^{\infty} \sum_{n'=-\infty}^{\infty} c_{n,n'}^A \exp \left\{ j2\pi \left(\frac{nx}{D_p} + \frac{n'y}{D_p} \right) \right\}, \quad (4.9)$$

where $c_{n,n'}^A$ is the FS coefficient for the spatial frequency $\vec{f} = \frac{\hat{x}n}{D_p} + \frac{\hat{y}n'}{D_p}$. Similarly, the coefficients $c_{n,n'}^A$ are also chosen to be circular-complex Gaussian, independent random variables having a mean square value given by

$$E \left\{ |c_{n,n'}^A|^2 \right\} = \frac{1}{D_p^2} \Phi_{AA} \left(\frac{n}{D_p}, \frac{n'}{D_p} \right) \quad (4.10)$$

and due to Hermitian symmetry, $c_{n,n'} = c_{-n,-n'}^*$. The zero frequency term was also required to be a real, zero mean Gaussian random variable [15].

We could simply use the amplitude and phase psds to calculate independent amplitude and phase effects, but since they are not independent we need to also take into account their cross correlation. Therefore, we need to satisfy the following conditions:

$$E \left\{ |c_{n,n'}^\phi|^2 \right\} = \frac{1}{D_p^2} \Phi_{\phi\phi} \left(\frac{n}{D_p}, \frac{n'}{D_p} \right), \quad (4.11)$$

and

$$E \left\{ |c_{n,n'}^A|^2 \right\} = \frac{1}{D_p^2} \Phi_{AA} \left(\frac{n}{D_p}, \frac{n'}{D_p} \right), \quad (4.12)$$

and

$$E \left\{ c_{n,n'}^A c_{n,n'}^\phi \right\} = \frac{1}{D_p^2} \Phi_{A\phi} \left(\frac{n}{D_p}, \frac{n'}{D_p} \right). \quad (4.13)$$

To achieve these conditions we must satisfy all the elements in the correlation matrix, $R_{c_{n,n'}}$, for the amplitude, phase, and cross correlations. The correlation matrix is defined as

$$\begin{aligned}
 R_{c_{n,n'}} &= E \left[\begin{bmatrix} c_{n,n'}^\phi \\ c_{n,n'}^A \end{bmatrix} [c_{n,n'}^\phi, c_{n,n'}^A]^* \right] \\
 &= \begin{bmatrix} E[|c_{n,n'}^\phi|^2] & E[c_{n,n'}^A c_{n,n'}^{\phi*}] \\ E[c_{n,n'}^{A*} c_{n,n'}^\phi] & E[|c_{n,n'}^A|^2] \end{bmatrix} \\
 &= \frac{1}{D_p^2} \begin{bmatrix} \Phi_{\phi\phi} \left(\frac{n}{D_p}, \frac{n'}{D_p} \right) & \Phi_{A\phi} \left(\frac{n}{D_p}, \frac{n'}{D_p} \right) \\ \Phi_{A\phi} \left(\frac{n}{D_p}, \frac{n'}{D_p} \right) & \Phi_{AA} \left(\frac{n}{D_p}, \frac{n'}{D_p} \right) \end{bmatrix} \quad (4.14)
 \end{aligned}$$

To satisfy Eqs. (4.11), (4.12), and (4.13) consider

$$\begin{bmatrix} c_{n,n'}^\phi \\ c_{n,n'}^A \end{bmatrix} = C^T \begin{bmatrix} g_1 \\ g_2 \end{bmatrix}, \quad (4.15)$$

where C^T is a 2×2 matrix and g_1 and g_2 are complex zero mean unit variance independent Gaussian random numbers. To form the C^T matrix we need to decompose the correlation matrix, $R_{c_{n,n'}}$, so that the phase, amplitude and cross correlation are all satisfied. The Cholesky decomposition is performed for this transformation, since $R_{c_{n,n'}}$ is positive definite:

$$R_{c_{n,n'}} = C^T C. \quad (4.16)$$

Performing the decomposition results in the following matrix

$$C^T = \frac{1}{D_p} \begin{bmatrix} \sqrt{\Phi_{\phi\phi}} & 0 \\ \frac{\Phi_{A\phi}}{\sqrt{\Phi_{\phi\phi}}} & \sqrt{\Phi_{AA} - \frac{\Phi_{A\phi}^2}{\Phi_{\phi\phi}}} \end{bmatrix}. \quad (4.17)$$

Notice what happens when $R_{c_{n,n'}}$ is computed:

$$R_{c_{n,n'}} = E \left[C^T \begin{bmatrix} g_1 \\ g_2 \end{bmatrix} [g_1 \ g_2]^* C \right]$$

$$\begin{aligned}
&= C^T E \begin{bmatrix} \begin{bmatrix} g_1 \\ g_2 \end{bmatrix} [g_1 \ g_2]^* \end{bmatrix} C \\
&= C^T \begin{bmatrix} 1 & 0 \\ 0 & 1 \end{bmatrix} C \\
&= C^T C = R_{c_{n,n'}}.
\end{aligned} \tag{4.18}$$

Therefore, we can determine what random numbers to use for the screen by using Eq. (4.15) and Eq. (4.17):

$$\begin{bmatrix} c_{n,n'}^\phi \\ c_{n,n'}^A \end{bmatrix} = \frac{1}{D_p} \begin{bmatrix} g_1 \sqrt{\Phi_{\phi\phi}} \\ g_1 \frac{\Phi_{A\phi}}{\sqrt{\Phi_{\phi\phi}}} + g_2 \sqrt{\Phi_{AA} - \frac{\Phi_{A\phi}^2}{\Phi_{\phi\phi}}} \end{bmatrix}. \tag{4.19}$$

Notice how $c_{n,n'}^A$ approaches $g_2 \sqrt{\Phi_{AA}}$ when the cross correlation approaches zero which is the desired result. Also, the phase term is not affected by the cross correlation.

Welsh approximates the phase by truncating the FS expansion in Eq. (4.7) to a finite number of terms. The truncated expansion becomes [15]

$$\begin{aligned}
\hat{\phi}(\vec{x}) &= \sum_{n=-(N-1)}^{N-1} \sum_{n'=-(N-1)}^{N-1} c_{n,n'}^\phi \exp \left\{ j2\pi \left(\frac{nx}{D_p} + \frac{ny'}{D_p} \right) \right\} \\
&= 2\text{Re} \left[\sum_{n=0}^{N-1} \sum_{n'=0}^{N-1} c_{n,n'}^\phi \exp \left\{ j2\pi \left(\frac{nx}{D_p} + \frac{ny'}{D_p} \right) \right\} \right. \\
&\quad \left. + \sum_{n=1}^{N-1} \sum_{n'=-(N-1)}^{-1} c_{n,n'}^\phi \exp \left\{ j2\pi \left(\frac{nx}{D_p} + \frac{ny'}{D_p} \right) \right\} \right].
\end{aligned} \tag{4.20}$$

This relationship is also valid for the amplitude, $\hat{A}(\vec{x})$, by replacing $c_{n,n'}^\phi$ with $c_{n,n'}^A$.

4.2 Method for Screen Generation

Equation (4.20) can be expressed in matrix algebra notation, allowing for simple implementation on mathematical software packages. In order to represent the equation in matrix algebra form, the phase screen is evaluated on a $M \times M$ square grid of dimension D , where D could be considered the diameter of the optical system pupil. In most instances

D_p will be much larger than D . The matrix formulation uses the following vectors in the representation of the phase and amplitude;

\mathbf{x} : column vector of length M (x-coordinates for the grid points),

\mathbf{y} : column vector of length M (y-coordinates for the grid points),

\mathbf{f} : column vector of length N (spatial frequency with n th entry being $[n - 1]/D_p$),

$\mathbf{1}$: column vector of ones of length M [15].

Since the atmospheric turbulence is extended over the entire propagation path at constant strength of turbulence, the amplitude and phase screens can be combined and collapsed into one screen at the pupil. The phase and amplitude can be represented as [15]

$$\begin{aligned} \hat{\phi}(\mathbf{x}\mathbf{1}^T\hat{x} + \mathbf{1}\mathbf{y}^T\hat{y}) &= 2\text{Re} \left\{ [\exp\{j2\pi\mathbf{f}\mathbf{x}^T\}] \right. \\ &\quad \times \left. \left(C_L^\phi[\exp j2\pi\mathbf{f}\mathbf{y}^T] + C_R^\phi[\exp -j2\pi\mathbf{f}\mathbf{y}^T] \right) \right\}, \end{aligned} \quad (4.21)$$

and

$$\begin{aligned} \hat{A}(\mathbf{x}\mathbf{1}^T\hat{x} + \mathbf{1}\mathbf{y}^T\hat{y}) &= 2\text{Re} \left\{ [\exp\{j2\pi\mathbf{f}\mathbf{x}^T\}] \right. \\ &\quad \times \left. \left(C_L^A[\exp j2\pi\mathbf{f}\mathbf{y}^T] + C_R^A[\exp -j2\pi\mathbf{f}\mathbf{y}^T] \right) \right\}, \end{aligned} \quad (4.22)$$

where C_L^ϕ and C_R^ϕ are $N \times N$ matrices containing the complex random variables $c_{n,n'}^\phi$ and C_L^A and C_R^A are $N \times N$ matrices containing the complex random variables $c_{n,n'}^A$.

4.3 Field Screen Generation Procedure

The psds developed in Chapter 3 for weak turbulence will be utilized to generate the random wavefront phase from Eq. (4.21) and the random amplitude perturbation from Eq. (4.22). The following considerations and steps are required to represent the phase and amplitude effectively.

4.3.1 Set-up:

1. FS period, D_p^ϕ , D_p^A , D_p^C , must be larger than the non-negligible support of Γ_{pp} , Γ_{aa} , and Γ_{ap} , respectively. If D_p is not selected large enough, the periodic effects of D_p could occur in the structure function for the large screen case.
2. N must be chosen so that the power encompassed in the simulated field sufficiently represents the power in the random processes $\phi(\vec{x})$ and $A(\vec{x})$. This can be determined by considering the ratio of the power in $\hat{\phi}(\vec{x})$ to the power in $\phi(\vec{x})$ and the ratio of $\hat{A}(\vec{x})$ to the power in $A(\vec{x})$. The power ratios are given by

$$\frac{E[|\hat{\phi}(\vec{x})|^2]}{E[|\phi(\vec{x})|^2]} = \frac{\int_{-N/D_p^\phi}^{N/D_p^\phi} \int_{-N/D_p^\phi}^{N/D_p^\phi} d\vec{\rho} \Phi_{\phi\phi}(\vec{\rho})}{\int_{-\infty}^{\infty} \int_{-\infty}^{\infty} d\vec{\rho} \Phi_{\phi\phi}(\vec{\rho})} \quad (4.23)$$

for the phase,

$$\frac{E[|\hat{A}(\vec{x})|^2]}{E[|A(\vec{x})|^2]} = \frac{\int_{-N/D_p^A}^{N/D_p^A} \int_{-N/D_p^A}^{N/D_p^A} d\vec{\rho} \Phi_{AA}(\vec{\rho})}{\int_{-\infty}^{\infty} \int_{-\infty}^{\infty} d\vec{\rho} \Phi_{AA}(\vec{\rho})} \quad (4.24)$$

for the amplitude, and

$$\frac{E[\hat{A}(\vec{x})\hat{\phi}(\vec{x})]}{E[A(\vec{x})\phi(\vec{x})]} = \frac{\int_{-N/D_p^C}^{N/D_p^C} \int_{-N/D_p^C}^{N/D_p^C} d\vec{\rho} \Phi_{A\phi}(\vec{\rho})}{\int_{-\infty}^{\infty} \int_{-\infty}^{\infty} d\vec{\rho} \Phi_{A\phi}(\vec{\rho})} \quad (4.25)$$

for the cross term. The value of N/D_p is chosen to accurately represent the wave-front's phase, amplitude, and cross statistics.

3. For correlated phase and amplitude screens D_p as well as N must be the same for the amplitude, phase, and cross statistics (i.e., $D_p = D_p^\phi = D_p^A = D_p^C$) to properly represent the cross statistics.
4. M must be chosen to be large enough to sufficiently sample the perturbations in the aperture of dimension, D .

4.3.2 Screen Generation:

1. The correlated phase and amplitude screens will be calculated by filling the matrices C_L^ϕ , C_R^ϕ , C_L^A , and C_R^A with circularly complex Gaussian random variables where $[g_1]_{i,i'}$, $[g_2]_{i,i'}$, $[g_3]_{i,i'}$, and $[g_4]_{i,i'}$ are complex zero mean unit variance independent

Gaussian random numbers. The i, i' th elements of the matrices will contain the following:

$$[C_L^\phi]_{i,i'} = \frac{1}{D_p} \sqrt{\Phi_{\phi\phi} \left(\frac{i-1}{D_p}, \frac{i'-1}{D_p} \right)} [g_1]_{i,i'} \quad (4.26)$$

$$[C_R^\phi]_{i,i'} = \frac{1}{D_p} \sqrt{\Phi_{\phi\phi} \left(\frac{i-1}{D_p}, \frac{1-i'}{D_p} \right)} [g_2]_{i,i'} \quad (4.27)$$

$$\begin{aligned} [C_L^A]_{i,i'} = & \frac{1}{D_p} \left[[g_1]_{i,i'} \frac{\Phi_{A\phi} \left(\frac{i-1}{D_p}, \frac{i'-1}{D_p} \right)}{\sqrt{\Phi_{\phi\phi} \left(\frac{i-1}{D_p}, \frac{i'-1}{D_p} \right)}} \right. \\ & \left. + [g_3]_{i,i'} \sqrt{\Phi_{AA} \left(\frac{i-1}{D_p}, \frac{i'-1}{D_p} \right) - \frac{\Phi_{A\phi}^2 \left(\frac{i-1}{D_p}, \frac{i'-1}{D_p} \right)}{\Phi_{\phi\phi} \left(\frac{i-1}{D_p}, \frac{i'-1}{D_p} \right)}} \right] \end{aligned} \quad (4.28)$$

$$\begin{aligned} [C_R^A]_{i,i'} = & \frac{1}{D_p} \left[[g_2]_{i,i'} \frac{\Phi_{A\phi} \left(\frac{i-1}{D_p}, \frac{1-i'}{D_p} \right)}{\sqrt{\Phi_{\phi\phi} \left(\frac{i-1}{D_p}, \frac{1-i'}{D_p} \right)}} \right. \\ & \left. + [g_4]_{i,i'} \sqrt{\Phi_{AA} \left(\frac{i-1}{D_p}, \frac{1-i'}{D_p} \right) - \frac{\Phi_{A\phi}^2 \left(\frac{i-1}{D_p}, \frac{1-i'}{D_p} \right)}{\Phi_{\phi\phi} \left(\frac{i-1}{D_p}, \frac{1-i'}{D_p} \right)}} \right], \end{aligned} \quad (4.29)$$

where the multiplicative terms represent the standard deviation of the random numbers, $[g_1]_{i,i'}$, $[g_2]_{i,i'}$, $[g_3]_{i,i'}$, and $[g_4]_{i,i'}$.

2. Replace the complex random values of the first row and column of C_R^ϕ and C_R^A with zeros.
3. Compute the random screen, $\hat{E}(\vec{x})$, by evaluating Eq. (4.21) for the phase and Eq. (4.22) for the amplitude with the resulting screen having the following form:

$$\hat{E}(\vec{x}) = (1 + \hat{A}(\vec{x})) e^{j\hat{\phi}(\vec{x})}. \quad (4.30)$$

4. For subsequent independent screen realizations go to step 1 under subsection 4.3.2 and repeat steps 1 through 3.

4.4 Numerical Results

In this section the specific psds calculated in Chapter 3 and Eqs. (4.21) and (4.22) will be used to generate phase and amplitude screen realizations. These psds are valid for a plane wave using a constant strength of turbulence profile. Monte Carlo experiments for a variety of conditions are performed to show that Eqs. (4.21) and (4.22) generate screens with the correct spatial statistics.

4.4.1 Weak Turbulence Atmospheric Statistics. Since multiples of the frequency $1/D_p$ are used in the FS expansion it is convenient to include D_p in the psds. Therefore from Eqs. (3.16), (3.17), and (3.18) developed in the previous chapter the psds become

$$\begin{aligned}\Phi_{AA}(\rho) &= 16\pi^5(0.033)(0.185)^{5/3} \frac{\left(\frac{D_p}{r_o}\right)^{5/3} D_p^2 (2\pi)^{-11/3}}{\left(\rho^2 D_p^2 + \left(\frac{D_p}{L_o}\right)^2\right)^{11/6}} \\ &\quad \times \left[1 - \left(\frac{1}{2\pi\rho^2\lambda L}\right) \sin(2\pi\rho^2\lambda L)\right] \\ &= 0.01149 \frac{\left(\frac{D_p}{r_o}\right)^{5/3} D_p^2}{\left(\rho^2 D_p^2 + \left(\frac{D_p}{L_o}\right)^2\right)^{11/6}} \left[1 - \left(\frac{1}{2\pi\rho^2\lambda L}\right) \sin(2\pi\rho^2\lambda L)\right], \quad (4.31)\end{aligned}$$

and

$$\begin{aligned}\Phi_{\phi\phi}(\rho) &= 16\pi^5(0.033)(0.185)^{5/3} \frac{\left(\frac{D_p}{r_o}\right)^{5/3} D_p^2 (2\pi)^{-11/3}}{\left(\rho^2 D_p^2 + \left(\frac{D_p}{L_o}\right)^2\right)^{11/6}} \\ &\quad \times \left[1 + \left(\frac{1}{2\pi\rho^2\lambda L}\right) \sin(2\pi\rho^2\lambda L)\right] \\ &= 0.01149 \frac{\left(\frac{D_p}{r_o}\right)^{5/3} D_p^2}{\left(\rho^2 D_p^2 + \left(\frac{D_p}{L_o}\right)^2\right)^{11/6}} \left[1 + \left(\frac{1}{2\pi\rho^2\lambda L}\right) \sin(2\pi\rho^2\lambda L)\right], \quad (4.32)\end{aligned}$$

and

$$\begin{aligned}
\Phi_{A\phi}(\rho) &= 16\pi^5(0.033)(0.185)^{5/3} \frac{\left(\frac{D_p}{r_o}\right)^{5/3} D_p^2 (2\pi)^{-11/3}}{\left(\rho^2 D_p^2 + \left(\frac{D_p}{L_o}\right)^2\right)^{11/6}} \left[\frac{1}{\pi \rho^2 \lambda L} \sin^2(\pi \rho^2 \lambda L) \right] \\
&= 0.01149 \frac{\left(\frac{D_p}{r_o}\right)^{5/3} D_p^2}{\left(\rho^2 D_p^2 + \left(\frac{D_p}{L_o}\right)^2\right)^{11/6}} \left[\frac{1}{\pi \rho^2 \lambda L} \sin^2(\pi \rho^2 \lambda L) \right]. \quad (4.33)
\end{aligned}$$

4.4.2 Setup for independent **uncorrelated** phase and amplitude screen generation:

Steps 1 and 2. From steps 1 and 2 outlined in subsection 4.3.1 the FS period, D_p , and the number of FS coefficients N must be selected for the phase and amplitude. For uncorrelated screen generation the cross psd, $\Phi_{A\phi}$, in Eqs. (4.28) and (4.29) will be set to zero. Since the amplitude and phase will be uncorrelated, N and D_p can be selected separately to best represent the phase and amplitude perturbations. From Fig. 2.3 it appears that a value of $D_p^\phi \geq 4L_o$ will be adequate for the phase. For numerical results shown here we set $D_p^\phi = 4L_o$. Using Eq. (4.23) we determine that $N \geq 15D_p^\phi/L_o$ is required to capture 99% of the power in the phase. Since we chose $D_p^\phi = 4L_o$ at least $N = 60$ FS coefficients are required.

Considering the amplitude, from Fig. 2.2 it appears that a value of $D_p^A \geq L_o/4$ will be adequate for the amplitude. For numerical results shown here we set $D_p^A = L_o/4$. Using Eq. (4.24) we determine that $N \geq 720D_p^A/L_o$ is required to capture 99% of the power in the amplitude. Since we chose $D_p^A = L_o/4$ at least $N = 180$ FS coefficients are required.

We also need to consider sample spacing of the screens. In these numerical results we chose $N = \frac{3}{4}D_p^\phi/r_o$ for the phase statistics. In the following results we chose a strength of turbulence, $L_o/r_o = 100$ which for the phase implies that $N = (3/4)(D_p^\phi/L_o)(L_o/r_o) = \frac{3}{4} \cdot 4 \cdot 100 = 300$. This value of N will also satisfy the power requirements for the amplitude using the $D_p^A = L_o/4$.

4.4.3 Simulation results for independent **uncorrelated amplitude and phase screen generation.** Ten thousand random screens were generated in a Monte Carlo experiment

by following steps 1-4 of subsection 4.3.2. Each screen was generated on a square grid with a screen dimension of $D = 100r_o$ or $D = \frac{1}{4}D_p^\phi$ for the phase. The large screen case allowed us to compare the simulated spatial amplitude and phase psds to the theoretical psds. We chose an $M \times M$ grid for the screen of $2D/r_o \times 2D/r_o$. The ensemble based wavefront phase was computed to be 187.61 square radians, which compares with the theoretical mean square value (msv) of 186.57 square radians and the amplitude was computed to be 0.0877 which compares to the theoretical msv of 0.0879.

Next, a screen of dimension $D = 10r_o$ is considered. This time one thousand screens were generated for use in calculating the structure functions. An $M \times M$ grid for the field screen of $4D/r_o \times 4D/r_o$ was chosen. Figure 4.1 shows the phase structure function calculated for the ensemble of random screens along with the theoretical structure function computed from Eq. (2.38). Figure 4.2 shows the calculated amplitude structure function and the theoretical function computed from Eq. (2.37). The ensemble based and the theoretical structure functions match extremely well. Also, notice how the amplitude structure function away from the center of the screen approaches twice the mean square value of the amplitude perturbations calculated in the previous paragraph.

Figures 4.3 and 4.4 show the phase and amplitude structure functions results for a larger screen dimension of $D = 40r_o$. As before the ensemble based and the theoretical structure functions match extremely well.

Finally, the amplitude and phase structure functions are calculated for a very large screen dimension of $D = 100r_o$. For this case, D_p^A/L_o for the amplitude must be selected as $D_p^A/L_o \geq 5/8$ in order to keep the periodic nature of D_p^A from corrupting the structure function. The phase structure function is in Fig. 4.5 and matches very well with the theoretical function. If $N = 300$ is selected, the amplitude psd will be under-represented, since $N \geq 720D_p^A/L_o$ will no longer be satisfied. Therefore, if we let $N = 450$, over 99 % of the power in the amplitude psd will be captured. Figure 4.6 shows that the resulting amplitude structure function is slightly under represented but within 1% of the theoretical plot.

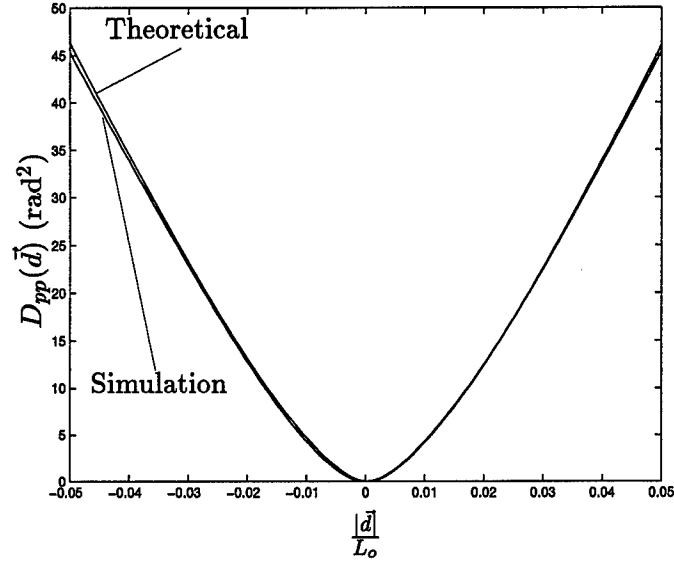


Figure 4.1 Theoretical and simulated phase structure function, $D_{pp}(\vec{d})$ plotted versus $|\vec{d}|/L_o$ for a von Karman turbulence power spectrum with $D_p^\phi/L_o = 4$, $D_p^\phi/r_o = 400$, $L/L_o = 1000$, and $\lambda/L_o = 5 \times 10^{-8}$. The screen dimension is $D = 10r_o$ and the number of FS coefficients is $N = 300$.

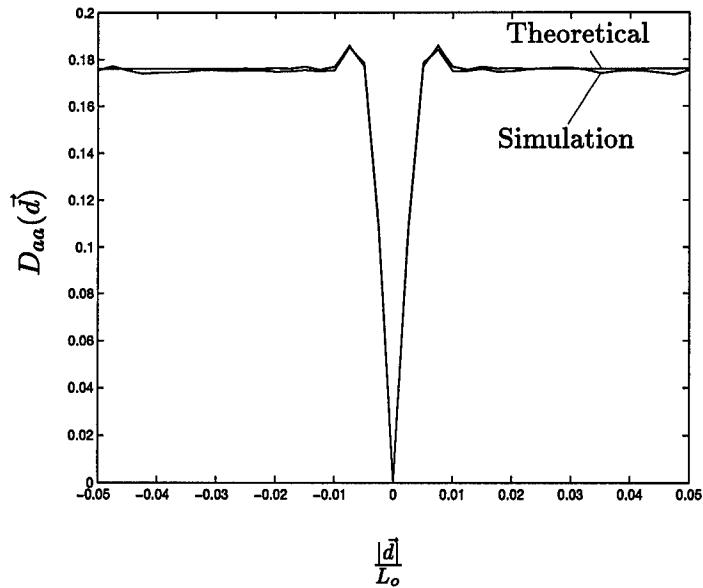


Figure 4.2 Theoretical and simulated amplitude structure function, $D_{aa}(\vec{d})$ plotted versus $|\vec{d}|/L_o$ for a von Karman turbulence power spectrum with $D_p^A/L_o = 1/4$, $D_p^A/r_o = 25$, $L/L_o = 1000$, and $\lambda/L_o = 5 \times 10^{-8}$. The screen dimension is $D = 10r_o$ and the number of FS coefficients is $N = 300$.

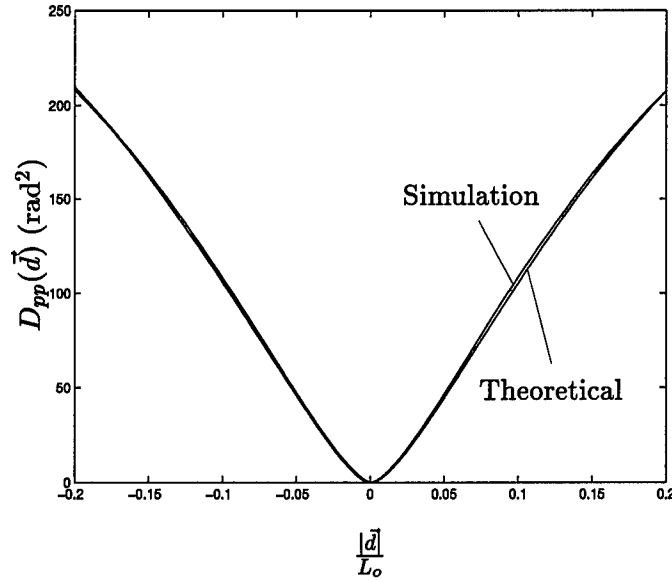


Figure 4.3 Theoretical and simulated phase structure function, $D_{pp}(\vec{d})$, plotted versus $|\vec{d}|/L_o$ for a von Karman turbulence power spectrum with $D_p^\phi/L_o = 4$, $D_p^\phi/r_o = 400$, $L/L_o = 1000$, and $\lambda/L_o = 5 \times 10^{-8}$. The screen dimension is $D = 40r_o$ and the number of FS coefficients is $N = 300$.

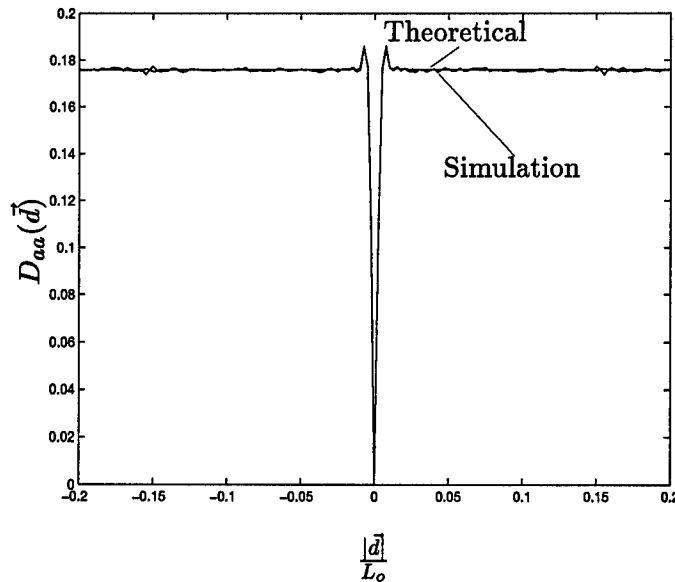


Figure 4.4 Theoretical and simulated amplitude structure function, $D_{aa}(\vec{d})$, plotted versus $|\vec{d}|/L_o$ for a von Karman turbulence power spectrum with $D_p^A/L_o = 1/4$, $D_p^A/r_o = 25$, $L/L_o = 1000$, and $\lambda/L_o = 5 \times 10^{-8}$. The screen dimension is $D = 40r_o$ and the number of FS coefficients is $N = 300$.

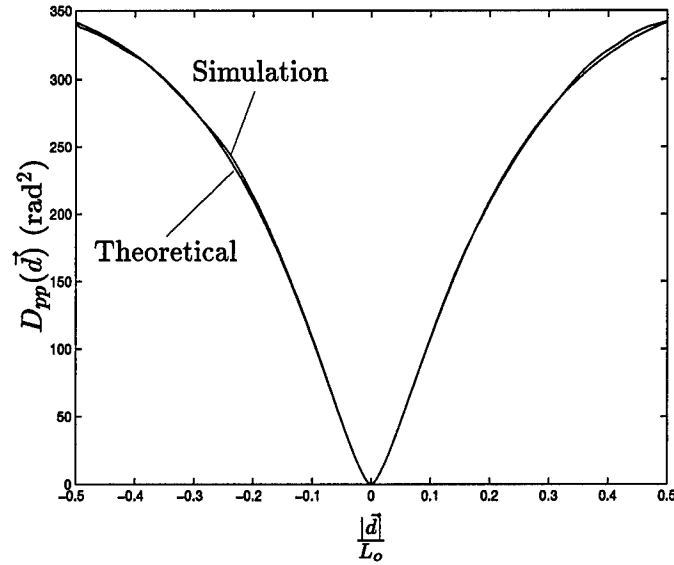


Figure 4.5 Theoretical and simulated phase structure function, $D_{pp}(\vec{d})$, plotted versus $|\vec{d}|/L_o$ for a von Karman turbulence power spectrum with $D_p^\phi/L_o = 4$, $D_p^\phi/r_o = 400$, $L/L_o = 1000$, and $\lambda/L_o = 5 \times 10^{-8}$. The screen dimension is $D = 100r_o$ and the number of FS coefficients is $N = 300$.

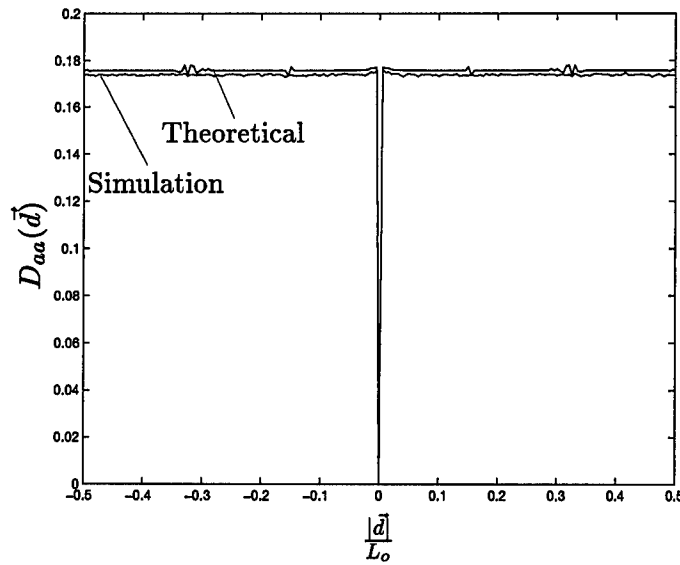


Figure 4.6 Theoretical and simulated amplitude structure function, $D_{aa}(\vec{d})$, plotted versus $|\vec{d}|/L_o$ for a von Karman turbulence power spectrum with $D_p^A/L_o = 5/8$, $D_p^A/r_o = 62.5$, $L/L_o = 1000$, and $\lambda/L_o = 5 \times 10^{-8}$. The screen dimension is $D = 100r_o$ and the number of FS coefficients is $N = 450$.

4.4.4 Setup for independent **correlated** phase and amplitude screen generation:

Steps 1, 2, and 3. From steps 1 and 2 outlined in subsection 4.3.1 the FS period, D_p , and the number of FS coefficients N must be selected for the phase, amplitude, and cross psds. Correlated phase and amplitude screen generation requires the same values for D_p and N . From subsection 4.4.2 it is apparent that the amplitude and phase requirements for D_p and N are not the same. First D_p must be selected, since it must be chosen large enough to represent the amplitude, phase, and cross statistics sufficiently. In considering the cross statistics, from Fig. 2.4 it appears that a value of $D_p \geq L_o$ will be adequate for the cross correlation. From Eq. (4.25) $N \geq 100D_p/L_o$ is determined to be required to capture 99% of the power in the cross statistics. In order to sufficiently represent the phase, amplitude, and cross statistics $D_p = 1.5$ is chosen. To capture 99% of the power in the amplitude, $N \geq 720D_p/L_o$ must be satisfied, requiring $N \geq 1080$. This requirement is much higher than the practical limits of the computation speed, especially given the number of iterations in the Monte Carlo experiments. $N = 400$ FS coefficients was chosen which resulted in a representation of over 99% in the phase and cross statistics and 92.3% for the amplitude.

4.4.5 Simulation results for independent **correlated** amplitude and phase screen generation.

Ten thousand random screens were generated in a Monte Carlo experiment by following steps 1-4 of subsection 4.3.2. Each screen was generated on a square grid with a screen dimension of $D = 100r_o$. The large screen case allowed us to compare the simulated spatial amplitude, phase, and cross psds to the theoretical psds. As before, we chose an $M \times M$ grid for the screen of $2D/r_o \times 2D/r_o$. Using $D_p = 1.5$ and $N = 400$ determined in the previous section the ensemble based phase, amplitude and cross values were determined. The ensemble based wavefront phase was computed to be 185.41 square radians, which compares with the theoretical mean square value (msv) of 186.57 square radians and the amplitude was computed to be 0.0812 which compares to the theoretical msv of 0.0879. The ensemble based mean cross value of the amplitude and phase perturbations was computed to be 0.2416 which compares with the theoretical value of 0.2418.

Next a screen of dimension $D = 10r_o$ is considered. Ten thousand screens are generated to calculate the structure functions. Again, an $M \times M$ grid for the field of $4D/r_o \times 4D/r_o$ is selected. Figure 4.7 shows the phase structure function calculated for the ensemble of random screens along with the theoretical structure function computed from Eq. (2.38). Figure 4.8 shows the calculated amplitude structure function and the theoretical function computed from Eq. (2.37). Figure 4.9 shows the calculated cross structure function and the theoretical function computed from Eq. (2.39). The ensemble based and the theoretical structure functions match extremely well for the phase and cross, but, as expected, the simulated amplitude structure function drops slightly below the theoretical plot.

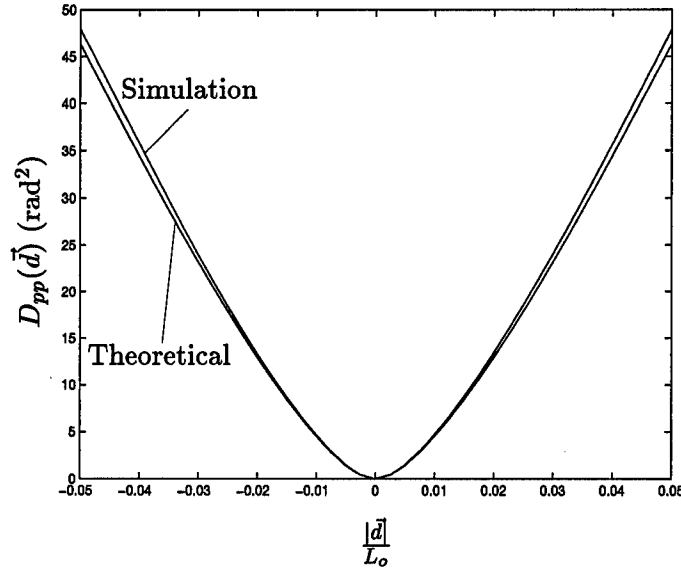


Figure 4.7 Theoretical and simulated phase structure function, $D_{pp}(\vec{d})$, plotted versus $|\vec{d}|/L_o$ for a von Karman turbulence power spectrum with $D_p/L_o = 1.5$, $D_p/r_o = 150$, $L/L_o = 1000$, and $\lambda/L_o = 5 \times 10^{-8}$. The screen dimension is $D = 10r_o$ and the number of FS coefficients is $N = 400$. The phase screens used in this calculation were correlated with the amplitude screens by the cross correlation.

Figures 4.10, 4.11, 4.12 show the phase, amplitude, and cross structure functions results for the very large screen dimension of $D = 100r_o$. As before, the ensemble based and the theoretical structure functions match extremely well for the phase and cross, but the ensemble based amplitude structure function drops slightly below the theoretical.

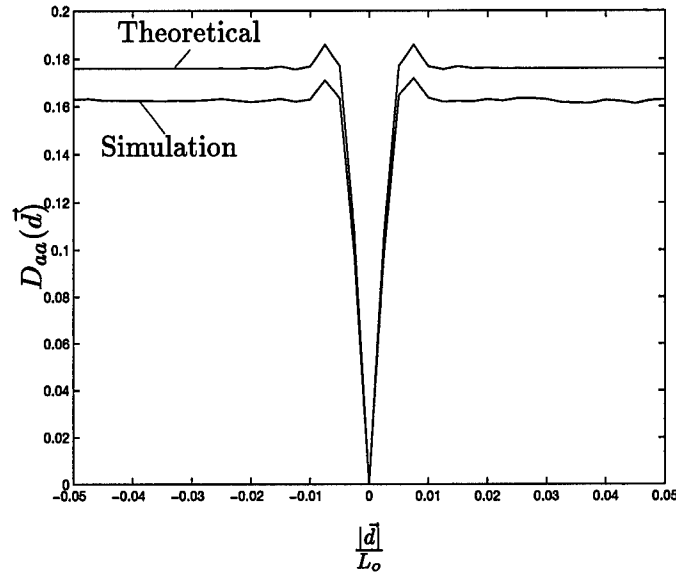


Figure 4.8 Theoretical and simulated amplitude structure function, $D_{aa}(\vec{d})$, plotted versus $|\vec{d}|/L_o$ for a von Karman turbulence power spectrum with $D_p/L_o = 1.5$, $D_p/r_o = 150$, $L/L_o = 1000$, and $\lambda/L_o = 5 \times 10^{-8}$. The screen dimension is $D = 10r_o$ and the number of FS coefficients is $N = 400$. The amplitude screens used in this calculation were correlated with the phase screens by the cross correlation.

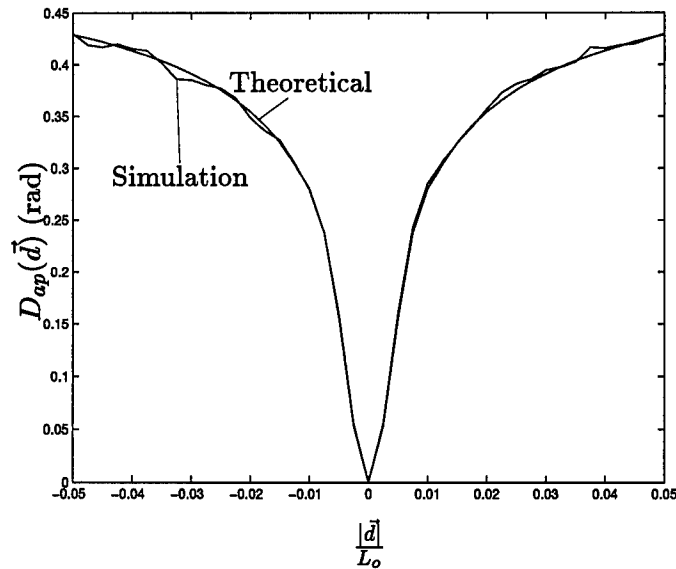


Figure 4.9 Theoretical and simulated cross structure function, $D_{ap}(\vec{d})$, plotted versus $|\vec{d}|/L_o$ for a von Karman turbulence power spectrum with $D_p/L_o = 1.5$, $D_p/r_o = 150$, $L/L_o = 1000$, and $\lambda/L_o = 5 \times 10^{-8}$. The screen dimension is $D = 10r_o$ and the number of FS coefficients is $N = 400$.

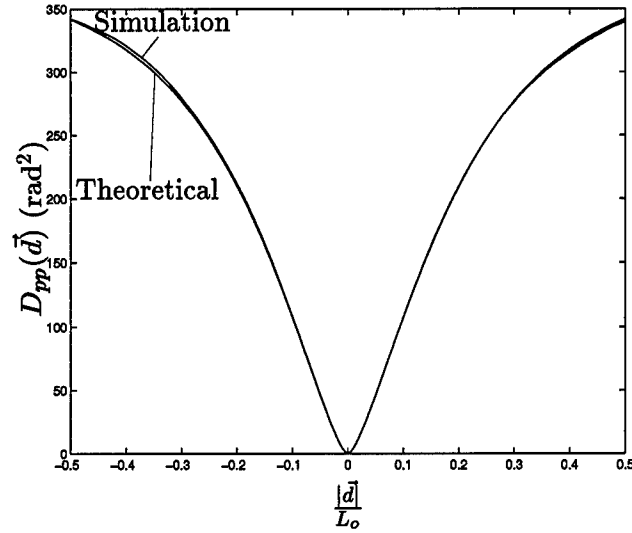


Figure 4.10 Theoretical and simulated phase structure function, $D_{pp}(\vec{d})$, plotted versus $|\vec{d}|/L_o$ for a von Karman turbulence power spectrum with $D_p/L_o = 1.5$, $D_p/r_o = 150$, $L/L_o = 1000$, and $\lambda/L_o = 5 \times 10^{-8}$. The screen dimension is $D = 100r_o$ and the number of FS coefficients is $N = 400$. The phase screens used in this calculation were correlated with the amplitude screens by the cross correlation.

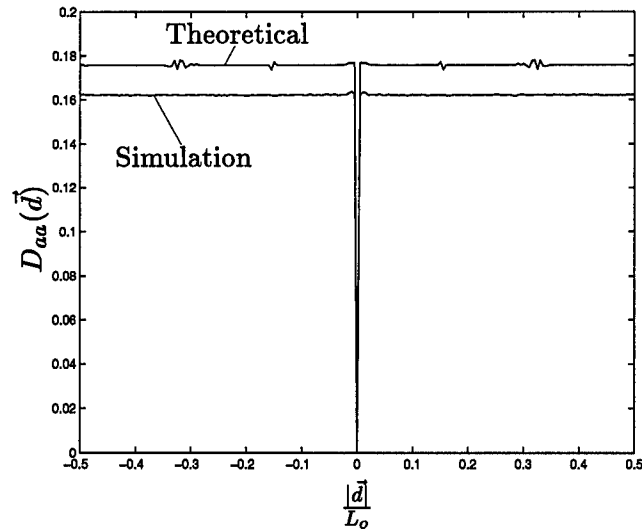


Figure 4.11 Theoretical and simulated amplitude structure function, $D_{aa}(\vec{d})$, plotted versus $|\vec{d}|/L_o$ for a von Karman turbulence power spectrum with $D_p/L_o = 1.5$, $D_p/r_o = 150$, $L/L_o = 1000$, and $\lambda/L_o = 5 \times 10^{-8}$. The screen dimension is $D = 100r_o$ and the number of FS coefficients is $N = 400$. The amplitude screens used in this calculation were correlated with the phase screens by the cross correlation.

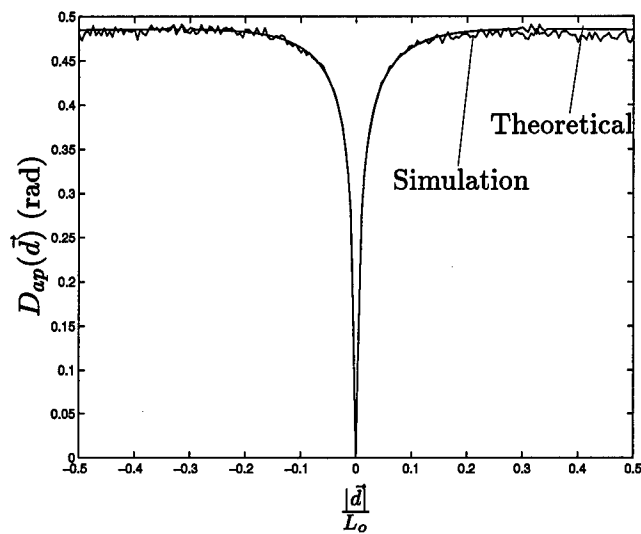


Figure 4.12 Theoretical and simulated cross structure function, $D_{ap}(\vec{d})$, plotted versus $|\vec{d}|/L_o$ for a von Karman turbulence power spectrum with $D_p/L_o = 1.5$, $D_p/r_o = 150$, $L/L_o = 1000$, and $\lambda/L_o = 5 \times 10^{-8}$. The screen dimension is $D = 100r_o$ and the number of FS coefficients is $N = 400$.

Figure 4.13 shows a random phase screen of dimension $D = 10r_o$ and Fig. 4.14 shows the correlated random amplitude screen. Notice how much larger the phase screen magnitude is than the amplitude screen. Figs. 2.5 and 2.6 from Chapter 2 illustrated the mean square value of the amplitude perturbations will get larger and the phase will get smaller as $\frac{L_o^2}{\lambda L}$ decreases for constant L_o/r_o . Therefore, if L/L_o or λ/L_o were larger the magnitude of the amplitude perturbations would be higher and the magnitude of the phase perturbations would be lower. It is also evident that the amplitude perturbations have a higher spatial frequency content than the phase perturbations which can be predicted from the power spectral density plot in Fig. 3.1.

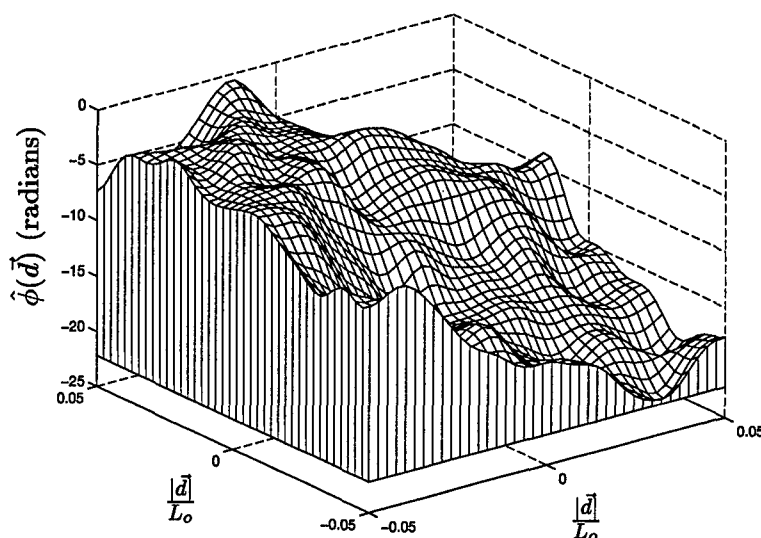


Figure 4.13 Random phase screen, $\hat{\phi}(\vec{d})$, plotted versus $|\vec{d}|/L_o$ for a von Karman turbulence power spectrum with $D_p/L_o = 4$, $D_p/r_o = 400$, $L/L_o = 1000$, and $\lambda/L_o = 5 \times 10^{-8}$. The screen dimension is $D = 10r_o$ and the number of FS coefficients is $N = 300$.

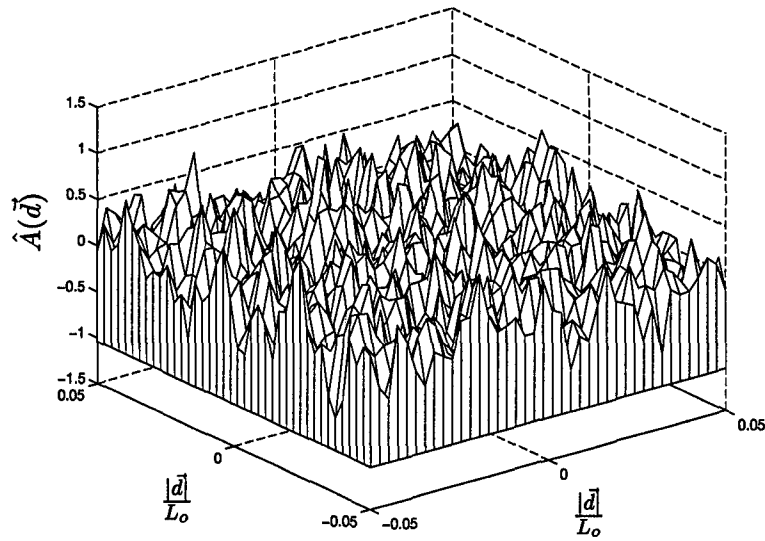


Figure 4.14 Random amplitude screen, $\hat{A}(\vec{d})$, plotted versus $|\vec{d}|/L_o$ for a von Karman turbulence power spectrum with $D_p/L_o = 1/4$, $D_p/r_o = 25$, $L/L_o = 1000$, and $\lambda/L_o = 5 \times 10^{-8}$. The screen dimension is $D = 10r_o$ and the number of FS coefficients is $N = 300$.

V. Amplitude Effects on Full Aperture Tilt Sensing

The random tilt over the aperture of an imaging system has the effect of moving an image around in the image plane of an optical system. Long exposure images will effectively average this movement over a long period of time blurring the image and reducing the resolution similar to a convolution operation. A short exposure image essentially freezes the random tilt allowing for much higher resolution. The tip-tilt mirror corrects the overall mean tilt over the aperture of the wavefront, significantly reducing the movement of the image in the image plane. It is simply a flat mirror that can be adjusted in two orthogonal directions. Adaptive optics systems began with a tilt correction system since the random tilt contains 87% of the power of the wavefront phase fluctuations. In modern adaptive optics systems the tip-tilt mirror stage separately removes the random tilt in a wavefront reducing the dynamic range requirements in the flexible or faceted deformable mirror. Refer back to Fig. 1.1 for a simplified adaptive optics system schematic. Dynamic range refers to the deflection magnitude of each actuator or facet of the mirror required to correct the higher order phase errors [12].

5.1 Full aperture tilt estimation using image centroid

There are a number of algorithms and systems used to measure the overall tilt of the wavefront in the aperture. One such measurement tracks the movement of the image centroid in the focal plane of a full aperture lens. Figure 5.1 illustrates the fundamental structure of the centroid tracker.

When the centroid of the image is located in the center of the focal plane the overall tilt of the phase perturbations in the aperture is zero. Using the Fourier transforming property of a lens the image intensity, $I(u, v)$, can be determined from the optical field, $E(x, y)$, by the following:

$$I\left(\frac{u}{\lambda f}, \frac{v}{\lambda f}\right) = \mathcal{F}\{E(x, y)\} \mathcal{F}\{E(x, y)\}^*, \quad (5.1)$$

where \mathcal{F} is the Fourier transform operator, λ is the average wavelength of the light, f is the focal length of the imaging lens, (x, y) are the coordinates in the object plane, and (u, v) are the coordinates in the focal plane [7].

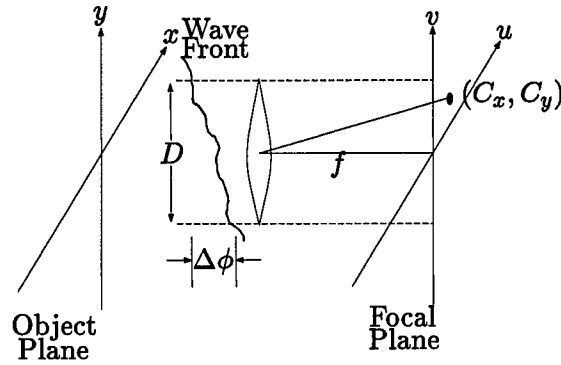


Figure 5.1 Simplified configuration of a full aperture tilt centroid tracker. (C_x, C_y) is the location of the image centroid and f is the focal length of the lens.

The centroid of the image can be determined by performing a discrete first moment calculation to determine the x and y locations of the centroid:

$$I_x = \frac{\sum_{i=1}^k M_i x_i}{\sum_{i=1}^k M_i} \quad (5.2)$$

and

$$I_y = \frac{\sum_{i=1}^k M_i y_i}{\sum_{i=1}^k M_i}, \quad (5.3)$$

where M_i is the relative irradiance on each element of the detector in the focal plane and (x_i, y_i) are the locations of each element. (I_x, I_y) represents the discrete location of the image centroid on the detector.

Simulations will be run to determine the image in the focal plane by evaluating Eq. (5.1) and using the FFT to compute the Fourier transform of the wavefront. The centroid of the image will be determined and related to the slope of the wavefront in the aperture of the system from the relationships in Eqs. (5.1), (5.2), and (5.3). Since the FFT will be implemented, a relation between the sample size in the aperture to the sample size of the focal plane detector is required. For a $m \times m$ matrix used in the computation of the image

the following relationships relate the Fourier frequency sample size to the sample size in the space domain:

$$\Delta f_x = \frac{1}{m\Delta x} \quad (5.4)$$

and

$$\Delta f_y = \frac{1}{m\Delta y} \quad (5.5)$$

where Δf_x and Δf_y are the sample size in the Fourier domain and Δx and Δy are the sample size in the space domain [5]. Now, using Eq. (5.1) one can determine the sample size in the image plane

$$\Delta u = \frac{\lambda f}{m\Delta x} \quad (5.6)$$

and

$$\Delta v = \frac{\lambda f}{m\Delta y}, \quad (5.7)$$

where Δu and Δv are sample size in the focal or detector plane. From Eqs. (5.2) and (5.3) one can determine the actual location of the centroid by computing $C_x = I_x \Delta u$ and $C_y = I_y \Delta v$.

Now, consider how the centroid location in the focal plane is related to the wavefront slope over the aperture. From Fig. 5.1 the location of the image centroid, (C_x, C_y) , is related to the orthogonal components of the wavefront slope \vec{s} by

$$s_x = k \frac{C_x}{f} = \frac{2\pi C_x}{\lambda f} \quad (5.8)$$

and

$$s_y = k \frac{C_y}{f} = \frac{2\pi C_y}{\lambda f}, \quad (5.9)$$

where (s_x, s_y) represents the x- and y-directed components of the vector \vec{s} [12]. Expressing the discrete representation of the centroid the wavefront slope can be simplified by

$$\begin{aligned} s_x &= \frac{2\pi I_x \Delta u}{\lambda f} = \frac{2\pi I_x}{\lambda f} \cdot \frac{\lambda f}{m\Delta x} \\ &= \frac{2\pi I_x}{m\Delta x} \end{aligned} \quad (5.10)$$

and

$$\begin{aligned} s_y &= \frac{2\pi I_x \Delta v}{\lambda f} = \frac{2\pi I_y}{\lambda f} \cdot \frac{\lambda f}{m \Delta y} \\ &= \frac{2\pi I_y}{m \Delta y}. \end{aligned} \quad (5.11)$$

Recall that $m \times m$ is the dimension of the matrix in the FFT calculation.

5.1.1 Tilt estimation calculation using random screens. The random phase and amplitude screen generator outlined in Chapter 4 will be used to determine the effect the amplitude perturbations have on the wavefront slope estimation, (s_x, s_y) . The random screen consists of a $M \times M$ matrix of dimension, D . Therefore, $\Delta x = D/M$ and $\Delta y = D/M$ and (s_x, s_y) becomes

$$s_x = \frac{2\pi I_x}{\frac{m}{M} D} \quad (5.12)$$

and

$$s_y = \frac{2\pi I_y}{\frac{m}{M} D}. \quad (5.13)$$

Using Eqs. (5.6) and (5.7) one can determine the size of the FFT matrix that must be used to determine the image in the focal plane given the particular sample size of the detector, Δu and the optical parameters λ , f , and D . Solving for m , Eq. (5.6) becomes

$$m = \frac{\lambda f}{\Delta x \Delta u} = \frac{\lambda f M}{D \Delta u} = \frac{\lambda f_{\#} M}{\Delta u}, \quad (5.14)$$

where $\Delta u = \Delta v$, $\Delta x = \Delta y$, and $f_{\#} = f/D$ is the f-number of the lens.

5.2 Simulations using the random screen generator with **uncorrelated** amplitude and phase screens

The screen generator will be used to investigate how the amplitude perturbations affect the tilt calculation. The mean square error in the tilt calculation will be determined for an ensemble of square screens. The estimated tilt will be subtracted from the phase screens to determine how well the algorithm performs for different situations.

Turbulence and Optical Parameters		
Parameter	Range	
	low high	Default
Propagation length over outer scale, L/L_o .	1000–50,000	10,000
Strength of turbulence, L_o/r_o .	50–500	200
Wavelength over outer scale, λ/L_o .	1.0×10^{-8} – 1.0×10^{-7}	5.0×10^{-8}
Diameter over Fried parameter, D/r_o .	2–100	10

Table 5.1 Atmospheric turbulence and optical parameters used in simulations.

The amplitude and phase screens used in these simulations are uncorrelated. Section 5.3 provides justification for using the uncorrelated screens over the correlated screens.

The following parameters D/r_o , L/L_o , L_o/r_o , and λ/L_o as shown in Table 5.1 will be studied to determine their effect on the tilt estimation. Square screens of width, D , will be used to simulate atmospheric turbulence over a square aperture. As each parameter is varied, all other parameters will remain constant. Since many of the parameters are inter-related, care must be taken in the analysis of the results. For instance, normally decreasing L/L_o will result in less turbulence effects. Since D/r_o is proportional to the integrated turbulence profile and held constant, decreasing L/L_o had the effect of simulating shorter but more concentrated turbulence strength profiles.

5.2.1 Mean square error in the tilt estimation. The estimated tilt will be calculated for each random screen, the square error in the estimation determined for each realization, and the mean calculated for the entire ensemble. The mean square error in the tilt estimation can be defined as

$$T_{mse} = \frac{\langle (t_x - s_x)^2 + (t_y - s_y)^2 \rangle}{2}, \quad (5.15)$$

where t_x and t_y are the x - and y -directed components of the actual tilt and the angle brackets represent the ensemble average operation. The T_{mse} for a random amplitude and phase screen will be compared with the error in the tilt estimation using a phase only screen. The components of the actual tilt, t_x and t_y , are calculated by taking the average slope over the phase screen. The mean square tilt of the phase screens is defined as

$$T_{ms} = \frac{\langle t_x^2 + t_y^2 \rangle}{2}. \quad (5.16)$$

The standard deviation of the mean for the Monte Carlo experiments can be determined by

$$\sigma_{\mu} = \frac{\sigma}{\sqrt{N}} \simeq \frac{s}{\sqrt{N}}, \quad (5.17)$$

where σ is the actual standard deviation of the population, s is the standard deviation of the sample, and N is the number of iterations in the simulation [1]. Using Eq. (5.17), an experiment of 1200 random screens or iterations was determined to be sufficient in the Monte Carlo calculations of the tilt. The standard deviation in the mean for T_{mse} was approximately 1/35th of the mean.

In the Monte Carlo experiments the following calculations were performed for each iteration. First, the actual tilt is calculated from the phase screen. Then, the full aperture tilt estimation algorithm is performed using Eqs. (5.12) and (5.13) on the optical field screen consisting of the phase *and amplitude* perturbations. Next, we use Eqs. (5.12) and (5.13) again, but this time we include only the phase perturbations in the screen. Finally, the mean square error in the tilt, T_{mse} , is calculated for the phase only screen and the phase and amplitude screen using Eq. (5.15). The difference between the T_{mse} 's represents the effect the amplitude perturbations have on the tilt estimation. The mean square tilt, T_{ms} , and T_{mse} are presented in the plots in radians² per number of r_o squared (or $\text{rad}^2 / \left(\frac{|d|}{r_o}\right)^2$).

In the first case, the propagation length over outer scale, L/L_o , was varied. The mean square error in the tilt estimation, T_{mse} , is plotted in Fig. 5.2 for both cases. Normally as the propagation path lengthens the turbulence effects become more severe, but since D/r_o and L_o/r_o are held constant, only the proportion of the amplitude to the phase perturbations changes. Figs. 2.5 and 2.6 from Chapter 2 show that the mean square value of the amplitude increases with L/L_o and the mean square value of the phase decreases when all other factors are held constant. Therefore as L/L_o gets larger, the larger amplitude perturbations cause the T_{mse} for the phase and amplitude screen case to increase. Whereas, the phase only T_{mse} decreases as L/L_o increases due to the slight decrease in phase perturbations. In addition, as these phase perturbations decrease with smaller L/L_o the mean square tilt, T_{ms} , decreases as expected.

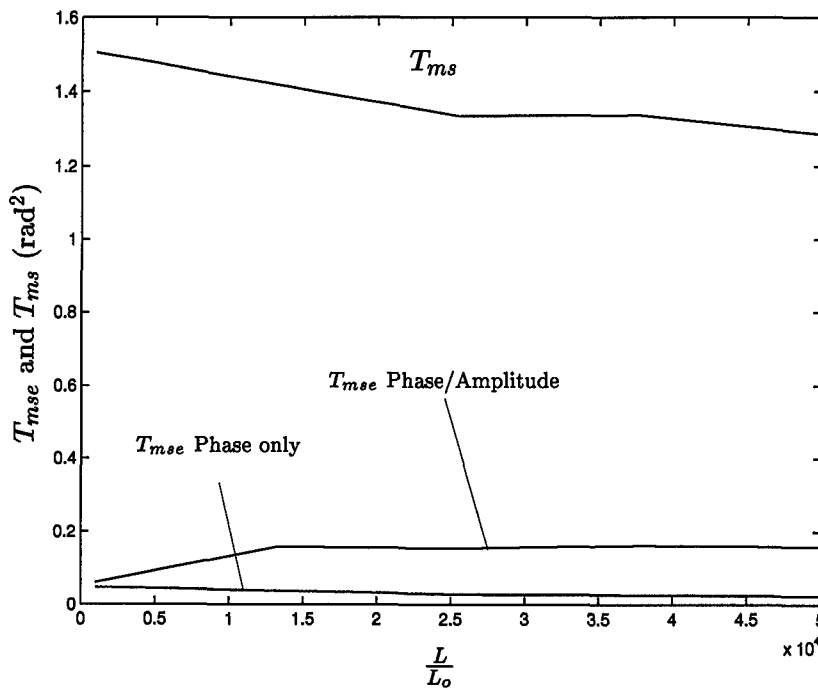


Figure 5.2 The mean square error in the tilt estimation, T_{mse} , and the mean square tilt, T_{ms} , are plotted versus L/L_o for $D/r_o = 10$, $L_o/r_o = 200$, and $\lambda/L_o = 5.0 \times 10^{-8}$. The T_{mse} is calculated twice, once using the phase and amplitude screen case and once for the phase screen only case. The T_{ms} is calculated by computing the average slope of the phase over the screen.

Next the strength of turbulence, L_o/r_o , was varied and the T_{ms} and T_{mse} were calculated again. The mean square error for both cases and the mean square tilt are shown in Fig. 5.3. As L_o/r_o increases and D/r_o is held constant the lower order phase perturbations (e.g., tilt) increase while the higher order perturbations decrease. The upward trend in the tilt, T_{ms} , is due to larger outer scales, L_o , contributing to higher tilt in the wavefront, but flatter smoother variations. The mean square value of the amplitude perturbations increase with the strength of turbulence as shown in Fig. 2.6. This increase in amplitude effects causes greater error in the tilt estimate for the phase and amplitude screen. Whereas, T_{mse} for the phase only case decreases as L_o/r_o increases, since the tilt estimator performs better for flatter phase screens.

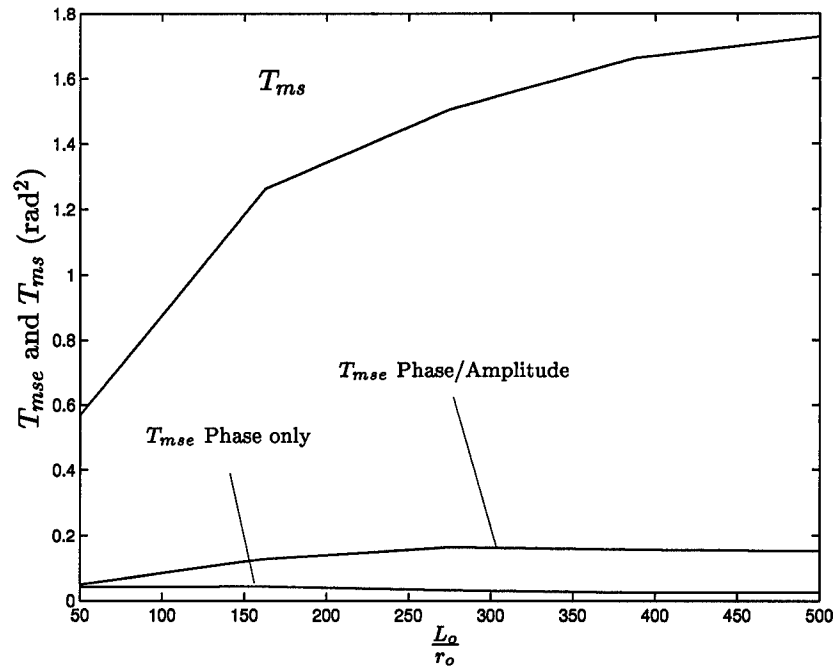


Figure 5.3 The mean square error in the tilt estimation, T_{mse} , and the mean square tilt, T_{ms} , are plotted versus L_o/r_o for $D/r_o = 10$, $L/L_o = 10000$, and $\lambda/L_o = 5.0 \times 10^{-8}$. The T_{mse} is calculated twice, once using the phase and amplitude screen case and once for the phase screen only case. The T_{ms} is calculated by computing the average slope of the phase over the screen.

Next, the tilt estimation is investigated for changes in λ/L_o in Fig. 5.4. Similar to L/L_o , Figs. 2.5 and 2.6 from Chapter 2 also show that the mean square value of the amplitude increases with λ/L_o and the mean square value of the phase decreases when the other factors are held constant. As λ/L_o gets larger, T_{mse} for the phase/amplitude case increases due to the larger amplitude perturbations. Whereas, the phase only T_{mse} decreases slightly as λ/L_o increases due to the decrease in phase perturbations. In addition, as these phase perturbations decrease the mean square tilt, T_{ms} , decreases slightly as expected.

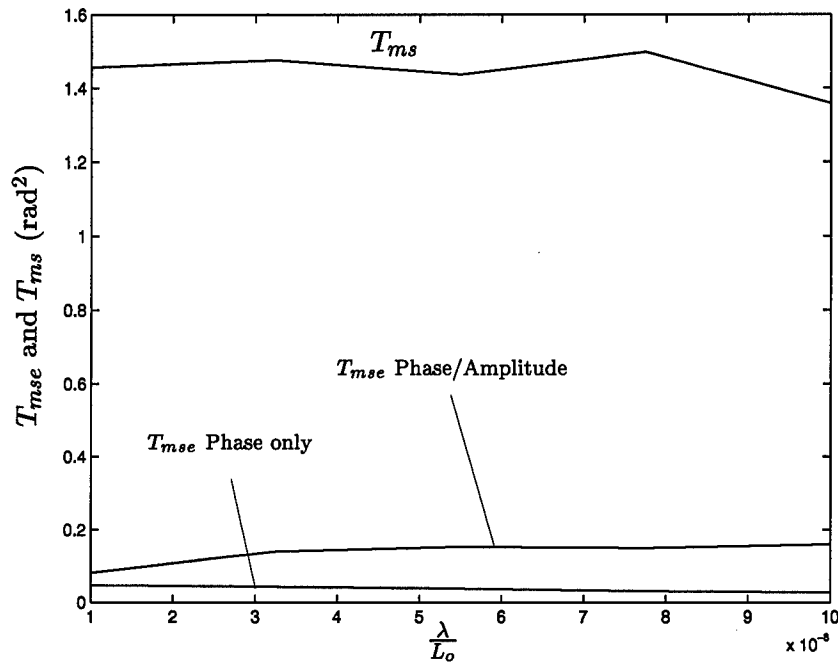


Figure 5.4 The mean square error in the tilt estimation, T_{mse} , and the mean square tilt, T_{ms} , are plotted versus λ/L_o for $D/r_o = 10$, $L/L_o = 10000$, and $L_o/r_o = 200$. The T_{mse} is calculated twice, once using the phase and amplitude screen case and once for the phase screen only case. The T_{ms} is calculated by computing the average slope of the phase over the screen.

Finally, the tilt estimation is investigated for changes in D/r_o in Fig. 5.5. Since L/L_o , L_o/r_o , and λ/L_o are held constant the strength and nature of the phase and amplitude perturbations remain relatively constant over a fixed area. Over very large apertures the phase tilt is very small, but as the aperture size decreases the mean square tilt, T_{ms} , increases. Therefore, as D/r_o gets larger, the tilt over the entire aperture decreases significantly. The error, T_{mse} , decreases for both cases as T_{ms} decreases.

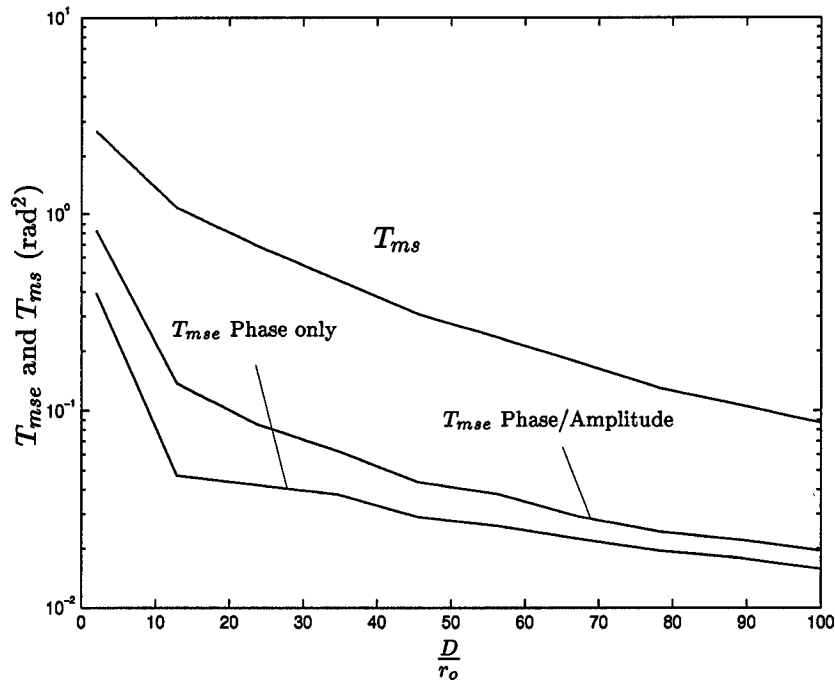


Figure 5.5 The mean square error in the tilt estimation, T_{mse} , and the mean square tilt, T_{ms} , are plotted versus D/r_o for $\lambda/L_o = 5.0 \times 10^{-8}$, $L/L_o = 10000$, and $L_o/r_o = 200$. The T_{mse} is calculated twice, once using the phase and amplitude screen case and once for the phase screen only case. The T_{ms} is calculated by computing the average slope of the phase over the screen.

5.2.2 Strehl ratio calculation. The Strehl ratio will be calculated before and after removing the tilt in the screen for the ensemble of random screens. The ensemble of screens will be generated in a Monte Carlo experiment. The point spread function is the image-plane intensity distribution resulting from imaging a point source [12]. The point spread function (psf) can be represented as

$$\begin{aligned} s(u, v) &= I(u, v) * \delta(0, 0) \\ &= I(u, v), \end{aligned} \tag{5.18}$$

where $\delta(0, 0)$ is the Dirac delta function and $*$ is the convolution operator. The psf will be calculated for each screen and averaged over the ensemble to simulate a long exposure image. Each corrected screen will be determined by subtracting the estimated tilt from the phase screen. The Strehl ratio is defined as the ratio of maximums between the actual psf and the diffraction limited psf. The Strehl ratio will be calculated for four different cases:

1. The actual tilt, t_x and t_y , will be determined by taking the average slope over the entire phase screen. The actual tilt will be subtracted from the phase screen and the Strehl ratio, SR_{UT} , will be calculated for the ensemble average psf of the corrected phase and original amplitude screens. The subscript, UT , refers to the screens "untitled" by the actual tilt.
2. The estimated tilt, s_x and s_y , will be determined from Eqs. (5.1), (5.12), and (5.13) by using the centroid of the phase screen only image. The estimated tilt will be subtracted from the phase screen and the Strehl ratio, SR_{UTP} , will be calculated for the ensemble average psf of the corrected phase and the original amplitude screens. The subscript, UTP , refers to the screens "untitled" by the estimated tilt from the phase screen image centroid.
3. The estimated tilt, s_x and s_y , will be determined from Eqs. (5.1), (5.12), and (5.13) by using the centroid of the phase and amplitude screen image. The estimated tilt will be subtracted from the phase screen and the Strehl ratio, SR_{UTAP} , will

be calculated for the ensemble average psf of the corrected phase and the original amplitude screens. The subscript, *UTAP*, refers to the screens "untitled" by the estimated tilt from the amplitude/phase screen image centroid.

4. The Strehl ratio, *SR*, will be calculated for the uncorrected phase screen using the ensemble average psf of the combined phase and amplitude screens.

Strehl ratio calculations 1 through 3 will have the effect of decreasing the movement of the image in the focal plane. Whereas, the uncorrected phase screen case of calculation 4 above will be averaged over a wider range of image motion. The corrected screen with the least amount of image motion over the ensemble will result in the highest Strehl ratio. Figure 5.6 shows a block diagram of the four different Strehl ratio calculations performed.

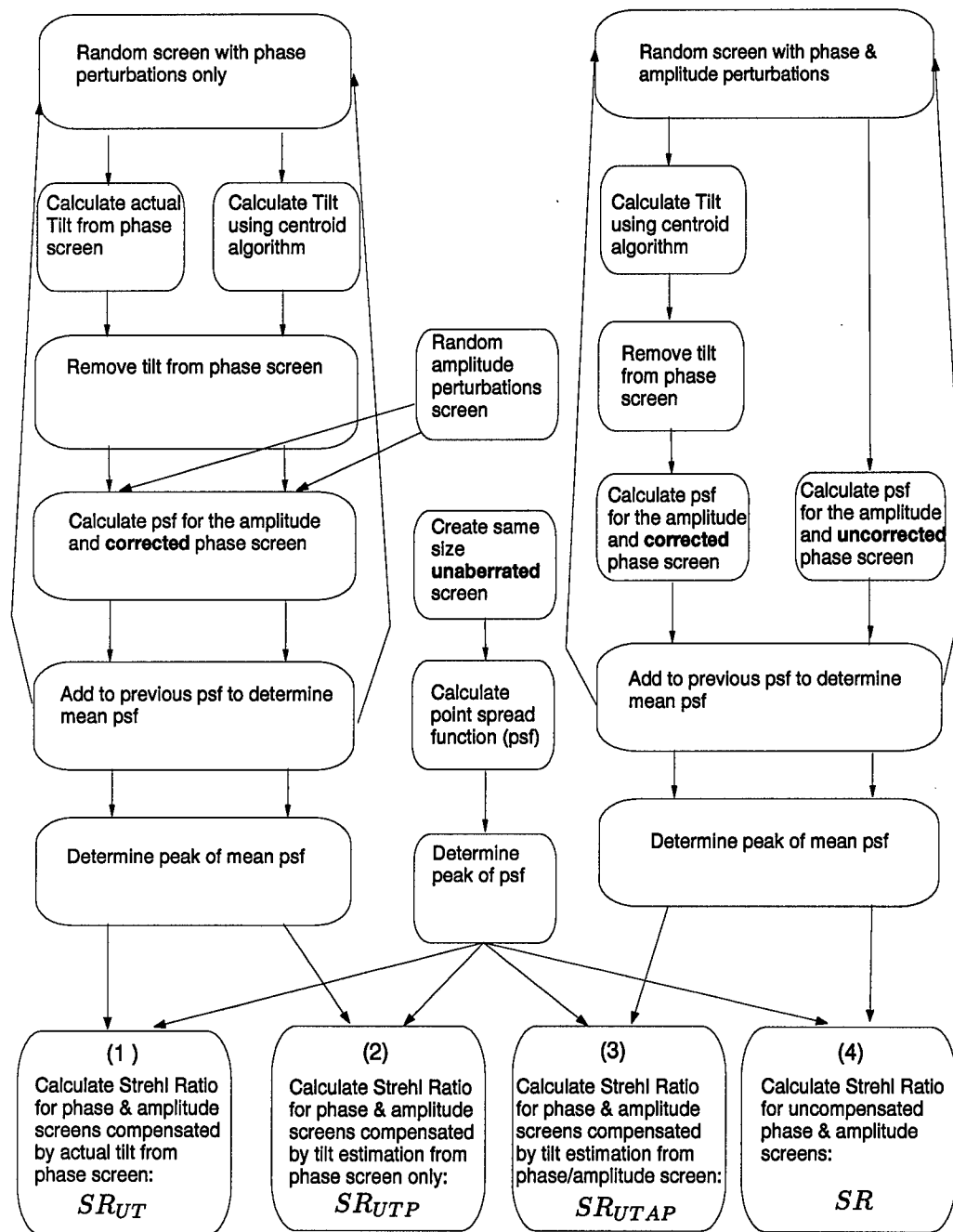


Figure 5.6 Block diagram of Strehl ratio calculation procedure. Random screens are generated by following the *Screen Generation* procedure in Sec. 4.3.2. Strehl ratios SR_{UT} , SR_{UTP} , and SR_{UTAP} are for screens compensated by the actual tilt, estimated tilt using phase screen image centroid, and estimated tilt using phase/amplitude screen image centroid, respectively. The fourth Strehl ratio, SR , is calculated for the random uncompensated phase/amplitude screen.

Figure 5.7 shows the point spread function of the diffraction limited unaberrated screen. The uncorrected random screen's psf for the short exposure image is shown in Fig. 5.8. The simulations were run by performing a Monte Carlo experiment to generate random screens. By taking the ensemble mean of the psf's of each screen the long exposure point spread functions were determined. The uncorrected long exposure psf is shown in Fig. 5.9 (case 4 in Fig. 5.6). The long exposure psf for the screens compensated by the phase only image centroid estimated tilt is shown in Fig. 5.10 (case 2 in Fig. 5.6). The long exposure psf for the screens compensated by the actual tilt is shown in Fig. 5.11 (case 1 in Fig. 5.6). The long exposure psf for the screens compensated by the phase/amplitude image centroid estimated tilt is shown in Fig. 5.12 (case 3 in Fig. 5.6). Notice how the uncorrected long exposure psf is shorter and wider than that of the corrected screens. Also, notice how the screen compensated by using the phase/amplitude centroid estimate is higher and narrower than the screens compensated by the actual average tilt and the phase centroid estimate.

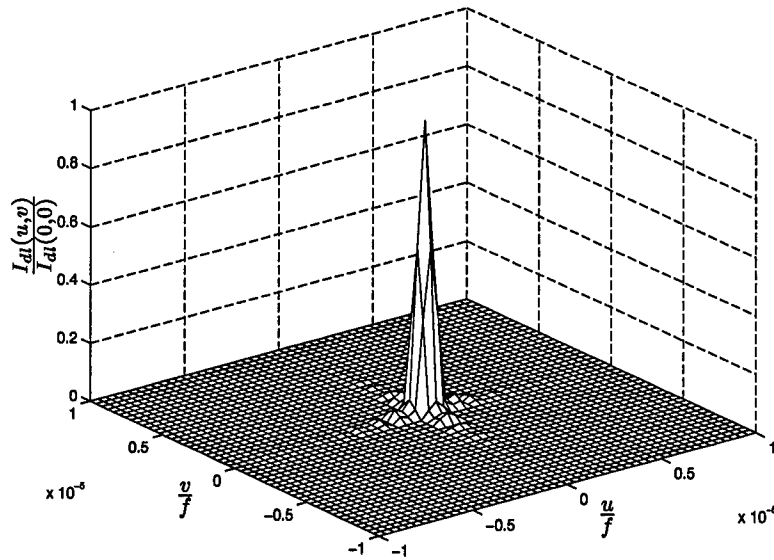


Figure 5.7 Point spread function of the diffraction limited unaberrated screen.

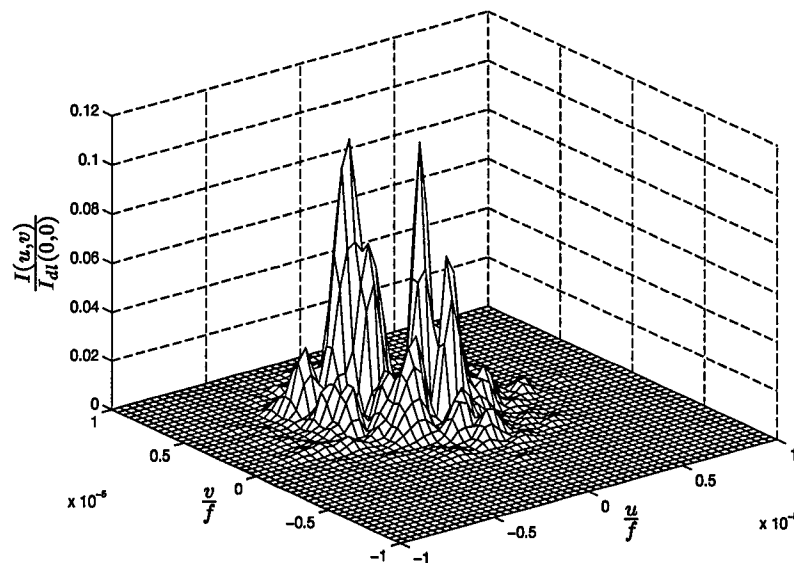


Figure 5.8 Point spread function (psf) of the uncorrected random screen for the short exposure image for the following parameters $L/L_o = 50,000$, $D/r_o = 10$, $L_o/r_o = 200$, and $\lambda/L_o = 5.0 \times 10^{-8}$.

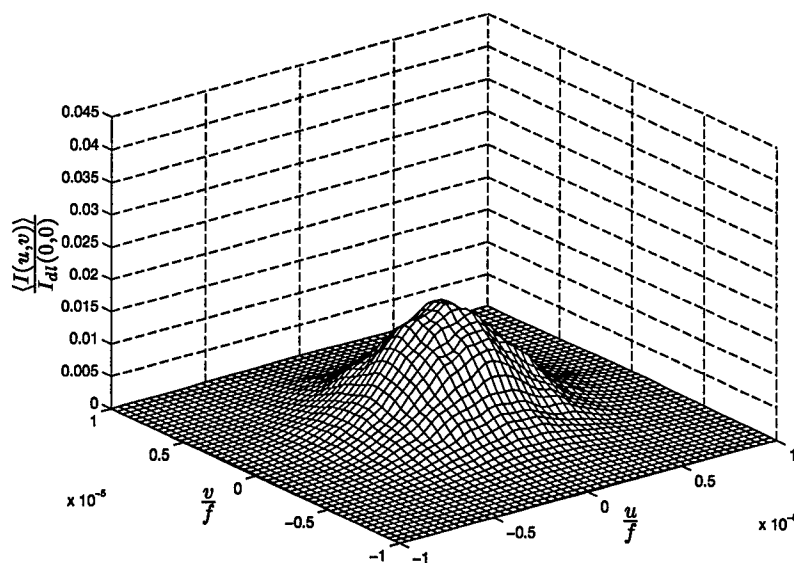


Figure 5.9 Point spread function (psf) of the uncorrected random screen for the long exposure image for the following parameters $L/L_o = 50,000$, $D/r_o = 10$, $L_o/r_o = 200$, and $\lambda/L_o = 5.0 \times 10^{-8}$.

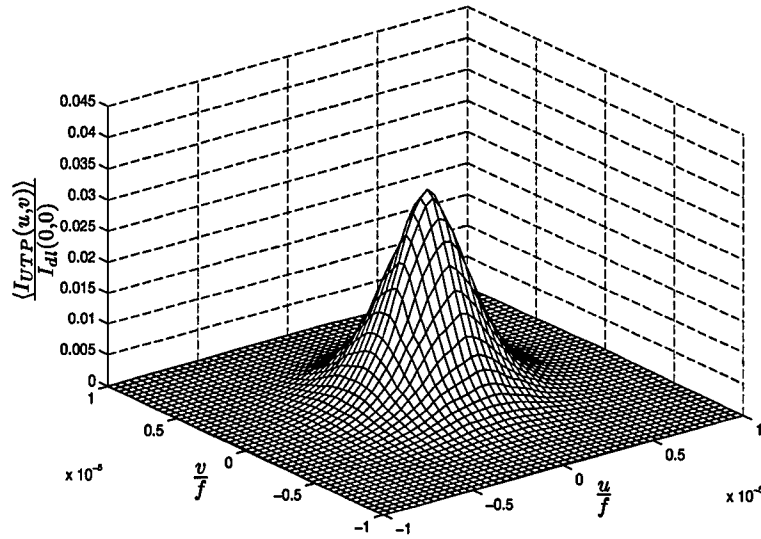


Figure 5.10 Point spread function (psf) of the corrected random screen using the image centroid of the phase screen only to determine the tilt for the long exposure image for the following parameters $L/L_o = 50,000$, $D/r_o = 10$, $L_o/r_o = 200$, and $\lambda/L_o = 5.0 \times 10^{-8}$.

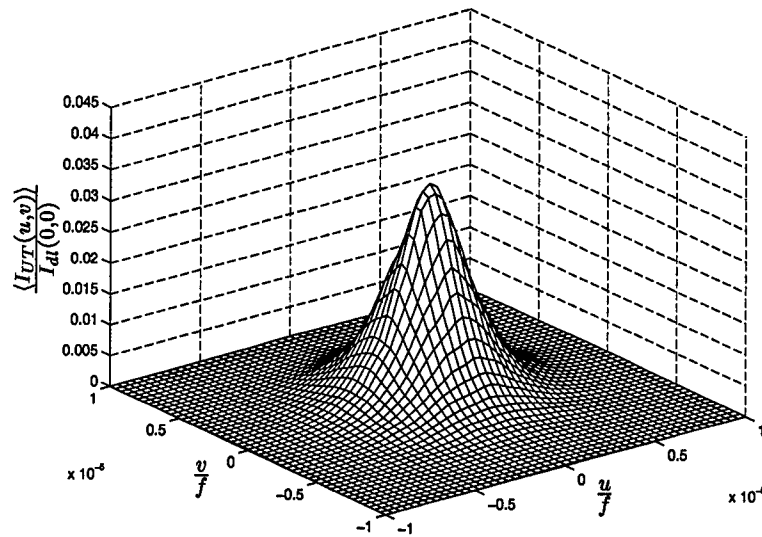


Figure 5.11 Point spread function (psf) of the corrected random screen using the actual average tilt for the long exposure image for the following parameters $L/L_o = 50,000$, $D/r_o = 10$, $L_o/r_o = 200$, and $\lambda/L_o = 5.0 \times 10^{-8}$.

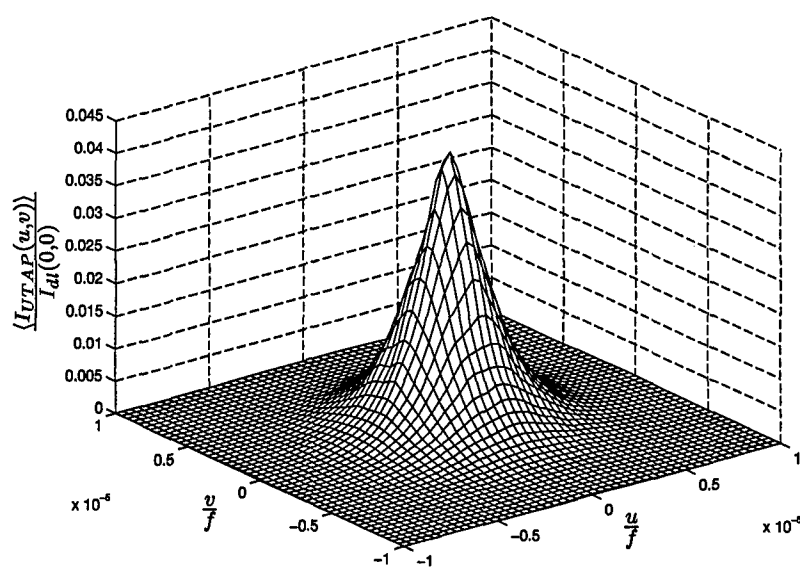


Figure 5.12 Point spread function (psf) of the corrected random screen using the image centroid of the phase/amplitude screen for the long exposure image for the following parameters $L/L_o = 50,000$, $D/r_o = 10$, $L_o/r_o = 200$, and $\lambda/L_o = 5.0 \times 10^{-8}$.

In Fig. 5.13 the strength of turbulence is held constant regardless of the length of propagation allowing for an isolation of the effects of changing L/L_o . For longer propagation paths the relative phase perturbations decrease while the amplitude perturbations increase. Since phase perturbations have the greatest effect on the psf, the Strehl ratios rise as the phase perturbations decrease.

From Fig. 5.13 one can see using the amplitude/phase screen image centroid to estimate tilt correction allows for a higher Strehl ratio, SR_{UTAP} , over the Strehl ratios, SR_{UT} and SR_{UTP} , that use the phase to estimate the correction. Equations (5.12) and (5.13) map the centroid location to the tilt correction required to move the centroid to the center of the image. Since the phase as well as the amplitude perturbations affect the position of the centroid, subtracting the average phase tilt over the screen will not take into account the effect the amplitude perturbations have on the image centroid. If, however, the phase and amplitude screen image centroid is used to determine the tilt correction, the phase and amplitude image centroid will move closer to the center of the image. The less movement of the image centroid the higher the Strehl ratio will be for the ensemble.

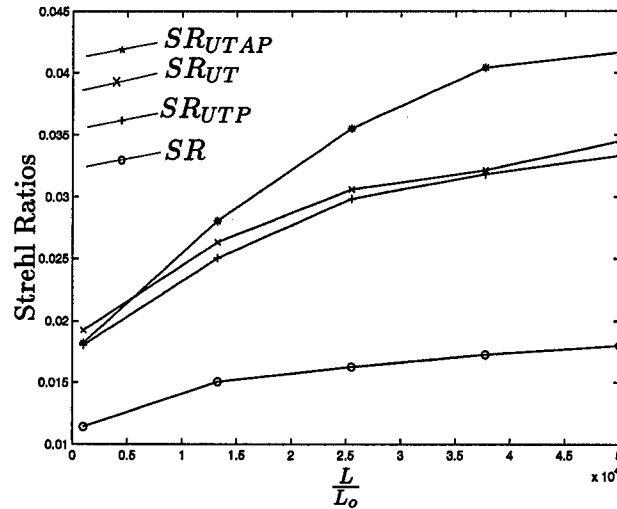


Figure 5.13 Strehl ratios of the simulated wavefront are plotted versus L/L_o for $D/r_o = 10$, $L_o/r_o = 200$, and $\lambda/L_o = 5.0 \times 10^{-8}$. Strehl ratios are plotted for the compensated screen with phase/amplitude centroid, SR_{UTAP} , compensated screen with actual phase tilt, SR_{UT} , compensated screen with phase centroid, SR_{UTP} , and uncompensated screen, SR .

In Fig. 5.14, as the strength of turbulence, L_o/r_o , increases the uncompensated Strehl ratio, SR , remains relatively constant. As L_o/r_o increases and D/r_o is held constant the lower order phase perturbations increase (i.e., more tilt) while the higher order perturbations decrease (i.e., flatter screens). The mean square tilt over the aperture increases significantly as seen in Fig. 5.3, but the decrease in higher order phase perturbations counteracts the effects of the larger tilt. Therefore, as the screens flatten due to increases in L_o/r_o , the Strehl ratios of the compensated screens will be higher. As before, the screens compensated by the phase/amplitude centroid calculated tilt had the highest Strehl ratio.

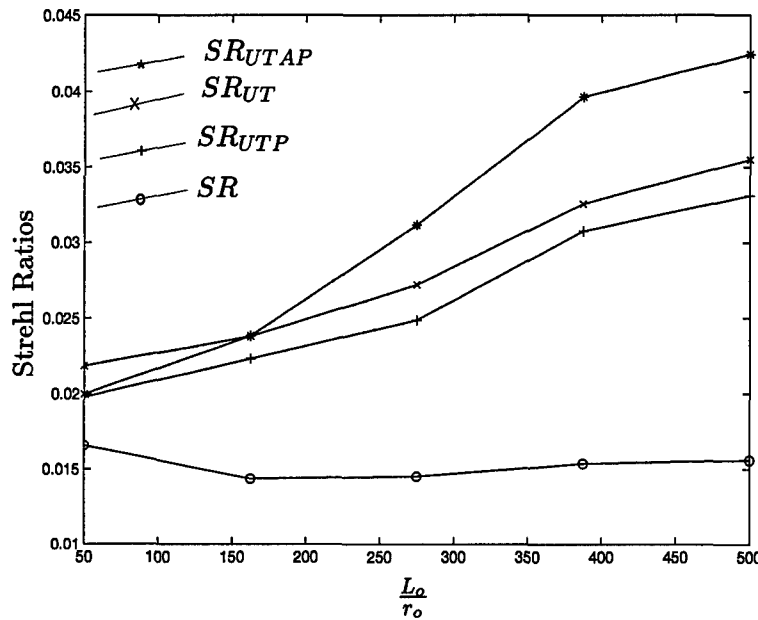


Figure 5.14 Strehl ratios of the simulated wavefront are plotted versus L_o/r_o for $D/r_o = 10$, $L/L_o = 10000$, and $\lambda/L_o = 5.0 \times 10^{-8}$. Strehl ratios are plotted for the compensated screen with phase/amplitude centroid, SR_{UTAP} , compensated screen with actual phase tilt, SR_{UT} , compensated screen with phase centroid, SR_{UTP} , and uncompensated screen, SR .

From Fig. 5.15 notice how increasing λ/L_o has nearly the same effect as increasing L/L_o . This similar relationship is due to the mean square value of the amplitude and phase perturbations' dependence upon $\frac{L_o^2}{\lambda L}$ as seen in Figs. 2.5 and 2.6.

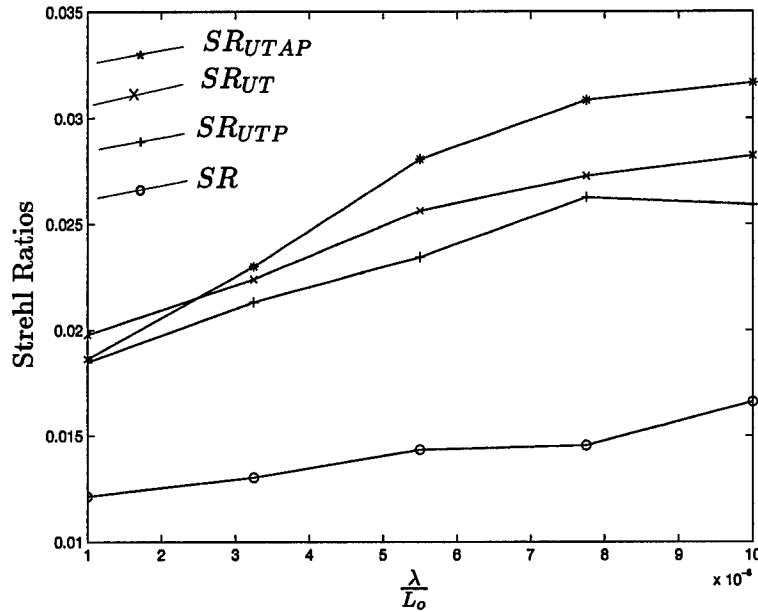


Figure 5.15 Strehl ratios of the simulated wavefront are plotted versus λ/L_o for $D/r_o = 10$, $L/L_o = 10000$, and $L_o/r_o = 200$. Strehl ratios are plotted for the compensated screen with phase/amplitude centroid, SR_{UTAP} , compensated screen with actual phase tilt, SR_{UT} , compensated screen with phase centroid, SR_{UTP} , and uncompensated screen, SR .

Figure 5.16 shows how increasing the ratio D/r_o significantly decreases the Strehl ratio. Fried parameter, r_o , can be interpreted as the limiting aperture size beyond which the turbulence does not affect the resolution. Therefore, as D/r_o gets larger the more the turbulence limits the resolution. The improvement in the Strehl ratio due to tilt removal becomes negligible as D/r_o approaches 100. Removing the tilt from the screen becomes negligible since as the aperture diameter increases the average tilt over the aperture decreases significantly as shown in Fig. 5.5.

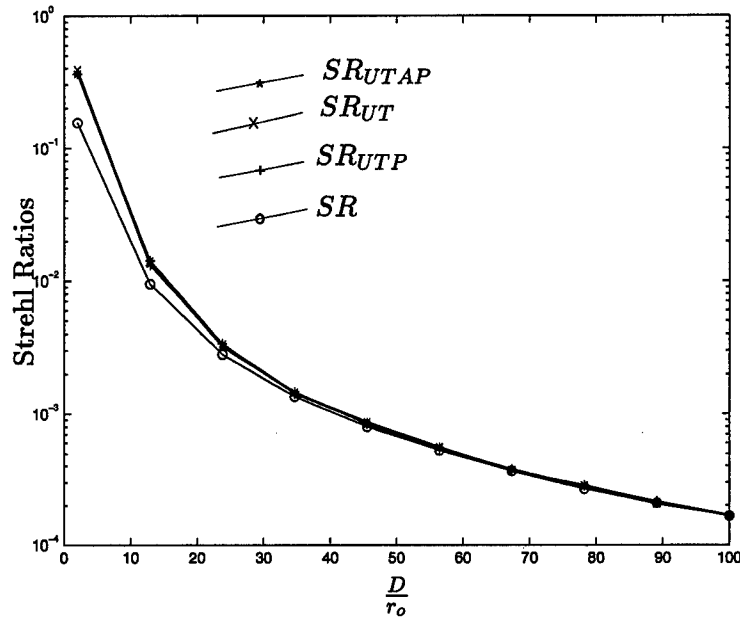


Figure 5.16 Strehl ratios of the simulated wavefront are plotted versus D/r_o for $\lambda/L_o = 5.0 \times 10^{-8}$, $L/L_o = 10000$, and $L_o/r_o = 200$. Strehl ratios are plotted for the compensated screen with phase/amplitude centroid, SR_{UTAP} , compensated screen with actual phase tilt, SR_{UT} , compensated screen with phase centroid, SR_{UTP} , and uncompensated screen, SR .

5.3 Comparisons of simulations using *correlated versus uncorrelated* phase and amplitude screens

In this section the same calculations are implemented as in the last section but this time the uncorrelated phase and amplitude screens are compared to calculations using the correlated screens. The amplitude and phase screens for the uncorrelated and correlated case will both be calculated using $D_p = 1.5$. These calculations will be performed to determine if implementing the cross correlation affects the results in any way. The parameters, L/L_o and L_o/r_o , were chosen to be studied since varying these parameters had different effects on the T_{mse} and the Strehl ratios.

5.3.1 Mean Square Error in the Tilt Estimation with *correlated versus uncorrelated* screens. The mean square error in the tilt estimation was calculated for both the correlated and uncorrelated phase and amplitude screens to determine whether the cross correlation has any effect on the results. Figures 5.17 and 5.18 show how T_{ms} and T_{mse} vary with L/L_o for the correlated and uncorrelated screens, respectively. The uncorrelated case seemed to have a slightly higher T_{ms} and T_{mse} for the amplitude/phase screen. Figures 5.19 and 5.20 show how T_{ms} and T_{mse} vary with L_o/r_o for the correlated and uncorrelated screens, respectively. This time, the correlated screens case seemed to have a slightly higher T_{ms} , but slightly lower T_{mse} for the amplitude/phase screen. As one can see the mean square error in the tilt estimation is not significantly affected by the cross correlation of the amplitude and phase.

5.3.2 Strehl Ratio Calculation with *correlated versus uncorrelated* screens.

Strehl ratios were calculated for both the correlated and uncorrelated phase and amplitude screens to determine whether the cross correlation has any effect on the results. Figures 5.21 and 5.22 show how the Strehl ratios vary with L/L_o for the correlated and uncorrelated screens, respectively. Figures 5.23 and 5.24 show how the Strehl ratios vary with L_o/r_o for correlated and uncorrelated screens, respectively. The Strehl ratios for the correlated and uncorrelated screens are just slightly different, but SR_{UT} and SR_{UTP} are consistently slightly higher for the correlated screens than the uncorrelated screens.

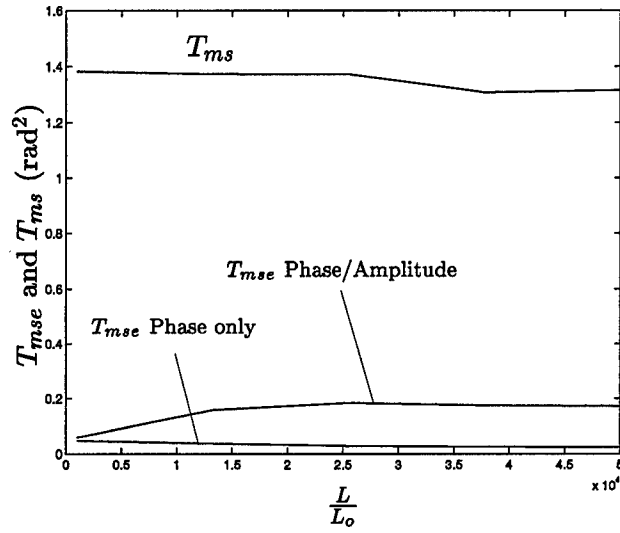


Figure 5.17 The amplitude and phase screen are **correlated** by the cross correlation. The mean square error in the tilt estimation, T_{mse} , and the mean square tilt, T_{ms} , are plotted versus L/L_o for $D/r_o = 10$, $L_o/r_o = 200$, and $\lambda/L_o = 5.0 \times 10^{-8}$. The T_{mse} is calculated twice, once using the phase and amplitude screen case and once for the phase screen only case. The T_{ms} is calculated by computing the average slope of the phase over the screen. $D_p/L_o = D_p^A/L_o = D_p^\phi/L_o = D_p^C/L_o = 1.5$.

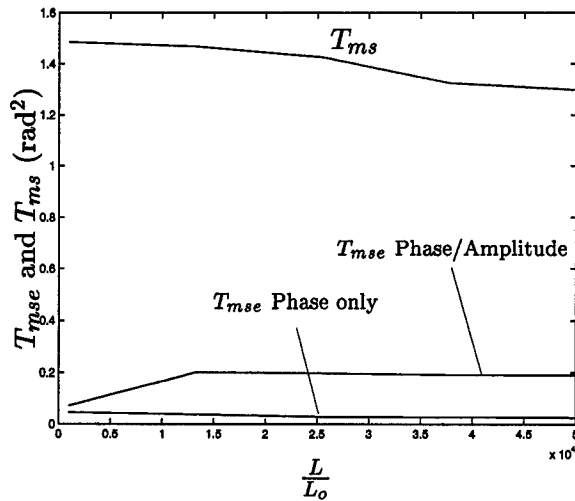


Figure 5.18 The amplitude and phase screen are **uncorrelated**. The mean square error in the tilt estimation, T_{mse} , and the mean square tilt, T_{ms} , are plotted versus L/L_o for $D/r_o = 10$, $L_o/r_o = 200$, and $\lambda/L_o = 5.0 \times 10^{-8}$. The T_{mse} is calculated twice, once using the phase and amplitude screen case and once for the phase screen only case. The T_{ms} is calculated by computing the average slope of the phase over the screen. $D_p^A/L_o = 1.5$ and $D_p^\phi/L_o = 1.5$.

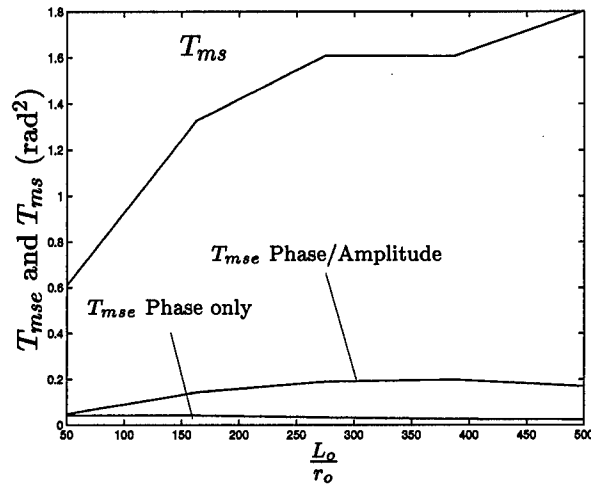


Figure 5.19 The amplitude and phase screen are **correlated** by the cross correlation. The mean square error in the tilt estimation, T_{mse} , and the mean square tilt, T_{ms} , are plotted versus L_o/r_o for $D/r_o = 10$, $L/L_o = 10000$, and $\lambda/L_o = 5.0 \times 10^{-8}$. The T_{mse} is calculated twice, once using the phase and amplitude screen case and once for the phase screen only case. The T_{ms} is calculated by computing the average slope of the phase over the screen. $D_p/L_o = D_p^A/L_o = D_p^\phi/L_o = D_p^C/L_o = 1.5$.

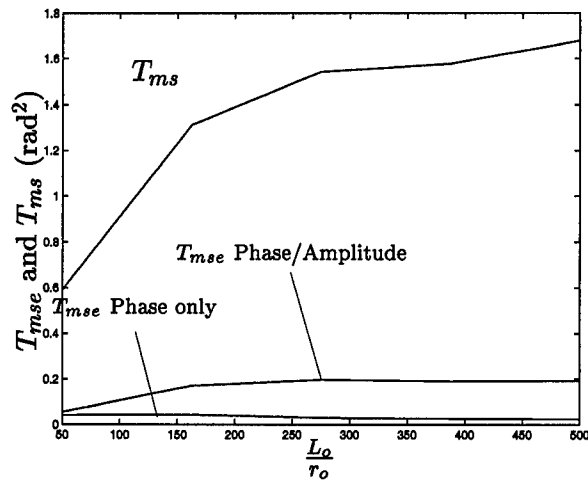


Figure 5.20 The amplitude and phase screen are **uncorrelated**. The mean square error in the tilt estimation, T_{mse} , and the mean square tilt, T_{ms} , are plotted versus L_o/r_o for $D/r_o = 10$, $L/L_o = 10000$, and $\lambda/L_o = 5.0 \times 10^{-8}$. The T_{mse} is calculated twice, once using the phase and amplitude screen case and once for the phase screen only case. The T_{ms} is calculated by computing the average slope of the phase over the screen. $D_p^A/L_o = 1.5$ and $D_p^\phi/L_o = 1.5$.

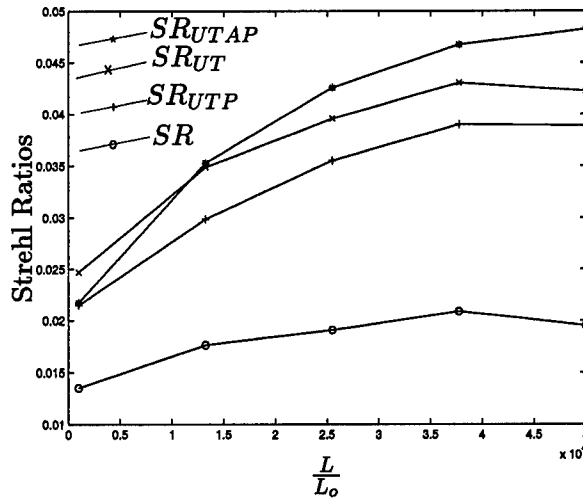


Figure 5.21 The amplitude and phase screen are **correlated** by the cross correlation. Strehl ratios of the simulated wavefront are plotted versus L/L_o for $D/r_o = 10$, $L_o/r_o = 200$, and $\lambda/L_o = 5.0 \times 10^{-8}$. Strehl ratios are plotted for the compensated screen with phase/amplitude centroid, SR_{UTAP} , compensated screen with actual phase tilt, SR_{UT} , compensated screen with phase centroid, SR_{UTP} , and uncompensated screen, SR . $D_p/L_o = D_p^A/L_o = D_p^\phi/L_o = D_p^C/L_o = 1.5$.

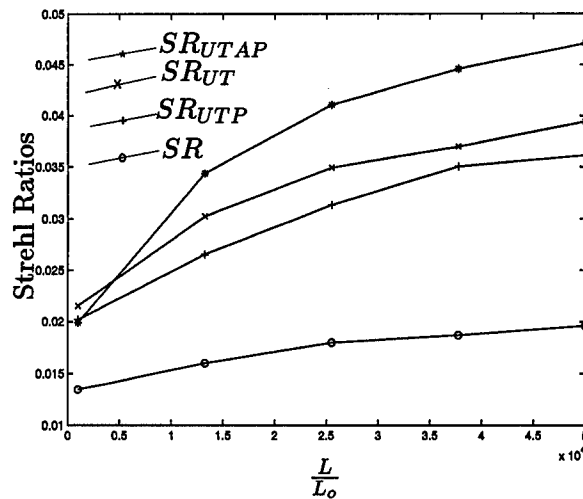


Figure 5.22 The amplitude and phase screen are **uncorrelated**. Strehl ratios of the simulated wavefront are plotted versus L/L_o for $D/r_o = 10$, $L_o/r_o = 200$, and $\lambda/L_o = 5.0 \times 10^{-8}$. Strehl ratios are plotted for the compensated screen with phase/amplitude centroid, SR_{UTAP} , compensated screen with actual phase tilt, SR_{UT} , compensated screen with phase centroid, SR_{UTP} , and uncompensated screen, SR . $D_p^A/L_o = 1.5$ and $D_p^\phi/L_o = 1.5$.

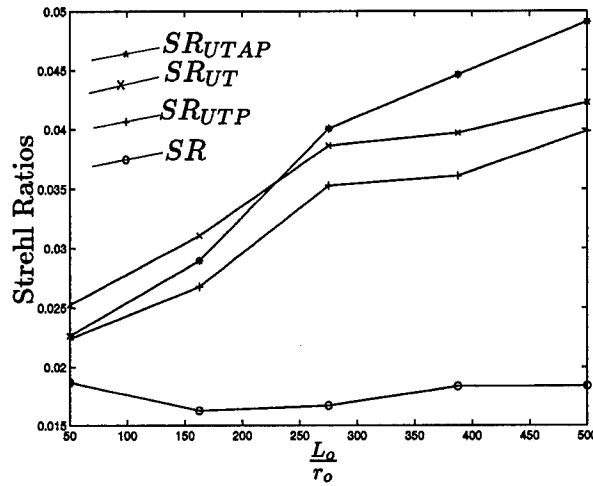


Figure 5.23 The amplitude and phase screen are **correlated** by the cross correlation. Strehl ratios of the simulated wavefront are plotted versus L_o/r_o for $D/r_o = 10$, $L/L_o = 10000$, and $\lambda/L_o = 5.0 \times 10^{-8}$. Strehl ratios are plotted for the compensated screen with phase/amplitude centroid, SR_{UTAP} , compensated screen with actual phase tilt, SR_{UT} , compensated screen with phase centroid, SR_{UTP} , and uncompensated screen, SR . $D_p/L_o = D_p^A/L_o = D_p^\phi/L_o = D_p^C/L_o = 1.5$.

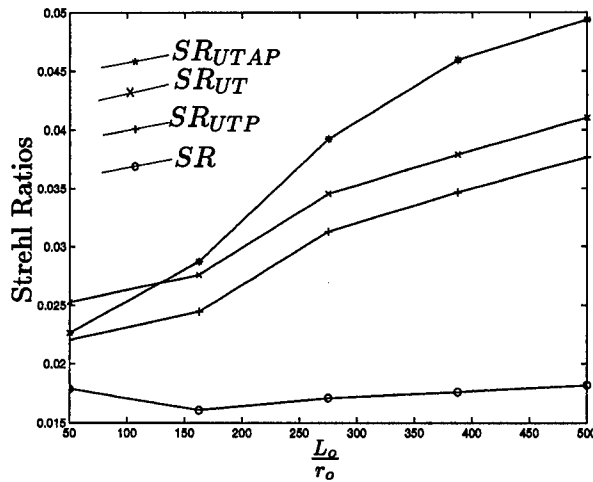


Figure 5.24 The amplitude and phase screen are **uncorrelated**. Strehl ratios of the simulated wavefront are plotted versus L_o/r_o for $D/r_o = 10$, $L/L_o = 10000$, and $\lambda/L_o = 5.0 \times 10^{-8}$. Strehl ratios are plotted for the compensated screen with phase/amplitude centroid, SR_{UTAP} , compensated screen with actual phase tilt, SR_{UT} , compensated screen with phase centroid, SR_{UTP} , and uncompensated screen, SR . $D_p^A/L_o = 1.5$ and $D_p^\phi/L_o = 1.5$.

5.3.3 Conclusions about using correlated versus uncorrelated screens. In this study uncorrelated screens were used since the amplitude perturbations were not sufficiently represented in the FS expansion. There are slight differences between using correlated versus uncorrelated screens, but the reduction in the amplitude perturbations due to the under representation proved to be of greater concern. Correlated screens could have been used in this study if more FS coefficients were used in the amplitude screen generation, but the matrix dimensions required (1080×1080) made the calculation too computationally intensive.

VI. Conclusions and Recommendations

6.1 Conclusions

A new atmospheric turbulence screen generator was developed for use in performance simulations of adaptive optics algorithms valid over a wide range of atmospheric turbulence parameters, incorporating both phase and amplitude effects. Most screen generators only calculate the phase perturbations over the aperture [2, 4, 11, 12, 15]. The screen generator developed here accounts for diffraction effects caused by weak turbulence by incorporating the phase, amplitude, and cross statistics of the perturbed optical field. The wavefront's phase and amplitude perturbations were taken from the correlation functions developed by Lee and Harp. The cross statistics of Lee and Harp's weak turbulence model were developed here for the first time and were incorporated into the screen generator. Since the amplitude perturbations cannot be corrected with adaptive optics, the theoretical limit of an adaptive optics system is bounded by the effects of the amplitude perturbations. Using both the amplitude and phase perturbations, one can more accurately simulate the performance of an adaptive optics system. Since a weak index of refraction fluctuation model was used in the development, the screen generator will not predict effects of strong turbulence, such as the saturation of the log-amplitude fluctuations.

For independent uncorrelated phase and amplitude screens the mean square value and structure functions of the Monte Carlo simulation were within 1% of the theoretical values. Due to differences in the amplitude and phase power spectral densities and computational limits on the matrix size in the calculations, the simulations for the correlated screens were within 7% of the theoretical values for the amplitude, 1% for the phase, and 1% for the cross statistics.

Incorporating the cross correlation into the simulations had a negligible effect on the results obtained and therefore the uncorrelated phase and amplitude screens were used to more accurately represent the phase and amplitude perturbations. Monte Carlo experiments performed using the screen generator showed the amplitude perturbations can significantly reduce the accuracy of full-aperture tilt estimation using image centroid motion.

In contrast, using the same amplitude/phase screen image centroid to estimate tilt correction allows for a higher Strehl ratio than using only the phase to estimate the correction. The tilt estimation algorithm maps the image centroid location to the tilt correction required to move the centroid to the center of the image. Since the phase as well as the amplitude perturbations affect the position of the centroid, subtracting the average phase tilt over the screen will not take into account the effect the amplitude perturbations have on the image centroid. If, however, the phase and amplitude screen image centroid is used to determine the tilt correction, the phase and amplitude image centroid will move closer to the center of the image. The less movement of the image centroid the higher the Strehl ratio will be for the long exposure image. Therefore, using the tilt estimator on the combined phase and amplitude screen resulted in higher Strehl ratios over subtracting the average tilt over the aperture.

6.2 Recommendations for Further Study

6.2.1 Screen Generation. In this thesis the turbulence is modeled as uniform over the propagation path which is often appropriate for horizontal propagation paths. A layered approach could be implemented to accurately represent the strength of turbulence profile up through the atmosphere. Using Taylor's frozen flow hypothesis one could also incorporate the time statistics into the amplitude and phase screen generator. As in Welsh's paper on phase screen generation one could incorporate the layered representation of the phase and amplitude, incorporate the temporal statistics, and provide for off-axis calculations to include the effects of anisoplanatism [15].

6.2.2 Simulations. The atmospheric turbulence generator developed in this thesis can be used to study the effects of amplitude perturbations on all sorts of adaptive optics algorithms. The screen generator can also be used to determine the effects of different atmospheric conditions on imaging systems or laser propagation. Including the phase and amplitude perturbations in simulations will allow one to more accurately simulate the complete performance of an adaptive optics system.

Bibliography

1. Bevington, Phillip R. and D. Keith Robinson. *Data Reduction and Error Analysis for the Physical Sciences 2nd Ed.*. New York: McGraw Hill Inc., 1992.
2. Dai, G. Ming. "Wavefront Simulation for Atmospheric Turbulence," *SPIE proceedings on Image Reconstruction and Restoration*, 2302:62-72 (1994).
3. Fried, D.L. "Optical Resolution Through a Randomly Inhomogeneous Medium for Very Long and Very Short Exposures," *Journal of the Optical Society of America A*, 56:1372-1379 (October 1966).
4. Goldring, T. and L. Carlson. "Analysis and implementation of non-Kolmogorov phase screens appropriate to structured environments," *SPIE preceeding on Nonlinear Optical Beam Manipulation and High Energy Beam Propagation Through the Atmosphere*, 1060:244-264 (1989).
5. Gonzalez, Rafael C. and Richard E. Woods. *Digital Image Processing*. New York: Addison-Wesley Publishing Company Inc., 1992.
6. Goodman, Joseph W. *Statistical Optics*. New York: John Wiley and Sons, 1985.
7. Goodman, Joseph W. *Introduction to Fourier Optics*. New York: McGraw Hill, 1996.
8. Hardy, John W. "Adaptive Optics: A New Technology for the Control of Light," *Proceedings of the IEEE*, 66(6):651-697 (June 1978).
9. Kolomogoroff, A. N. "Dissipation of energy in the locally isotropic turbulence." *Turbulence, Classical Papers on Statistical Theory* edited by S. K. Friedlander and L. Topper, 159-161, New York: Wiley-Interscience, 1961.
10. Lee, Robert W. and Jeffery C. Harp. "Weak Scattering in Random Media, with Applications to Remote Probing," *Proceedings of the IEEE*, 57(4):375-406 (April 1969).
11. Roggemann, Michael C., et al. "Method for simulating atmospheric turbulence phase effects for multiple time slices and anisoplanatic conditions," *Applied Optics*, 34:4037-4051 (1995).
12. Roggemann, Michael C. and Byron M. Welsh. *Imaging Through Turbulence*. New York: CRC Press, 1996.
13. Tatarski, V.I. *Wave Propagation in a Turbulent Medium*. New York: McGraw Hill Book Company Inc., 1961.
14. Troxel, Steven E. and Byron M. Welsh. "Off-axis optical transfer function calculations in an adaptive-optics system by means of a diffraction calculation for weak index fluctuations," *Journal of the Optical Society of America A*, 11(7):2100-2111 (July 1994).
15. Welsh, Byron M., "A Fourier Series Based Atmospheric Phase Screen Generator for Simulating Nonisoplanatic Geometries and Temporal Evolution." Reviewer Copy, 1997.

Vita

Capt Jim Louthain enrolled in Air Force Reserve Officer Training Corps (AFROTC) at the University of Portland in January 1988. He received a AFROTC scholarship in Electrical Engineering in 1988. He graduated from the University of Portland with a Bachelor of Science in Electrical Engineering and was commissioned a lieutenant in the U.S. Air Force in Dec 1991. Upon entering active duty, he served as Program Manager for a software development program in support of a B-52 weapon mission planning system and as Chief precision weapons mission planning in support of the Air Force Mission Support System (AFMSS), Mission Planning Systems, Electronic Systems Center, at Hanscom AFB Massachusetts. In May 1996 he was promoted to the rank of Captain and began his Master's degree in Electrical Engineering at the Air Force Institute of Technology, Wright-Patterson Air Force Base, Ohio. His next assignment is with the Aerospace Components and Subsystems Technology Division, Photonics Processing Branch at Rome Laboratory, Rome, New York.

Permanent address: 5415 Johnson Pt Rd
Olympia, WA 98516

REPORT DOCUMENTATION PAGE			Form Approved OMB No. 0704-0188	
Public reporting burden for this collection of information is estimated to average 1 hour per response, including the time for reviewing instructions, searching existing data sources, gathering and maintaining the data needed, and completing and reviewing the collection of information. Send comments regarding this burden estimate or any other aspect of this collection of information, including suggestions for reducing this burden, to Washington Headquarters Services, Directorate for Information Operations and Reports, 1215 Jefferson Davis Highway, Suite 1204, Arlington, VA 22202-4302, and to the Office of Management and Budget, Paperwork Reduction Project (0704-0188), Washington, DC 20503.				
1. AGENCY USE ONLY (Leave blank)		2. REPORT DATE December 1997		3. REPORT TYPE AND DATES COVERED Master's Thesis
4. TITLE AND SUBTITLE ATMOSPHERIC TURBULENCE SCINTILLATION EFFECTS ON WAVEFRONT TILT ESTIMATION				5. FUNDING NUMBERS
6. AUTHOR(S) James A. Louthain Captain, USAF				
7. PERFORMING ORGANIZATION NAME(S) AND ADDRESS(ES) Air Force Institute of Technology, WPAFB OH 45433-6583				8. PERFORMING ORGANIZATION REPORT NUMBER AFIT/GE/ENG/97D-11
9. SPONSORING/MONITORING AGENCY NAME(S) AND ADDRESS(ES) Airborne Laser Technology Division, Phillips Lab PL/LIA 3550 Aberdeen Ave. SE Kirtland AFB, NM 87117-5776				10. SPONSORING/MONITORING AGENCY REPORT NUMBER
11. SUPPLEMENTARY NOTES				
12a. DISTRIBUTION AVAILABILITY STATEMENT Approved for public release; Distribution Unlimited				12b. DISTRIBUTION CODE A
13. ABSTRACT (Maximum 200 words) <p>A new atmospheric turbulence screen generator is developed for use in performance calculations of adaptive optics systems valid over a wide range of atmospheric turbulence parameters. The screen generator accounts for diffraction effects caused by weak turbulence and incorporates the phase, amplitude, and cross statistics of the perturbed optical field. The wavefront's phase and amplitude perturbations are taken from the correlation functions developed by Lee and Harp and the cross correlation of the phase and amplitude derived in this thesis. The screen generator uses a modal representation to perform a Fourier series expansion of the wavefront phase and amplitude over a square area. The phase, amplitude, and cross power spectral densities determined from the correlation functions are used in the Fourier series expansion. The mean square value and the structure functions of the phase, amplitude, and cross terms are calculated to within 1 % of the theoretical values in a Monte Carlo experiment using the screen generator.</p> <p>Monte Carlo experiments performed using the screen generator showed the amplitude perturbations can significantly reduce the accuracy of full-aperture tilt estimation using image centroid motion. However, since the amplitude perturbations affect the image centroid, the tilt estimate using the combined amplitude and phase screen allows for a higher Strehl ratio than using only the phase to estimate the correction.</p>				
14. SUBJECT TERMS Weak Turbulence, Adaptive Optics, Phase Perturbations, Amplitude Perturbations, Scintillation, Screen, Tilt Estimation				15. NUMBER OF PAGES 99
				16. PRICE CODE
17. SECURITY CLASSIFICATION OF REPORT UNCLASSIFIED	18. SECURITY CLASSIFICATION OF THIS PAGE UNCLASSIFIED	19. SECURITY CLASSIFICATION OF ABSTRACT UNCLASSIFIED	20. LIMITATION OF ABSTRACT UL	